This is to certify that the

dissertation entitled

Investigation of the Flow Structure and Loss Mechanism in a Centrifugal Compressor Volute

presented by

Hooman Rezaei

has been accepted towards fulfillment
of the requirements for

Ph.D.

_____ degree in _____ Mechanical Engineering

_____
Major Professor

4/12/01
Date _____

PLACE IN RETURN BOX to remove this checkout from your record.
TO AVOID FINES return on or before date due.
MAY BE RECALLED with earlier due date if requested.

DATE DUE	DATE DUE	DATE DUE
MAY 2 7 2002		

INVESTIGATION OF THE FLOW STRUCTURE AND LOSS MECHANISM IN

A CENTRIFUGAL COMPRESSOR VOLUTE

By

Hooman Rezaei

A DISSERTATION

Submitted to

Michigan State University

in partial fulfillment of requirements

for the degree of

DOCTOR OF PHILOSOPHY

Department of Mechanical Engineering

2001

ABSTRACT

INVESTIGATION OF THE FLOW STRUCTURE AND LOSS MECHANISM IN A CENTRIFUGAL COMPRESSOR VOLUTE

By

Hooman Rezaei

A spiral-shaped volute is used in many applications of compressors to collect the rotating flow, which discharges from a diffuser downstream of the impeller, and to deliver it into a single discharge pipe. The performance and design of volutes has not received the detailed study given to the other components of compressors. This can be attributed to the fact that the volute is a simple collecting device and all the necessary diffusion has been achieved in the vaned or vaneless diffuser upstream of the volute. The volute is usually designed through the application of one-dimensional analysis. A design objective is to achieve a uniform pressure distribution at the volute inlet. This is usually attained at the design flow rate only; at off-design conditions the volute is either too small or too large and pressure distortion develops circumferentially around the volute passage. The static pressure distortions are transmitted to the diffuser exit, the impeller discharge, and even through the inducer. Therefore, these pressure distortions reduce the stage performance and have a direct impact on diffuser and impeller stability.

In the present study, a Trane CVHF 1280 two-stage centrifugal compressor, which is used in air-conditioning applications, was modified to a single stage. Air replaced the refrigerant gas and a new motor replaced the old driving system. The compressor's inlet and outlet components were modified to accommodate the performance evaluation experiments. The data acquisition system was developed to measure static, total temperatures and pressures at diffuser, volute casings, inlet and outlet pipes. Measurements have been performed at three speeds of 2000, 3000 and 3497 RPM in order to evaluate the performance of this compressor and its volute.

In addition, Fluent 5.0 was utilized to simulate the flow in this compressor utilizing the experimental and meanline analysis data as the boundary conditions. An unstructured grid was generated in GAMBIT for the region of vaneless diffuser inlet to the volute cone outlet. The simulations were performed for adiabatic flow in this flow path to extract the flow structure and calculate the performance of the components. The numerical results are in a good agreement with the experimental ones, which validates the simulations. Furthermore, the flow properties were extracted for various cross sections of the volute and vaneless diffuser from the simulation results in order to investigate the flow structure inside these components at off design condition. These results revealed the deviation of the volute flow from the free vortex design methodology in all cases. In addition the compressor performance improved as speeds and mass flow rates increases because the losses decrease for those conditions. The losses corresponding to tongue region were inevitable and design modifications were discussed to reduce the effect of the tongue and improve the compressor performance.

To my parents for all their
sacrifices throughout their
lives to enjoy this moment

AKNOWLEDGEMENT

Throughout the program the author has enjoyed extensively the love and support of his wife, Mrs. Stephanie Bonin. She had significant input in preparing this dissertation and concluding publications, which made him more grateful of her company.

TABLE OF CONTENTS

LIST OF FIGURES

NOMENCLATURE

.

A	Area
AR	Area Ratio
a	Speed of Sound
b	Passage Width
C	Absolute Velocity, Constant
C_P	Specific Heat Constant Pressure, Static Pressure Recovery Coefficient
C_v	Specific Heat Constant Volume
C_f	Friction Factor
d	Diameter
D	Diameter
g	Gravity
h	Enthalpy, Head loss
k	$1-\left(\dfrac{r_h}{r_s}\right)^2$
L	Axial Length
$\dot{m}$	Mass Flow Rate
M	Mach number
N	Rotational Speed
N_s	Specific Speed
P	Pressure
Q	Volume Flow Rate
r	Radius
R	Gas Constant, Center of the Volute Radius
Re	Reynolds Number
s	Entropy
t	Blade Thickness
T	Temperature
U	Blade Velocity
W	Relative Velocity, Work
X	X-Axis
Y	Y-Axis
Z	Number of Blade, Z-Axis

GREEK

α	Absolute Flow Angle
β	Relative Flow Angle
γ	Ratio of Specific Heats
η	Efficiency
μ	Viscosity
ρ	Density
σ	Slip Factor
ω	Rotation Speed (Radian/sec), Vorticity
ϕ	Flow Coefficient, Angle
θ	Circumferential Angle

ψ Work Coefficient

SUBSCRIPT

0	Stagnation Condition, Ambient Condition
1	1st stage inlet
2	1st impeller discharge
3	1st diffuser inlet
4	Bend inlet
5	Bend outlet
6	Vane inlet
7	Vane outlet
8	2nd stage inlet
9	2nd impeller discharge
10	2nd diffuser inlet
11	Volute inlet
12	Volute outlet

av	Average
ax	Axial
b	Blockage
c	Compressor, Throat center
flow	Effective Flow Area
h	Hub
i	Inner
in	Inlet
m	Meridional
o	Outer
out	Outlet
r	Radial
u	Circumferential, Tangential
s	Shroud, Swirl, Static Condition
t	Tangential, Through flow, Total Condition
th	Throat, Theoretical
w	Relative

SUPERSCRIPT

-	Average

CHAPTER 1

INTRODUCTION

In this chapter, a centrifugal compressor, its components and their interactions are discussed. In order to remind the reader the governing equations and preliminary design methodology of these compressors, steps of the design of a two stage centrifugal compressor are described. At the end of the chapter, the reader's attention is drawn to the importance of the volute performance and design models in order to help exploring the details of the next chapters.

1.1 COMPRESSORS

The major fluid mechanics problem in turbomachinery is the design of compressors. A turbine, with its flow usually going from a high to a low pressure, always works and with reasonable care it works at high efficiency. A compressor, particularly the axial-flow type, may not produce a pressure rise at all. Until almost the beginning of the 20th century, compressor isentropic efficiencies were generally less than 50 percent.

There is no record of the efficiencies of Papin's centrifugal blowers (1705). There appears to have been little development between that time and 1884, when Charles Parsons patented an axial-flow compressor. Three years later, he designed and sold a three-stage centrifugal compressor for ship ventilation. He returned to experiments on axial-flow compressors in 1897, and made an eighty-one-stage machine in 1899, which attained 70 percent efficiency. By 1907 his company had made or had on order forty-one axial-flow compressors, but they were plagued by poor aerodynamics. Parsons used far too high a spacing/chord ratio for the rotor-blade settings, and all bade rows were likely be stalled over much of the operating range. Parsons returned to making radial-flow compressors.

The other major pioneer working on compressors at that time was Auguste Rateau, who published a major paper on turboblowers in 1892. However a turbocompressor he designed to give a pressure ratio of 1.5 at 12,000 rpm and tested in 1902 gave an isentropic efficiency of only 56 percent. Subsequently, Rateau designed and built compressors of increasing pressure ratio and mass flow, and gradually increasing efficiency. The continued story of compressor development is largely involved with the long struggle to produce a working gas-turbine engine. Many attempts failed simply because of poor compressor efficiency.

1.2 COMPRESSOR THEORY

To better understand a turbomachine's performance, one must approach by the means of thermodynamics and fluid mechanics. The conservation of mass, energy, momentum and angular momentum in addition to 1st and 2nd laws of thermodynamics are the basic laws that govern the operation of the compressor. Since the operating fluid is air, the perfect gas and isentropic laws will be completing conservation laws. Figures 1.1 shows schematics of a single stage with components, corresponding velocity triangle (without inlet prewhirl) and a typical h-s diagram.

As is known from thermodynamics, the shaft work input to the compressor is transformed to build up pressure in the fluid while passing through the impeller passages. A simple angular momentum shows that

$$W_c = u_2 C_{u2} - u_1 C_{u1} \tag{1.1}$$

On the other hand, from the first law of thermodynamics and ideal gas law

$$W_c = h_{02} - h_{01} = C_p (T_{02} - T_{01}) \tag{1.2}$$

3

Equations (1.1) and (1.2) are the principles of this energy transformation. Note that the total (stagnation) temperature in an adiabatic machine changes where the shaft work is present, otherwise, it stays constant. Once the work input is defined, efficiency must be defined to distinguish between the ideal and actual work. Note that there are various definitions of efficiency and the general definition of compressor isentropic efficiency is

$$\eta_c = \frac{Idealwork}{Actualwork} = \frac{h_{02s} - h_{01}}{h_{02} - h_{01}} \tag{1.3}$$

$$\eta_c = \frac{\left(\dfrac{P_{0,out}}{P_{0,in}}\right)^{\frac{k}{k-1}} - 1}{\dfrac{T_{0,out}}{T_{0,in}} - 1}$$

The efficiency defined by (1.3), although fundamentally valid, can be misleading if used for comparing the efficiencies of turbomachines of differing pressure ratios. Any turbomachine may be regarded as being composed of a large number of very small stages irrespective of the actual number of stages in the machine. If each small stage has the same efficiency, then the isentropic efficiency of the whole machine will be different from the small stage efficiency, the difference depending upon the pressure ratio of the machine. There are correlations to convert the isentropic efficiency to Polytropic; however, the concept is utilized with perfect gas law to be helpful in defining the properties across the stage and impeller. Having the stage pressure ratio, the designer is able to derive the following correlation

$$\left(\frac{T_{08}}{T_{01}}\right) = \left(\frac{P_{08}}{P_{01}}\right)^{\left[\frac{R}{C_p}\frac{1}{\eta_p}\right]} \tag{1.4}$$

The same is valid across the impeller

$$\left(\frac{T_{02}}{T_{01}}\right) = \left(\frac{P_{02}}{P_{01}}\right)^{\left[\frac{R}{C_p}\frac{1}{\eta_P}\right]}$$ (1.5)

Utilizing equations (1.1)-(1.5) and knowing the desired stage pressure ratio and inlet total properties, a designer will be able to calculate the key properties at every location in the stage.

The other fact to be considered is slip factor (Figure 1.2). Even under ideal (frictionless) conditions, the relative flow leaving the impeller of a compressor will receive less than perfect guidance from the vanes and the flow is said to slip. Therefore, slip factor is defined to correct value of the energy transfer between the impeller and the fluid. There are various correlations for slip factor in the literature, following, the below definition has been referred by many authors to predict the best slip condition.

$$\sigma_w = \left[\frac{C_{u_2,\,actual}}{C_{u_2,\,theory}}\right] = 1 - \frac{\sqrt{Cos\beta_2}}{Z^{0.7}}$$ (1.6)

The other characteristic of a compressor is shown in its performance diagram (Figure 1.4), where the pressure ratio is drawn versus flow the coefficient. The diagram has the significant information regarding the range of operation, which lies between surge and choke lines and the area of maximum efficiency, Dixon (1998). One of the major issues in compressor operation is surge and choke limitation. For the compressor, efficient operation at constant $N/\sqrt{T_{01}}$ lies to the right of the line marked surge. For multistage compressors it commences approximately at the point where the pressure ratio flattens out to its maximum value. The surge line denotes the limit of stable operation of a compressor, where unstable operation is characterized by a severe

oscillation of the mass flow rate through the machine. The vertical portions of the constant speed lines may recognize the choke regions of the flow. No further increase in the flow coefficient is possible since the Mach number across some section of the machine has reached unity and the flow is choked.

1.3 COMPRESSOR COMPONENTS

1.3.1 INLET

A well-designed inlet system, which includes a bell mouth and inlet guide vane (IGV), will provide a uniform non-swirl flow to the impeller. To achieve high performance, the curvature of the bell mouth should be against any separation effect at the inlet. In some designs for better performance of the impeller, the inlet guide vanes will provide the required flow angle at the inlet to the impeller. The most important fact in designing the inlet system is to keep the relative Mach number as low as possible. This will provide the required mass flow rate at the best efficiency point and minimize the blade incidence and frictional losses in the following impeller passage.

1.3.2 IMPELLER

There is an extensive literature about the impeller design, performance and optimizations such as Bhinder et. al. (1987) and Palmer et. al. (1995). The impeller is where the energy is transferred and transformed. The fluid entering the passage will experience Coriolis force and at the same time diffusion through the passage. As mentioned in the previous section, losses will accompany this diffusion, which is

reflected in the efficiency concept. At the outlet of the impeller, slipping occurs, which is the result of loss, where all equations (energy, mass, momentum) must be satisfied.

The key parameters are the angles at the inlet and outlet of the impeller and the axial length of the impeller. One can utilize any of the optimization techniques in the literature to design the angular variation of the passages from inlet to outlet. Blades are designed in various types of radial, backward and forward swept blades. Radial blades are able to create a high-pressure ratio but create significant amount of loading on the impeller. Radial blades reduce the stress in high-pressure ratios but circulation and separation in the rotor channels are inevitable. Forward swept blades theoretically has the largest pressure ratio, however, current research was not able to put these impellers in use. Backward swept blades will reduce the discharge absolute Mach number and has a broader stable operating range. Since the streamline curvature in the blade to blade plane is increased in these type of blades, the blade to blade pressure gradient is reduced, therefore, the secondary flows and associated losses is avoided. However, in these types of blades, the blockage of the flow path must be considered.

The other factor in the impeller design is the number of the blades. Based on the impeller discharge flow angle, a zone of acceptable performance is defined for the number of the blades, described in Wilson (1998). The higher number of blades for certain angles, the higher blockage of the flow in the impeller passages will be created. The lower this number, the higher blade loading will be. Meanwhile, this number is selected in the way that half of the blades will behave as a splitter blades. These blades will reduce the loading on the blade. More details regarding the selection of the angles will be discussed later in the chapter.

1.3.3 DIFFUSER

Flow leaving the impeller carries kinetic energy, which is transformed inside a radial diffuser. Diffusers are classified as vaned and vaneless. If the flow leaving the impeller has a steep angle, using vaned diffuser avoids significant losses because of the longer residence time of the flow inside the diffuser. If the flow angle at the impeller discharge is not large, using the vaneless diffuser will help diffuse the flow and transform the rest of the kinetic energy left in the flow. The radial-flow component diffuses because the area increases, and this component have a low Mach number even when the Mach number based on the overall velocity vector is above unity. In axisymmetric flow the pressure gradient is in the radial direction and acts on this radial component. The tangential-velocity component diffuses because in axisymmetric flow, and in the absence of turning vanes and wall friction, the tangential velocity is inversely proportional to the radius. It is unaffected by the area change. This component of the velocity vector can pass from supersonic to subsonic without shock since it can adjust to direction changes from signals received through the subsonic radial component. The governing law is the conservation of angular momentum in vaneless diffusers, which is

$$r_3 C_{u3} = r_4 C_{u4} \qquad (1.7)$$

However, equation (1.7) is for the ideal case and normally there are losses due to the friction. In addition, in the area 2-3 (Figure 1.3) there is an unsteady mixing region, which creates its own loss.

Jansen (1964) reports the best analysis of vaneless diffusers, which has been endorsed by many researchers (Figure 1.5). In his analysis, the performance of the radial vaneless diffusers has been analyzed based on the Reynolds number of the impeller

8

discharge flow, the ratio of the discharge passage width to the radius of the impeller at the exit, and the blade angle at the discharge. Knowing this information, the designer will be able to have the best ratio of the diffuser radius to the impeller discharge radius as the matter of diffusion quality.

1.3.4 BEND AND RETURN CHANNEL

There is a lack of research in this area primarily because of the complication of the flow in this region and its inaccessibility. The flow passing through the bend, experiences pressure gradient across the channel and this pressure gradient creates a highly rotational flow and great pressure loss. To design these components one must rely on empirical correlations such as those described in Aungier (1995).

1.3.5 VOLUTE

The volute surrounds the impeller, and is a spiral casing whose cross-sectional area increases from a minimum at the cutwater to a maximum at the throat, which is the beginning of the conic diffuser to the outlet pipe. The cutwater is the nearest component of the casing to the impeller, and is aligned into the general direction of the flow leaving the impeller. The cross-sectional area increases to take the volume leaving the impeller. If the ideal flow is considered, the law of constant angular momentum will apply, and the flow will leave the impeller on a logarithmic spiral path. In many casing designs, the cross-sections are circular sections, and the outer wall follows an Archimedean spiral. It is possible, using integration across each section of small elements, to evaluate the area changes and get the correct areas for designated sections. In the governing laws, the

effect of friction is typically neglected as it has been found to affect the areas by very small amounts. However, because of the curvature of the casing, the flow spirals inside the volute, which requires a full three dimensional analysis to study it. There will be a comprehensive discussion on the volute geometry and design procedure in the next chapter.

1.4 A TYPICAL PRELIMINARY DESIGN PROCEDURE FOR A TWO STAGE CENTRIFUGAL COMPRESSOR

There are various ways of designing a centrifugal compressor in one dimension or mean radius values. The following is one of typical design procedure in which the main goals of designing a centrifugal compress are:

- Reducing the relative Mach numbers at the inlet to the stage in order to avoid high losses in the impeller.

- Minimizing the kinetic energy at the outlet of the diffuser and volute.

- Enforcing the optimized geometry parameters, in order to create an optimum performance, such as flow angles and radius ratios.

In the next sections a two-stage compressor (Figure 1.4) will be designed in order to familiarize the reader with the methodology since this is going to be the basis of the meanline analysis of the Trane compressor in Chapter 4. In this design procedure frictionless flow is considered and for explicit design the empirical correlation should be used to consider related losses. Although the design is ideal, it can be used for a designer to have a starting point.

1.4.1 FIRST STAGE

To start the design process the mass flow rate, inlet total pressure and inlet total temperature are considered given. Suppose the desired pressure ratio for the compressor is 7.5 where by dividing it between two stages, the first stage pressure ration is 2.8 and the second stage is 2.7. Note that in designing a two-stage machine, either the overall pressure ratio or work input is divided between the two stages. In order to start the iteration process, designer should start with selecting an inlet absolute velocity C_1 or Mach number M_1; correspondingly, the other parameters will be calculated knowing the initial guesses. The absolute velocity should be selected first. Knowing the inlet conditions, one can obtain the static temperature

$$T_1 = T_{01} - \frac{C_1^2}{2C_P} \tag{1.8}$$

Knowing the static pressure, the speed of sound and Mach number can be calculated

$$a_1 = \sqrt{\gamma RT}$$
$$M_1 = \frac{C_1}{a_1} \tag{1.9}$$

In order to calculate the relative and tangential velocities, the velocity triangles must be obtained by calculating the corresponding the flow and impeller angles. The inlet velocities can be assumed swirl free by using IGV, which means α, the absolute velocity angle respect to radius, at both stage's inlets is zero. Meanwhile, the blades are selected to be radial at the hub and backward swept at the shroud. Therefore, β, the angle of relative velocity respect to radius, at the hub is zero for both stages. It is shown in various literatures that the flow angle leaving the impeller (β=60) degree at the shroud

will optimize the performance; therefore, it is assumed the same amount as the initial guess. Having this angle, the inlet velocity triangle can be defined.

$$W_{s1} = \frac{C_1}{Cos\beta_{s1}}$$

$$U_{s1} = C_1 Tan\beta_{s1}$$

(1.10)

Using the perfect gas law, total density can be calculated.

$$\rho_{01} = \frac{P_{01}}{RT_{01}}$$

(1.11)

Having the absolute Mach number, the static density can be calculated.

$$\frac{\rho_{01}}{\rho_1} = \left[1 + \frac{M_1^2}{2\left(\frac{C_p}{R} - 1\right)} \right]^{\left(\frac{C_p}{R} - 1\right)}$$

(1.12)

Volume flow rate can be calculated from

$$Q = \frac{\dot{m}}{\rho_1}$$

(1.13)

The number of the blade Z is chosen to be 20, which puts the impeller in the accepted region of Wilson (1998) chart. Then the slip factor can be calculated using (1.6). It is shown in literature that selection of 60 and 45 degrees for α and β at the impeller discharge would be good initial guesses. Therefore using the velocity triangle at the outlet and considering slip factor the following correlation can be used.

$$\left[\frac{C_{u2,ac}}{U_2} \right] = \left\{ \frac{Tan\beta_2}{Tan\alpha_2} + \frac{1}{\sigma_w} \right\}^{-1}$$

(1.14)

On the other hand, with no swirl at the inlet

$$\Delta h_0 = U_2 C_{u2} - U_1 C_{u1} = U_2 C_{u2}$$

(1.15)

As mentioned before

12

$$\Delta h_0 = C_P (T_{02} - T_{01}) \tag{1.16}$$

Using the efficiency concept (1.3) Δh_0 can be calculated, knowing that the total temperature stays constant from first stage impeller outlet to the inlet of the second stage. Using (1.13) and (1.14) the tangential velocity and blade speed at the outlet will be calculated.

Rodgers [32] showed that the specific speed of 0.8 is a good assumption to have an optimum performance. Knowing that, the rotational speed can be calculated using the following correlation.

$$N = \frac{60 N_s (\Delta h_0)^{\frac{3}{4}}}{2\pi \sqrt{Q}} \tag{1.17}$$

Therefore, the angular velocity can be calculated correspondingly. The diameter of the impeller at the inlet can be calculated as following

$$d_2 = \frac{2U_2}{\omega} \tag{1.18}$$

Knowing the angular speed and (1.9), the diameter of the shroud can be similarly calculated. To calculate the hub diameter, the result of the previous studies will be used as was shown that a ratio of hub to shroud diameter range of 0.3-0.5 creates a reasonable balance between the blockage and high inlet velocity, Wilson (1998). Therefore by choosing this ratio, the hub diameter can be calculated as well. Note that using Microsoft Excel sheets, all these parameters cab be assigned with their corresponding equations. At the end of the calculations, a conservation law such as conservation of mass can be used to confirm the first initial guess; otherwise, an iteration process will take place with changing the parameters. The choices of the parameters will be used as an initial guesses

and based on the outcome of the design, they may be modified as the iteration goes along.

Using the velocity triangle information at the inlet, the absolute and relative velocities will be calculated.

$$C_2 = \frac{C_{u2}}{Sin\alpha_2}$$

$$W_{u2} = U_2 - C_{u2}$$

$$W_2 = \frac{W_{u2}}{Sin\beta_2} \tag{1.19}$$

$$C_{r2} = C_2 Cos\alpha_2$$

The static temperature and thus the absolute and relative Mach numbers will be calculated similar to (1.7) and (1.8). Defining the thickness of the blade, the width of the impeller discharge can be calculated by conserving the mass flow rate.

$$A_{flow2} = \frac{m}{\rho C_{r2}}$$

$$b_2 = \frac{A_{flow2}}{(\pi d_2 - \frac{Zt_2}{Cos\beta_2})} \tag{1.20}$$

The width could have been calculated from choosing a proper ratio of width to diameter of the impeller at the discharge but (1.19) will save iteration. Knowing the width, the blockage areas can be calculated.

$$A_{b1} = \frac{Zt_1}{Cos\beta1}(d_{s1} - d_{h1})$$

$$A_{b2} = \frac{Zbt_2}{Cos\beta_2} \tag{1.21}$$

This iteration process must be implemented until the mass flow rate conserved as stated earlier.

Presented in various literatures, it is shown that to have a good performance diffuser, the ratio of the relative velocities at the impeller discharge to the inlet must be greater than 0.6. This ratio can be a strong design condition to be conserved; otherwise, a supersonic relative velocity will choke the flow at the inlet of the impeller. At the same time, the size of the impeller has a direct influence on the required speed of the compressor. The higher the rotational impeller speed, the more stress on the impeller.

Knowing all parameters at the impeller discharge, the diffuser must be designed. In order to accommodate the mixing region at the impeller discharge, one percent of the impeller radius can be designated for the mixing region; however, there are ongoing researches for more accurate design of this region. In order to calculate the required diameter of the diffuser, the absolute Mach number at the diffuser discharge is set to be 0.25, which is a reasonable value in order to guarantee the transformation of the kinetic energy inside the diffuser as much as possible. Knowing the Mach number leads to definition of the static temperature at the diffuser discharge.

$$\frac{T_{04}}{T_4} = 1 + \frac{\gamma - 1}{2} M_4^2 \qquad (1.22)$$

Knowing the both static and total temperature and using (1.7), the absolute velocity at the diffuser discharge can be calculated. Meanwhile, calculating the Reynolds number at the impeller discharge and utilizing the data in Wilson (1998), one can calculate the ratio of the diameters of diffuser to impeller. This ratio will guarantee the acceptable performance of the diffuser.

From stage and impeller efficiencies, which are desired parameters in the design, the total pressures at the impeller discharge and inlet to the second stage will be known. The difference between two values is the pressure loss across the diffuser, bend, and

15

return channel. Therefore, the properties of the fluid can be calculated at every location. On the other hand, knowing the velocities at the inlet and outlet of the diffuser, the conservation of the mass (1.23) can be used to calculate the flow angle at the diffuser outlet.

$$\rho_2 A_2 C_{r2} = \rho_4 A_4 C_4 Cos\alpha_4 \qquad (1.23)$$

Note that in some designs, pinching has been used in design of the vaneless diffuser walls but for the simplicity in this design, the width of the diffuser can be kept constant.

In the bend section, the inner radius of the bend is kept as the average of the width at the diffuser inlet and discharge, referring to Aungier (1995). Since the width of the duct is kept constant across the diffuser to the end of return vane, the radius of the shroud side of the bend chosen to be equal to the two times width.

In order to adjust the flow angle for the second stage, vanes are used in the return channel. In this design, the leading edge of the vanes in the return channel is located where the bend is terminated. The angle of the leading edge is the same as the angle of the flow leaving the bend. The thickness of the vanes will be equal to the width of the duct. Since the flow at the inlet of the second stage impeller can be designed to be swirl free, the return vanes must guide the flow to zero degree angle respect to the radius. To accommodate this turn smoothly, the vanes are designed to be long enough in order to avoid high pressure losses. Similar to the bend, there are ongoing research to investigate the effect of various vanes in this section on the compressor performance.

1.4.2 SECOND STAGE

To design the second stage, the process is similar to the first stage except volute replaces the bend and return channel. Note that all the fluid properties will be known through the Mach numbers, total properties and velocities at the different components of the second stage.

In the volute section, it is proven that the circular cross section has the lowest loss (Chapter 3), therefore, in the current design circular cross section has been chosen. To design the volute, the iteration process should be implemented to calculate the radius and the area of the throat. The conservation of the angular momentum is valid here as well.

$$r_{11}C_{u,11} = r_C C_{u,th} \tag{1.24}$$

At the same time, conservation of mass leads to

$$\frac{A_{th}}{r_C} = \frac{C_{r,11}b_{11}\pi d_{11}}{r_{11}C_{u,11}} \tag{1.25}$$

Choosing the radius of the throat and applying the conservation of mass can calculate the throat area. Meanwhile, no blockage at the tongue has been considered, therefore, for simplicity of the design, a linear distribution of the area has been chosen for the volute.

For the conical diffuser, the next component attached to the volute, it is shown that the best design is to keep 2θ, the divergence angle of the cone, less than 7 degree in order to avoid stall in the diffuser. The cone's function is to transform the rest of the kinetic energy left in the flow to pressure as much as possible. Knowing the pressure loss, the area ratio and the length of the diffuser at the end of volute can be calculated.

1.5 SIGNIFICANCE OF THE VOLUTE AND CURRENT CHALLENGES

As mentioned previously, the primary function of a centrifugal compressor volute is to serve as the transition from the impeller and diffuser to the pipe system. Depending on the particular configuration, the losses in volutes especially at off-design can be significantly high which leads to poor stage efficiency and reduction of operating range.

It is well known, that the collecting volute of a centrifugal compressor operating at off-design conditions, produces a peripheral pressure distortion. This pressure distortion intensively acts back on the impeller exit, when a vaneless diffuser is chosen and leads to a periodic throttling of the impeller flow. This results in a cyclic acceleration and deceleration of the fluid inside each impeller channel. As a result, the inlet flow angle and thus the incidence angle vary periodically, which is the reason for a decrease of impeller efficiency and operating range. The varying force that acts on the impeller blades can cause impeller failure especially when high inlet pressures are considered.

Several simplified one- or two-dimensional models exist that predict the peripheral pressure distortion caused by the volute. However, measurements of Van den Braembussche and Handle (1990) and Ayder et al. (1991, 1993) clearly show the fully three-dimensional nature of the volute flow. The secondary flow inside the volute has a major influence on the pressure distortion and on the distribution of the through flow velocities. This implies that a reliable prediction method must be considered the 3-dimensional character of the flow. Van den Braembussche et al. (1998) present an analytical quasi-one dimensional prediction method, which takes into consideration the

18

three dimensionality of the flow. A reasonable correspondence of the pressure distribution and losses with the experimental results obtained at the large centrifugal compressor test stand of the Institute of Turbomachinery in Hanover.

Ayder et al. (1994) used a steady 3D Euler-method for the calculation of the diffuser and volute flow of a compressor with elliptic volute. They introduced an artificial dissipation term in their calculations in order to limit the flow quantities in the vortex core to finite values. Generally good agreements with the measurements results were obtained. The calculated total pressure distributions were less accurate.

There are quite few measurement results available of the flow inside the volute. The works of Van den Braembussche and Handle (1990), Ayder et al. (1991, 1994) and Ayder (1993) provide good insight to the flow behavior inside the volute in typical geometries, such as circular or elliptic, at nominal and off-design operating points. Nevertheless, Trane's volute is a combination of rectangular and circular cross-sections, which can affect the general flow structure and loss mechanism. Therefore we are far from fully understanding the flow phenomena and loss mechanism inside the volute and further empirical data are necessary to improve the existing flow models.

FIGURES

Figure 1.1: Schematic of a single stage centrifugal compressor with corresponding velocity triangle and h-s diagram

β'_2: Vane Angle

β_2: Average Relative
Flow Angle
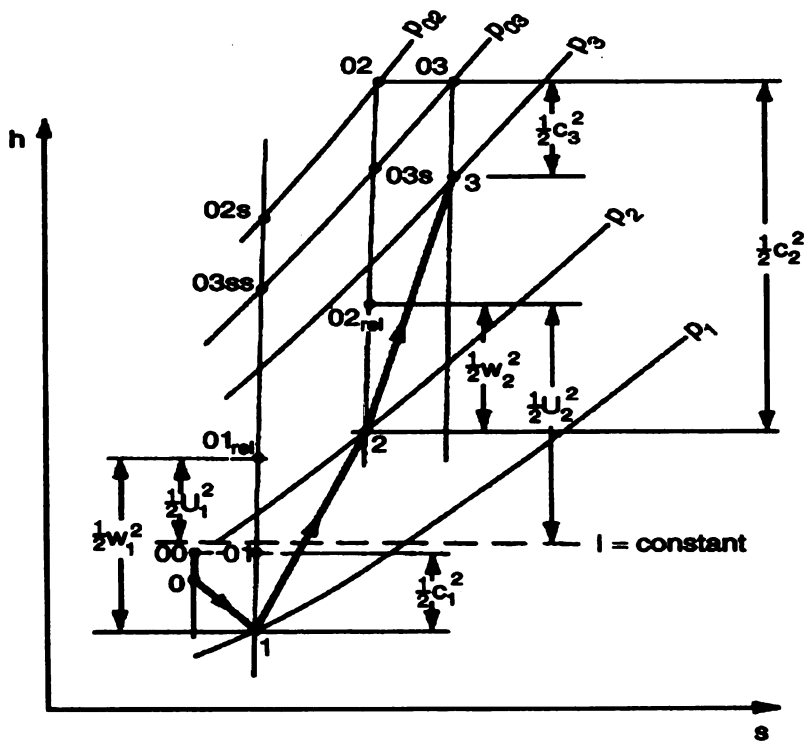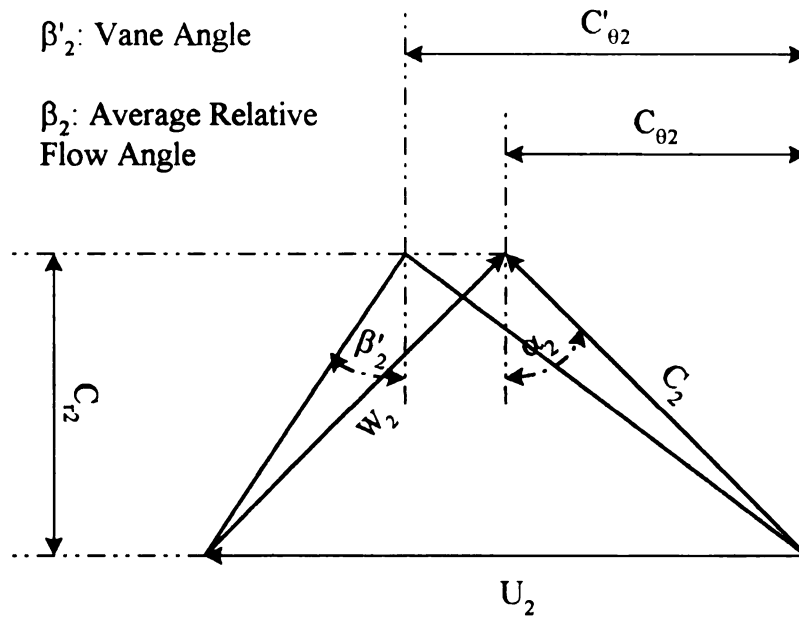
Figure 1.2: Velocity triangle with slip
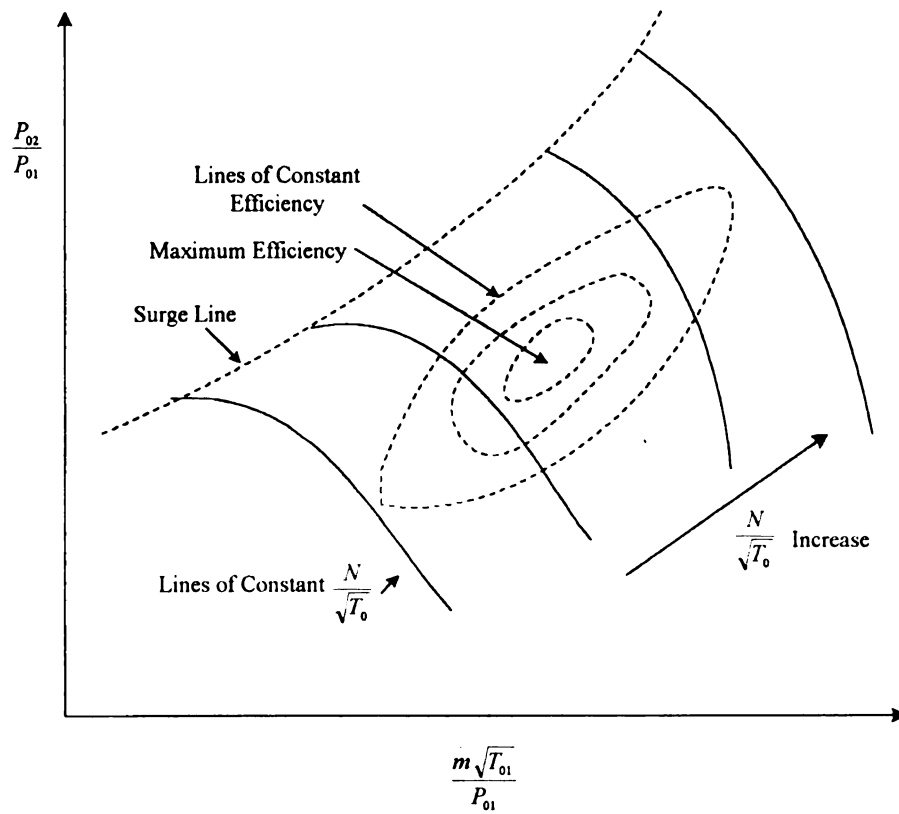
Figure 1.3: A typical compressor performance map

22
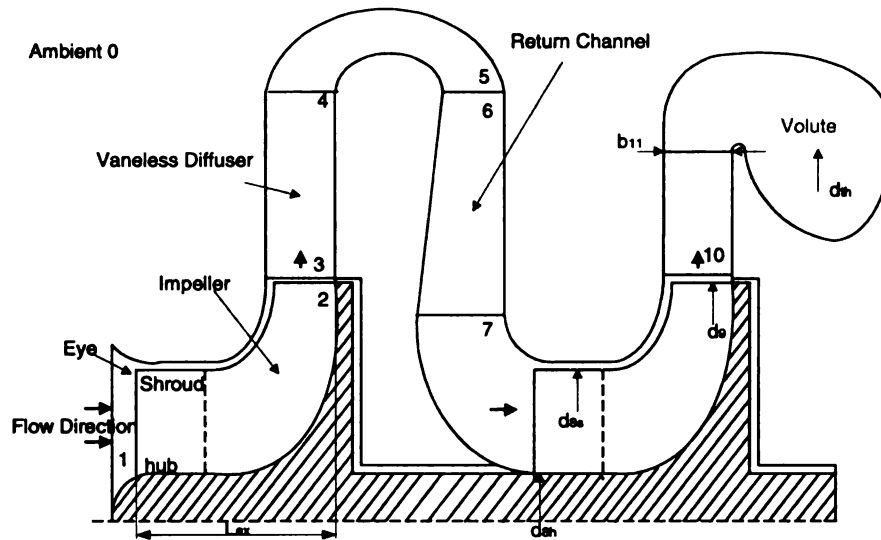
Figure 1.4: Schematic of a two stage centrifugal compressor
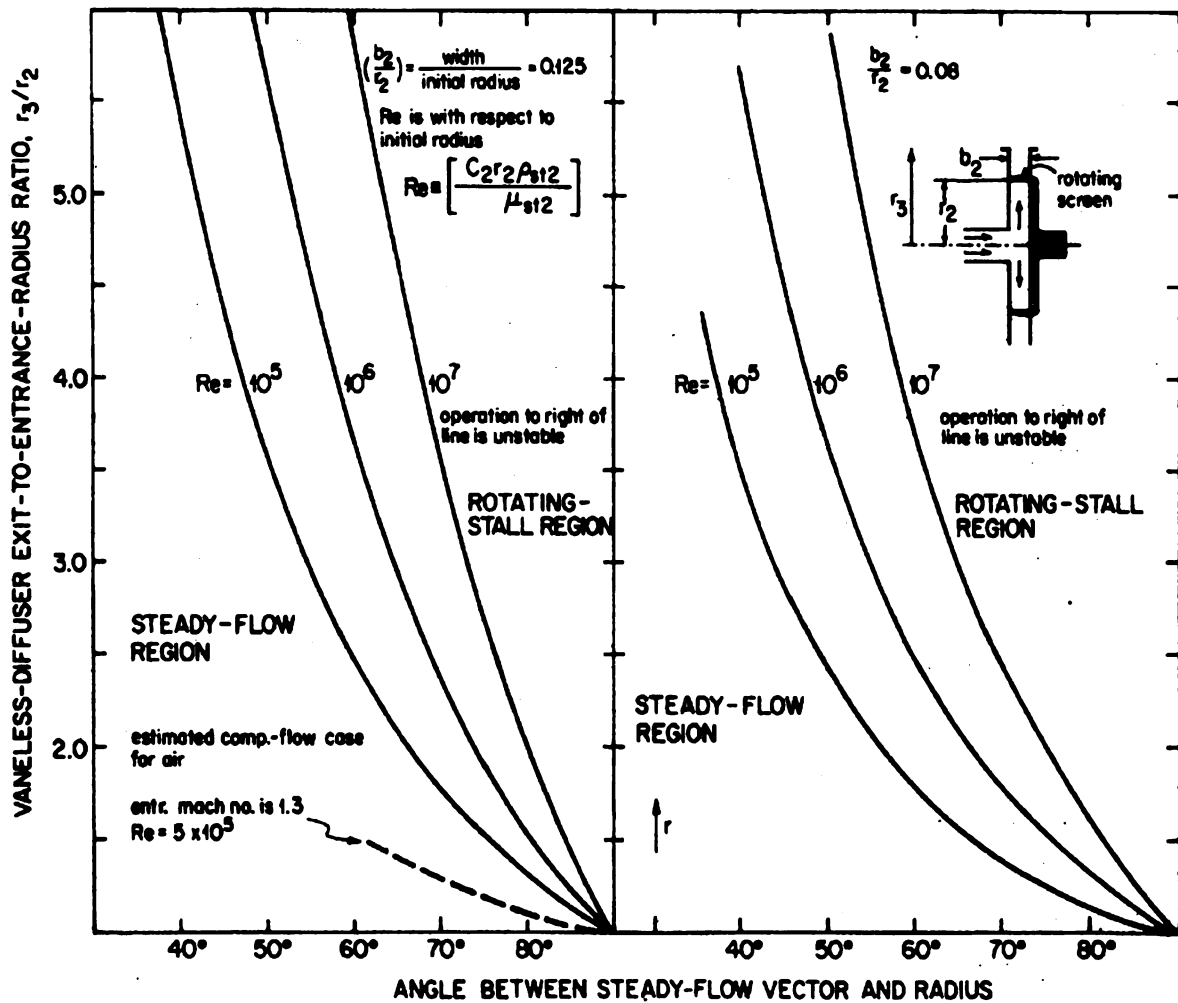
Figure 1.5: Stable operating range of vaneless diffusers. From Jansen 1964

CHAPTER 2

LITERATURE SURVEY

In this chapter the literatures were reviewed extensively. The material gathered in this chapter is focused on the volute design methodologies and performance analysis performed by different researchers. Various models for losses in radial diffusers, volute, conic outlet and their interactions with the impeller and the stage are introduced.

2.1 FLOW IN COMPRESSOR VOLUTE

As described previously, the flow leaving the impeller is collected by the volute and delivered to the compressor outlet pipe. Circumferential volute area distribution is designed to produce minimum static pressure distortions at minimum loss. However, in conic diffuser, one should see a kinetic energy exchange.

2.1.1 FLOW MECHANISM

The flow leaves the impeller at a fairly constant angle over the whole periphery, with the fluid particles following spiral trajectories. Entering the radial diffuser of the volute, the flow is decelerated and based on the conservation of angular momentum equation the pressure increases.

The flow inside the volute is highly three-dimensional and swirling. Described by Ayder and Van den Braembussche (1993), the volute flow is made of layers of non-uniform total pressure and temperature with high shear forces at the volute center. Entering the volute, the fluid starts rotating around the cross section area, giving rise to large velocity gradients and shear stresses. The fluid entering close to the tongue develops a vortex flow and remains in the center of the volute as it proceeds towards the conic diffuser. Further downstream flow wraps around the previous one, generating a structure similar to vortex tubes of increasing radius (Figure 2.1, 2.2).

Turbulence mixing occurs between the high-energy fluid at the center of the volute and the low-energy fluid in the boundary layers, resulting in mixing losses. The boundary layer at the volute walls is absorbed by new fluid coming out of the vaneless diffuser after each rotation and the incoming fluid mixes with the flow already streaming through the volute.

The amount of fluid entering the volute has an enormous effect on the flow. At higher than optimum mass flow rate, the fluid is accelerated from the volute inlet to the exit pipe; if the mass flow is lower than optimum, the flow is decelerated throughout the volute. Secondary flow inside the volute occurs as the friction-decreased boundary layer flow has the pressure distribution of the core flow. Therefore, the flow close to the wall streams to the volute center mixes with the core flow and is thrown back towards the volute wall. A twin vortex is formed in a symmetrical volute and a single vortex appears in the asymmetrical one.

Huebl [29] measured the flow parameters of two volutes with the same circumferential variation of the cross sectional area but different inlet positions, one being a symmetrical and one being an asymmetrical volute (Figure 2.37). The flow in the symmetrical volute has a completely different structure than the flow in the asymmetrical one. Asymmetrical volutes show a higher efficiency than symmetrical volutes owing to the formation of a single vortex in the asymmetrical volute instead of the double vortex in the symmetrical one. The formation of the double vortex can be explained by the fact that the sharp edge at the radial diffuser exit prevents the flow to be attached to one side of the volute.

Hagelstein [29] reports that a part of the pressure developed in the radial inlet diffuser prior to the volute, is lost in an internal volute. This is because of smaller curvature radius of the streamlines in the volute than in the radial diffuser, resulting in velocity increase and pressure drop. Compared to external volutes, the increase in velocity results in higher wall friction losses and greater velocity reduction in the exit conic diffuser, which contributes to the exit cone losses. Another reason for the high losses in an internal volute is the radial velocity component of the flow at the radial diffuser exit. Leaving the diffuser, the radial velocity component is transformed into a swirl flow, increasing friction losses.

2.1.2 STATIC PRESSURE DISTRIBUTION

At optimum mass flow rate, there is a uniform circumferential pressure distribution at the volute inlet, which leads to an almost uniform total pressure over each cross section. As described by Van den Braembussche (1998) there is only a small pressure gradient from the volute wall to the center due to the small swirl velocity shear losses (Figure 2.4) and a change in the circumferential pressure distribution due to the flow perturbation near the tongue.

With the mass flow rate being higher than optimum, losses increase because of large velocity gradients and shear stresses. The volute is now too small to accumulate the flow; therefore, the flow accelerates and results in decrease of total pressure from the volute inlet to outlet. Van den Braembussche (1998) reveals with his measurements, that at the volute inlet sections both the static and the total pressure decrease from the volute wall to the center. This results in a nearly uniform through flow velocity distribution. At

the downstream volute sections the static pressure decreases towards the center of the volute while the total pressure increases, resulting in a through flow velocity which is twice as large as the one at the volute inlet.

The relation between the through flow velocity and the static and total pressure distribution is shown by the following equation:

$$p_0 - p = \frac{\rho}{2}\left(v_T^2 + v_S^2\right)$$

(2.1)

The static pressure variation at high mass flow results from the swirl and the circumferential curvature of the volute walls (2.2)

$$\frac{dp}{dr} = \rho\frac{v_S^2}{r}$$

(2.2)

with the centrifugal forces due to swirl being in equilibrium with the static pressure increase from the center to the outer walls.

At low mass flow, the volute acts like a diffuser and the static pressure increases from the volute inlet to the outlet. A decrease of total pressure occurs at the center of the cross-section due to internal shear stresses. The static pressure distribution at low mass flow rates is primarily defined by the following equation, which describes the pressure gradient between the inner and outer wall caused by the through flow velocity distribution and the circumferential curvature R_c:

$$\frac{dp}{dR} = \rho\frac{v_T^2}{R_c}$$

(2.3)

Elholm et al. (1992) and Ayder, Van den Braembussche (1993) discovered a sudden pressure drop over the tongue at a low mass flow rate, as a result of an extra amount of fluid entering the volute through the clearance at the volute tongue. At a high

mass flow rate a pressure rise at the volute tongue occurs, pushing the fluid back from the inlet to the exit pipe. The non-uniform circumferential pressure distributions at high and low mass flow rates lead to a periodic change in flow conditions at the impeller outlet. This causes periodic changes in the blade load resulting in radial forces on the impeller shaft.

2.1.3 VELOCITY DISTRIBUTION

At the impeller exit, the radial velocity is transformed into a swirling motion with a forced vortex type of velocity distribution in the center of the volute and a constant swirl velocity away from it. The through flow velocity in the volute follows the angular momentum conservation equation;

$$R \cdot v_T = const \tag{2.4}$$

The variation of the through flow velocity is due to the curvature of the volute with the through flow velocity decreasing from the inner to the outer volute wall and minimum through flow velocity occurring at the center of the vortex. The dependence of swirl and through flow velocity from total and static pressure can be revealed by equations (2.1), (2.2) and (2.3).

Van den Braembussche (1998) describes the flow in the volute consisting of vortex tubes of increasing radius (Figure 2.2) with the swirl velocity v_S at a given radial position depending on the radial velocity of the fluid at the position where it has entered the volute. The velocity distribution inside the volute (Figure 2.7) distinguishes itself enormously for optimum and off-design mass flow. At optimum mass flow rate, the velocity near the walls is nearly constant due to the constant circumferential velocity

distribution at the volute inlet. The uniform pressure distribution at the volute inlet with optimum mass flow rate condition leads to an almost uniform through flow velocity at each cross section with only a small increase towards the center of the volute. Lower radial velocity at the volute inlet results in smaller swirl velocity throughout the volute circumference (Figure 2.6).

Fluid entering the volute at higher than the optimum mass flow rate has a small tangential and a large radial velocity component. Due to the negative incidence of the flow at the volute entrance and because the volute is too small for the amount of mass flow, the through flow velocity increases from the volute tongue to the exit. The large radial velocity leads to a high swirl velocity formation, which increases with the cross-section radius.

At lower than the optimum mass flow rate, the flow enters the volute with a positive incidence leading to an acceleration of the flow around the tongue and a deceleration towards the volute exit. This deceleration is due to the volute being too big for the small amount of flow. The flow has a large tangential and small radial velocity component with the volute acting like a diffuser as the tangential velocity decelerates from the volute tongue to the exit. Near the walls, a constant swirl velocity occurs as a result of the uniform radial velocity at the volute inlet. Due to the large tangential velocity the static pressure distribution is mainly defined by equation (2.3).

The pressure drop at low mass flow rate and the pressure rise at high mass flow around the tongue described by Elholm (1992) has an effect on the position of the swirl center inside the volute (Figure 2.7). For high mass flow rate, the swirl center is pushed further inside the volute and for low mass flow rate it is located closer to the volute inlet.

Observed by Ayder et al. (1992), the flow entering close to the tongue has a large swirl velocity and a small through flow velocity so that the static pressure distribution in the tongue area is primarily given by equation (2.2). As found by Ayder (1993), none of the previously described calculation methods account for the effect of the cross flows on the volute flow because they all assume uniform flow over a cross section. Van den Braembussche et al. [40] have developed a method to predict the three-dimensional flow in a compressor volute.

2.1.4 NUMERICAL ANALYSIS

Miner, Flack and Allaire (1992) calculated the velocity field in a centrifugal pump by using a two-dimensional potential flow analysis. The impeller and volute are modeled with the finite element method and the results included velocity profiles for the impeller and determination of the tongue stagnation point. Martinez-Botas, Pullen and Shi (1996) use a 3D Navier Stokes solver to calculate the flow in a turbine volute. Their method solves the fully 3D Reynolds averaged Navier Stokes Equations. They conclude that by correctly treating the boundary conditions the results of the Navier Stokes solver are much better than the results of a free-vortex flow prediction.

Engeda (1995) examines the validity of compromise methods using 2D and 3D viscid and inviscid solutions to describe the flow in a volute. Ayder and Van den Braembussche (1993) use an Euler solver added by second order dissipation and wall shear forces to describe the flow in the compressor volute. The comparison between their model and measured data shows a good prediction of the velocity distribution and a more qualitative agreement of the pressure distribution. Ayder and Van den Braembussche

conclude, that their method, using the Euler solver with a volute adapted loss model, can be a good alternative to a method using the solution of the full Navier Stokes equations for which the computational effort would be much higher.

Carter (1981) solves the two dimensional Laplace equation to describe the volute flow. The solution is obtained by using the finite element method with variational principle, assuming ideal flow and design conditions. Carter uses the superposition method to simplify the implementation of the boundary conditions. Initially, only the radial flow components were considered and the tangential flow was calculated. To obtain the total flow properties, the two solutions were added together. His results for design flow are that the velocity follows the free vortex law except in the tongue region that the tongue clearance has a large effect on the volute flow and that the average velocity of the volute flow is determined by the spiral angle of the volute outer wall.

2.2 VOLUTE DESIGN

The main goal in volute design is to achieve a circumferential uniform static pressure over the impeller outlet, Eckert et al. (1961). If this is not accomplished, the flow inside the impeller vanes change their circulation with every rotation of the shaft leading to a development of vortices, which results in vane vibration and lower compressor efficiency. Therefore the fluid has to flow through the volute like a vortex source. The volute can be designed for constant velocity at the volute inlet. For an exact volute design it is yet necessary to account for friction and a change in flow density from the volute hub to the shroud.

Other design targets for compressor volutes are compactness and efficiency. The compactness is required for low cost and weight and is often in contradiction to the volute efficiency. Aspects of limited space to install the volute have to be considered as well.

2.2.1 VOLUTE GEOMETRY

To define the geometry of the volute, Eck [17] describes a simple vortex flow, which is symmetrical about an axis. He substitutes a streamline of the vortex source by a firm wall, which after a full rotation will confine the flow within the end section of the volute (Figure 2.8).

Eckert et al. (1961) calculate the streamlines of the volute flow, and therefore the outer wall of an external volute as logarithmic spirals (Figure 2.9). The cross-section shape of the volute can be rectangular, circular or elliptic. The advantage of a rectangular shape is that it is the easiest to manufacture. Most commonly used are volutes with circular cross-sections. Van den Braembussche (1998) expressed the reason, where volute losses are considered.

The volute cross-section can be symmetrical or asymmetrical. Asymmetrical volutes develop only a single secondary vortex flow. Volutes can be of external or internal type (Figure 2.10). In internal volutes, the flow undergoes a 90°-turn and is accelerated because these volutes have a smaller radius than the impeller exit. Internal volutes have the advantage of being much more compact than external ones. The flow accelerates when entering the volute due to the rotation law; thus, the volute has to be smaller than an external one. Impeller friction is smaller and the friction path is shorter

than for normal configuration. These advantages are yet balanced out by the large increase in friction due to the greater velocity. Therefore, external volutes are preferred because of their higher efficiency.

In addition, it is possible to subdivide the discharge section of the volute to a number of guide blades to further decrease in the discharge velocity. For very large volumes one can construct a volute with several subdivisions and partially profile the guide planes [17]. This results in comparatively small units. To minimize the losses in these volutes, Mueller [29] suggests the use of a volute casing with a number of discharge points disposed around the circumference. This kind of volute is often used for aircraft engine superchargers because of its numerous discharge points.

In order to handle mass flows at off-design conditions Eck [17] describes a volute with an adjustable tongue and Pfleiderer [29] gives data for the position of the volute tongue and states the tongue thickness for maximum efficiency.

2.2.2 1-DIMENSIONAL DESIGN

One of the primary equations used for the volute design is the incompressible continuity equation.

$$Q = \int c \cdot dA \qquad (2.5)$$

c is the through flow velocity for the differential area dA.

The predication of the continuity equation for the volute is that the mass flow in each circumferential cross section is the same, Eckert (1961). Due to the curvature of the volute walls, there is a rise in static pressure from hub to shroud. This results in a density change, which is yet neglected; because the pressure rise is small the meridional velocity

c_m is small compared to the circumferential velocity c_u. Therefore the continuity equation states

$$2\pi \cdot r \cdot b \cdot c_m = 2\pi \cdot r_3 \cdot b_3 \cdot c_{m3}$$ (2.6)

with the index (3) describing the conditions at the volute inlet.

The other equation is the conservation of angular momentum equation

$$c_u \cdot r = c_{u3} \cdot r_3$$ (2.7)

With these two equations a simple volute design can be performed. For some basic cross sectional shapes it is possible to calculate the boundary curves of the volute mathematically.

2.2.3 FRICTIONELESS DESIGN

Eck [17] and Eckert (1961) and Pfleiderer [29] provided mathematical solutions for the design calculation of volutes using the continuity equation and the angular momentum conservation equation:

- External volute with parallel sidewalls:

For parallel side walls with $b = b_3$ equation (2.6) changes to

$$c_m = \frac{r_3}{r} c_{m3}$$ (2.8)

The angle of inclination of the streamlines to the periphery is

$$\tan \alpha = \frac{c_m}{c_u}$$ (2.9)

Equations (2.7) and (2.8) show that $\tan \alpha = \tan \alpha_3$ and therefore that the angle of inclination is constant and with dr and $d\varphi$ as the differentials of the streamline

35

$$\tan \alpha = \frac{dr}{r \cdot d\varphi} \tag{2.10}$$

Integration of equation (2.10) results in

$$\ln \frac{r}{r_3} = \tan \alpha (\varphi - \varphi_3) = \frac{c_{m3}}{c_m}(\varphi - \varphi_3) \tag{2.11}$$

Which shows that the streamlines are logarithmic spirals. The streamline for $\varphi_3 = 0$ runs through the tongue of the volute and forms the outside boundary curve of the volute casing:

$$\ln \frac{r}{r_3} = \frac{c_{m3}}{c_m} \cdot \varphi \tag{2.12}$$

For volutes with parallel sidewalls that are wider than the impeller, equation (2.12) transforms to:

$$\ln \frac{r}{r_3} = \frac{c_{m3}}{c_m} \cdot \varphi \cdot \frac{b_3}{b} \tag{2.13}$$

If the flow parameters c_{m3} and c_{u3} and the geometrical parameters b_3 and r_3 are known, the width b of the volute can be calculated as follows. Assuming a square discharge area the volume of fluid exiting the volute is given by

$$Q = b^2 \cdot c \tag{2.14}$$

With c is the mean velocity, which is assumed to be equal to the velocity at the point of concentration of the discharge area, the volume flow rate at the volute exit equals to:

$$Q = b^2 \cdot \frac{c_{u3} \cdot r_3}{r_3 + (b/2)} \tag{2.15}$$

With $Q = 2\pi \cdot r_3 \cdot b_3 \cdot c_{m3}$, b can be obtained from:

36

$$b = \frac{\pi}{2}b_3\frac{c_{m3}}{c_{u3}} + \sqrt{\left(\frac{\pi}{2}b_3\frac{c_{m3}}{c_{u3}}\right)^2 + 2\pi \cdot r_3 \cdot b_3\frac{c_{m3}}{c_{u3}}} \qquad (2.16)$$

- External volute with rectangular cross-section

In volutes with rectangular cross-sections the conservation of angular momentum equation cannot be properly used here, because deviations from the law $r \cdot c_u = const.$ are to be expected. As an approximation for volutes with a radial extension that is not too large with respect to the radius, Eck [17] suggests the following calculation.

With $h/b = const.$ the circumferential velocity at any x location becomes

$$c_u = \frac{c_{u3} \cdot r_3}{r_3 + x} \qquad (2.17)$$

Using the continuity equation and $Q_\varphi = Q\frac{\varphi^\circ}{360}$ a solution for the problem can be provided

$$\varphi^\circ = \frac{360 \cdot c_{u3} \cdot r_3 \cdot h}{\overset{\bullet}{V} \cdot h/b}\ln\left(1 + \frac{h}{r_3}\right) \qquad (2.18)$$

- External volute with tapering side walls

Using equations (2.6) and (2.7), substituting b by

$$b = b_3 + 2(r - r_3)\tan\delta \qquad (2.19)$$

and solving the resulting differential equation one gets

$$\varphi = \frac{1}{\tan\alpha_3}\left[\left(1 - 2\frac{r_3}{b_3}\tan\delta\right)\ln\frac{r}{r_3} + 2\frac{r_3}{b_3}\left(\frac{r}{r_3} - 1\right)\tan\delta\right] \qquad (2.20)$$

The logarithmic term disappears for

$$\tan\delta = \frac{b_3}{2r_3} \qquad (2.21)$$

and modifies equation (2.20) to form the outer wall of a volute with tapering walls:

$$\varphi = \frac{1}{\tan\alpha_3}\left(\frac{r}{r_3} - 1\right)$$

(2.22)

- External volute with circular cross-section

Strictly spoken the conservation of angular momentum equation is not applicable on volutes with circular cross sections, because they have no body of rotation with reference to the sidewalls. Therefore the tangential force on the flow particles is existent and equation (2.8) is invalid. However the tangential force compared to the radial force is so small, that it can be neglected, and equation (2.8) can be used as an approximation.

A precise calculation of the volute with circular cross-section is possible but rather complicated. Therefore Eck [17] employed a linear approximation for the volute shape, when the diameter d of the volute section is not too large with respect to the casing diameter. The average velocity would then be equal to the velocity at the point of concentration of the area.

$$c_{av} = \frac{c_{u3} \cdot r_3}{r_3 + (d/2)}$$

(2.23)

Using the continuity equation for the flow through a cross-section at the angle φ, the volume flow rate $Q(\varphi)$ is

$$Q\frac{\varphi^\circ}{360} = \frac{\pi}{4}d^2 c_{av}.$$

(2.24)

With equation (2.24) the relation between φ and d can be calculated. For a solution of the equation Eck recommends to select d approximately.

- Internal volutes

Eck [17] describes the design of an internal volute with rectangular cross section and the mathematical calculation of the necessary geometrical parameters. At first there has to be a tongue section for an angle φ_0. At this angle the flow will enter the rectangular section of the volute with

$$\varphi^\circ = \frac{c_{u3}}{c_{m3}} \frac{b_3 + b}{b} \ln \frac{r_3'}{r_3} .$$

(2.25)

Using $Q_\varphi = Q\frac{\varphi^\circ}{360}$ to calculate the volume flow and equation (2.13) the equation for the internal volute is as follows:

$$\ln \frac{r}{r_3} = \varphi \frac{c_{m3}}{c_{u3}} \frac{b_3}{b}$$

(2.26)

Eckert et al. (1961) and Pfleiderer et al. [29] do not use a linear form of equation (2.8), but they assume its validity. With the continuity equation and equation (2.8) they receive

$$Q_\varphi = \int c_u \cdot dA = \int_r^{r_3} \frac{r_3}{r} \cdot c_{u3} \cdot b \cdot dr$$

(2.27)

Using $Q_\varphi = Q\frac{\varphi^\circ}{360}$ and the relation $\left(\frac{b}{2}\right)^2 + (r - r')^2 = R^2$, equation (2.27) becomes

$$\varphi = \frac{720 \cdot (c_{u3} \cdot r_3)}{\dot{V}_3} \int_{r'-R}^{r'+R} \frac{\sqrt{R^2 - (r - r')^2}}{r} \cdot dr = \frac{720\pi \cdot (c_{u3} \cdot r_3)}{\dot{V}_3} \left(r' - \sqrt{r'^2 - R^2}\right)$$

(2.28)

With $r' = r_3 + R$ a solution for the radius R of the volute cross-section can be given.

The minimum radius of the cross section is $R_{min} = b_3/2$, due to the fact, that the volute diameter must be larger than the impeller width. Therefore it is not possible to

generate a circular cross-section in the tongue region and the tongue section of the volute has to be calculated using rectangular shapes or the method suggested by Pfleiderer [29].

Another design method suggested by Pfleiderer [29] and tested by Floerkemeier [29] implies a shape coefficient μ in the following equation

$$\varphi = \frac{2\pi \cdot v_{Ti} \cdot R_i}{\mu(\varphi) \cdot \dot{V}_{opt}} \int\limits_{R_i}^{R_a} \frac{L}{R} dR \qquad (2.29)$$

The results obtained by Floerkemeier can be seen in Figure 2.19. The highest pump efficiency at design conditions is given for a volute with $\mu = \mu_{flach1}$ as proposed by Pekrun [29].

2.2.4 DESIGN WITH FRICTION

The consequence of friction on the walls is a decrease in total pressure in the flow direction. A volute calculated without considering friction would have a pressure decrease from the volute inlet to the exit and a sudden pressure rise at the tongue. In order to achieve a circumferential uniform pressure distribution at the volute inlet, design has to be corrected.

Since, it is not possible to calculate the friction losses exactly, Eckert (1961) takes into account the loss head with a friction coefficient λ :

$$dh_v = \lambda \cdot \frac{c^2}{2g} \frac{ds}{D_{hyd}} \qquad (2.30)$$

D_{hyd} is the hydraulic diameter of the cross-section and c the average velocity.

Eckert substitutes $ds = r_s \cdot d\varphi$ and integrates equation (2.30), receiving the pressure losses. By increasing the final cross-section (at the throat) accordingly, from A_1

to A_1' and subsequently the other cross-sectional areas the losses can be compensated. The average velocity changes, following the continuity equation

$$c_1 \cdot A_1 = c_1' \cdot A_1' \tag{2.31}$$

The pressure loss can be calculated with the Bernoulli equation

$$p_1 - p_v + \frac{\rho}{2}c_1^2 = p_1 + \frac{\rho}{2}c_1'^2 \tag{2.32}$$

Using equation (2.31) and (2.32) the head loss can be written as

$$h_v = \frac{c_1^2}{2g}\left[1 - \left(\frac{c_1'}{c_1}\right)^2\right] = \frac{c_1^2}{2g}\left[1 - \left(\frac{A_1}{A_1'}\right)\right] \tag{2.33}$$

From this equation the necessary cross-sectional area A_1' can be calculated, so that the pressure losses due to friction are compensated.

To compensate the pressure losses and to avoid a periodically unsteady impeller flow due to non-uniform pressure distribution in the volute Eck [17] states the same equations as given by Eckert (1961) for slightly increasing the volute cross-sectional area. He demonstrates his method by calculating the increase in area of a conic diffuser. Therefore he limits the validity of equation (2.33) and demands to consider the curvature of the volute, which causes secondary flow.

2.2.5 AREA RATIO DISTRIBUTION

In order to receive uniform inlet flow conditions the cross-sectional area centriod radius A/r must increase linearly from the volute tongue to the exit. For optimum mass flow rate the amount of mass collected by the volute has a linear increase and the circumferential pressure distribution is uniform.

Lorett (1986) gives an equation to calculate the cross-sectional area at any angle:

$$\left(\frac{A}{R}\right)_{\varphi} = \frac{V\omega\eta}{gH}\frac{\varphi}{2\pi}$$

(2.34)

R is the cross sectional radius, ω the angular velocity, η the hydraulic efficiency and H the total head (Figure 2.20).

Japikse (1996) introduced a simple volute design based on a geometric area ratio. The area ratio is defined by the equation:

$$AR = \frac{A_4}{A_3} = \frac{\pi}{4}\frac{D_4^2}{2\pi \cdot r_3 \cdot b_3}$$

(2.35)

where A_3 and A_4 are the volute inlet and exit areas. The circumferential area distribution can be seen in Figure 2.21.

2.2.6 NOVEL IDEAS

Another volute design described by Eck [17] is the axial volute (Figure 2.23). It is developed between two co-axial cylinders in the axial direction and has the advantage of arising from cylindrical surfaces. This results in an equal distribution of the circumferential velocity c_u and the lateral boundary increases only in proportion to the angle of admission. The lateral width b can be calculated for a given height h and an average value of c_u as follows:

$$b = \frac{V}{c_u \cdot h}\frac{\varphi^{\circ}}{360}$$

(2.36)

Whitfield and Roberts [45] examined two different volute/radial diffuser systems and compared them with a standard volute (Figure 2.24). One is designed to transfer part

of the diffusion process in a conic diffuser downstream of the volute, the other design allowed diffusion to take place in the collecting volute. For both systems the length of the radial vaneless diffuser was significantly reduced. Due to the fact, that the pressure rise in the shorter vaneless diffuser is lower than in a regular one. The flow velocity in the volute of the first system is larger, leading to an increase in friction losses. The reduction in pressure ratio of the stage can be seen in Figure 3.18. For the second prototype the pressure ratio is close to that of the standard volute. However, pressure ratio and efficiency fall rapidly with increasing mass flow.

2.3 VOLUTE PERFORMANCE

2.3.1 OVERALL PERFORMANCE

Volute performance is strongly influenced by the geometry of the volute casing, the flow parameters and the amount of mass-flow and the volute-impeller and volute-radial diffuser interactions. (Figure 2.26) shows the influence of the volute geometry on the efficiency of a radial compressor Eckert et al. (1961). As to be seen, asymmetrical volutes have a higher efficiency than symmetrical ones due to a stronger secondary flow in the symmetrical volute. With the meanline performance prediction program, Weber et al. (1986) describe how the losses reduce the volute performance.

2.3.2 PERFORMANCE EQUATIONS

For the evaluation of volute performance two primary parameters are calculated.

$$C_P = \frac{\overline{P}_{out} - \overline{P}_{in}}{\overline{P}_{0,in} - \overline{P}_{in}} \qquad (2.37)$$

C_P is the static pressure rise coefficient. The other parameter is ω, the loss coefficient.

$$\omega = \frac{\overline{P}_{0,\,in} - \overline{P}_{0,\,out}}{\overline{P}_{0\,in} - \overline{P}_{in}} \qquad (2.38)$$

Van den Braembussche et al. (1997) measured and predicted the static pressure rise and loss coefficients for a compressor with an external volute and rectangular cross-section. The results show higher losses for off-design mass flows, indicating that the amount of mass flow affects the volute performance. The performance of a volute can be estimated by using the following equation, combining the static pressure rise coefficient, the loss coefficient and a term to measure the outlet kinetic energy:

$$C_P + \omega + \frac{\overline{P}_o^o - \overline{P}_o}{\overline{P}_3^o - \overline{P}_3} = 1 \qquad (2.39)$$

The dependence of the loss and pressure rise coefficients on the volute outlet flow swirl can be seen in Figure 2.27.

2.3.3 OFF-DESIGN EFFECTS

Operation of the compressor at off-design points has a great effect on volute efficiency. The volute is designed to have a circumferential uniform static pressure distribution at optimum mass flow rate. However, at off-design operation the pressure distribution is distorted and the volute efficiency decreases due to diffusion, mixing and friction losses.

At smaller than optimum mass flow rate the volute acts like a diffuser resulting in a static pressure rise from volute inlet to outlet. If the mass flow rate is too large, the flow accelerates throughout the volute, which results in a pressure decrease between the volute

tongue and the conic diffuser. The effects of off-design operation on the compressor performance are a decrease in volute efficiency due to higher losses and radial forces on the impeller due to the non-uniform circumferential pressure distribution.

2.3.4 VOLUTE-IMPELLER INTERACTION

A circumferential uniform pressure distribution caused by a correctly designed volute at optimum mass flow rate results in a uniform blade load of the impeller. Only the volute tongue causes pressure and velocity distribution distortion, therefore, influences the impeller performance. The large pressure changes in the tongue region cause noise and vibration as well.

At off-design conditions the large velocity and pressure distortion cause variations of velocity and pressure along the impeller periphery. The flow in the impeller channels change periodically, causing radial thrust on the impeller shaft. The cyclic variation of the flow in the impeller channels results in additional energy dissipation. The effect is strong for short vaneless diffusers and almost negligible with vaned diffusers, Van den Braembussche (1998).

As described by Van den Braembussche (1998), the volute influences the impeller by a change in operation range and shift surge and choking limits. Smaller volutes give higher shut off pressure ratios and steeper performance curves than standard ones. The influence of two different volutes on the same impeller is shown in Figure 2.30. As seen in the figures larger volutes result in a larger operation range but have an unsteady flow at higher-pressure ratios. The flow in the smaller volute is more stable but the volute has a smaller range due to choking at low-pressure ratios.

Lorett et al. (1986) developed a computational method to express the volute-impeller interactions. They presented numerous equations to predict the flow behavior at off-design conditions. At very low-mass flow complete flow reversal in the impeller channels can occur, introducing flow prerotation at the impeller inlet. Figure 2.31 shows the distortion of the velocity field in the impeller at low mass flow and the reversal of the velocity.

Bowerman et al. [28] measured the influence of the volute performance on the impeller. They used three volutes with a constant axial width and the variation of the cross-sectional area defined by the logarithmic shape of the outer wall. Using the conservation of angular momentum equation and the continuity equation the volute is defined by

$$R = R_1 \cdot e^{\frac{\phi}{\psi}\theta} \qquad (2.40)$$

where R and θ are the radial and angular coordinates of the volute outer wall, ϕ and ψ are the flow- and head coefficients. The cross sectional area distributions of the three volutes result from the choice of ϕ equal to 75, 100 and 120 percent of the impeller design flow coefficient. Figure 2.32 shows the overall performance of the three-volute/impeller combinations.

For low flow rates the volute with the smallest cross sectional area has a higher efficiency than the other volutes, but for high flow rates the decrease in efficiency is larger than for the other volutes. The contrary situation can be found for the volute with the largest cross sectional area. This shows that the shape of the volute outer wall determines the volute-impeller matching mass flow.

2.3.5 VOLUTE-RADIAL DIFFUSER INTERACTION

Pressure and velocity distributions in the volute affect the radial diffuser efficiency as they cause velocity distortions in the radial diffuser. Figure 2.33 by Mueller [29] shows the velocity distribution in the radial diffuser caused by the volute. The volute tongue causes a wake, which propagates itself in the radial diffuser and contributes to the radial diffuser losses as measured.

The secondary flow in the volute greatly influences the radial diffuser flow leading to a non-uniform pressure distribution in the radial diffuser cross-section. Mueller [29] noticed that the secondary vortex flow transports boundary layer material in the core flow of the radial diffuser causing mixing and diffusion losses. With an asymmetrical design of the volute, it should be possible to reduce the radial diffuser losses.

2.3.6 PARAMETERS AND MECHANISMS INFLUENCING PERFORMANCE

A high inflow velocity c affects the volute performance negatively, as it increases the volute wall friction losses, which are function of the volute Reynolds-number. Following the pipe friction loss-model, the pressure losses due to wall friction are also a function of the volute surface roughness.

Varghese (1978), describes in his work the influence of the volute surface roughness on compressor performance. As expected the hydraulic losses increase with increasing surface roughness, as shown in Figure 2.34. The experimental results shown in this figure are in agreement with the empirical equation given by Varghese for the volute efficiency:

$$\sqrt{e_0} = 2.1605 \cdot R^{-0.0738} - 0.029 \log\left(\frac{\Delta}{d}\right) \tag{2.41}$$

Varghese observed that with increase in surface roughness, the best efficiency regime shifts to smaller discharges. The hydraulic losses in the volute however are not mainly influenced by the surface roughness, but by mixing losses, which are dependent on the Reynolds number (Figure 2.35). The results show the mixing process plays a more predominant role in deciding the volute losses than the surface roughness. The losses can be described by the following equation:

$$K = \frac{2g(H_I - H)}{v_d^2} \tag{2.42}$$

where $(H_I - H)$ is the difference between the virtual and the total head developed by the pump. K can be expressed as

$$K = f\left(\text{Re}, \frac{d}{\Delta}, R\right) \tag{2.43}$$

and can be calculated empirically.

Iversen et al. (1960) assumed that the mixing of the fluid exiting the impeller with the fluid already in the volute influences the volute pressure distribution. In order to describe the relation between the mixing and radial forces on the impeller as well as head losses, Iversen developed a program. Additionally he performed experiments with a centrifugal compressor to compare his findings with the program. Figure 2.36 shows the results and comparison.

The influence of the volute inflow angle α, is described by Van den Braembussche (1998) and Huebl [29]. If the inflow angle is too large with respect to tangent, the flow has a large radial and a small tangential velocity. This occurs, if the volute operates at larger than optimum mass flow rate. Due to the large radial velocity the formation of secondary flow vortices increases having a negative effect on volute

efficiency. For a small inflow angle the radial velocity is small compared to the tangential velocity, resulting in a small vortex formation.

Cohen et al. (1987), describe the effect of high Mach numbers on volute performance. High Mach numbers at the volute inlet are to be avoided, as they cause shock losses. They also imply high air speeds and large pressure gradients leading to a circumferential variation of static pressure. To reduce the relative velocity at the impeller inlet and hence the Mach number Cohen suggests to use inlet guide vanes.

2.3.7 VOLUTE LOSSES

2.3.7.1 GEOMETRICAL AND AERODYNAMIC EFFECTS

The volute itself has a direct influence on the performance of the compressor because of the non–isentropic deceleration of the fluid inside the volute, Van den Braembussche (1998). The overall performance of the volute is influenced by the volute cross-sectional shape and its radial position, the circumferential variation of the cross-sectional area, the tongue geometry and the shape of the conic diffuser, Elholm et al. (1992).

- Aerodynamic effects influencing performance

Because of the curvature of the volute, boundary layers of the volute flow are decelerated and as they have the pressure distribution of the core flow, they produce a secondary flow on both sidewalls of the volute. The boundary layers follow the pressure gradient from the surface to the core of the volute, mix with the core flow and are thrown

back towards the volute surface. A twin vortex is shaped which produces pressure losses (Figure 2.37). The twin vortex can be reduced to a simple vortex designing the volute asymmetrical, Eck [17].

- Influence of the cross-sectional shape and volute size

The cross-section shape and its radial location have an important influence on the volute losses. Circular cross-sections have a smaller wetted surface and therefore show smaller friction losses, Van den Braembussche (1998). Although it is quite imaginable, the swirling flow in rectangular cross sections does not cause higher losses than in elliptical or circular ones, as the flow approaches the corners tangentially and does not undergo a 90° - turning.

Volutes with elliptic cross-sections show higher diffusion and mixing losses than circular ones, because of the periodic increase and decrease of the swirl velocity V_S following the conservation of angular momentum equation. Asymmetrical volutes have a higher efficiency than symmetrical volutes, because of the formation of a single vortex in the asymmetrical one instead of the double vortex in the symmetrical volute.

The size of the volute also has major effects on the performance of the compressor-volute system. Larger volutes give lower shut off pressure ratios and flatter performance curves, while smaller volutes result in higher shut off pressure and steeper performance curves than standard ones, Van den Braembussche (1998). There is only one amount of mass flow rate for which the volute has a circumferentially uniform pressure distribution and therefore the least losses. If the mass flow rate is smaller than at the optimum, the flow is decelerated inside the volute and a static pressure rise from the volute inlet to the

outlet occurs, resulting in diffusion losses. Small radial velocity causes a rise of swirling motion, which is dissipated by internal shear and wall friction.

For larger than optimum mass flow rate the volute is too small, thus the flow is accelerated inside the volute resulting in a pressure decrease from the volute inlet to the outlet. This results in a circumferential pressure distortion at the radial diffuser and impeller exit and extra losses due to a partial destruction of pressure rise, which took place in the radial diffuser, Van den Braembussche (1998). Internal volutes show a lower efficiency than external ones, due to an increase in through flow velocity because of a decreasing average radius.

The acceleration of the fluid destroys the static pressure rise achieved upstream in the vaneless diffuser. Therefore the static pressure decreases from the vaneless diffuser exit to the volute exit. Another reason for the low efficiency of internal volutes is an accumulation of low energy fluid at the inner wall and the existence of an anti clockwise vortex in the hub inner-wall corner, Van den Braembussche (1998).

- Influence of the tongue geometry

The tongue is a major contributor to the casing losses, Chen (1986). Especially in turbine volutes the tongue losses are not to be neglected, as the flow around the tongue generates a wake, which leads to additional diffusion and mixing losses. In compressor volutes impact losses occur at the tongue at off-design operation, as the flow angle off the impeller does not match the volute-opening angle [29]. An increasing opening angle at a given mass flow leads to flatter loss curves, with the point of minimum losses moving to greater flow coefficients.

The volute performance is also influenced by the necessary clearance between impeller and volute tongue. Parts of the flow will stream through this gap and produce losses, as they have to rotate around the impeller again. The clearance can be modified either by changing the tongue angle or the length of the tongue. To change the tongue angle, the volute can be designed with a pivoting tongue (Figure 2.13). A larger clearance leads to a decrease in compressor efficiency and a more narrow operating range. The tongue length affects the overall efficiency with a shorter tongue causing higher efficiency than a longer, Ayder (1993). Pfleiderer and Petermann [29] recommend that the tongue should be of a certain thickness and well rounded to minimize a decrease in efficiency at off-design operation.

- Influence of the exit diffuser

A major contributor to the volute losses is the secondary flow in the exit conic diffuser. The intense vorticity generates strong local shear resulting in turbulent and viscous dissipation. From their numerical calculations Li et al. [27] developed, that the swirling motion of the fluid particles in the curved conic diffuser is more intense than that in the straight diffuser, therefore leading to higher losses in the curved diffuser. They conclude, that the losses in the diffuser can be reduced by improved design, such as a straight diffuser. Pfleiderer [29] claims the opposite. He says that the curved diffuser can have a higher efficiency than the straight diffuser.

2.3.7.2 LOSS COEFFICIENTS

There are several models describing the losses in the compressor volute. One of them is the model by Weber et al. (1986), which is further described by Van den

Braembussche et al. (1992, 1998). It was generated for use in meanline performance prediction programs (MLPPP). The model describes the four main sources of losses:

1. Meridional velocity dump loss

It is assumed that the head associated with the meridional velocity at the volute entrance is lost. The reason for this, intuitively given by Weber et al. (1986), is that the meridional velocity entering the volute becomes a spiraling velocity component in the volute does not contribute to the transport of the fluid through the volute. The amount of loss is expressed by the equation

$$\Delta p_{MVDL}^0 = \frac{1}{2} \rho \cdot v_{R3}^2 \qquad (2.44)$$

2. Skin friction loss

The friction loss is a function of the surface roughness of the wall, the volute's hydraulic diameter D_{hyd}, the average path length of the fluid particles L within the volute and the volume flow entering the volute, represented by the through flow velocity v_T.

$$\Delta p_T^0 = \omega_F \frac{L}{D_{hyd}} \frac{1}{2} \rho \cdot v_T^2 \qquad (2.45)$$

The friction coefficient ω_F is a function of the Reynolds number and the relative surface roughness and is obtained by making use of the standard friction charts for pipes.

3. Exit cone loss

Having been calculated during the past as a simple, sudden expansion loss, the exit cone loss is now calculated using the standard gradual expansion model from pipe flow analysis, Van den Braembussche (1998).

$$\Delta p_{EC}^0 = \omega_E \cdot C \cdot \rho \frac{(v_4 - v_5)^2}{2} \qquad (2.46)$$

With v_4 as the velocity at the radial diffuser entrance and v_5 as the exit velocity.

Δp_{EC}^0 depends on the total opening angle of the cone and varies from 0.15 for an opening angle of $10°$ to a value of the order of 1 for an opening angle $60°$, Van den Braembussche (1998). Weber et al. (1986), propose a constant value of 0.15, since the opening angle of the volute exit cone should not exceed $10°$.

4. Tangential velocity dump loss

Two assumptions are made, in order to calculate the tangential velocity dump loss:

If the tangential velocity accelerates from volute inlet to volute outlet $(v_{T3} < v_{T4})$, it is assumed that no tangential velocity dump loss occurs.

If the tangential velocity decreases from the volute inlet to the volute outlet $(v_{T3} > v_{T4})$, then the flow diffuses and the appearing total pressure loss is equivalent to the total pressure loss in a sudden expansion mixing process.

$$\Delta p_{TVDL}^0 = \omega_T \rho \frac{(v_{T3} - v_{T4})^2}{2} \qquad (2.47)$$

where $\omega_T = 1$.

Van den Braembussche (1998), points out that the modeling of the tangential velocity dump losses without taking into account the variation of the central radius of the volute channel causes an incorrect prediction of the losses especially for internal volutes. Therefore, the modeling of the tangential velocity dump loss has been modified by introducing an intermediate station in the volute channel at the point where 50% of the total mass flow is collected by the volute. In this new model the loss consists of two

components: If the tangential velocity at the volute inlet v_{T3} is larger than the tangential velocity at the 50% collection point v_{T3-f} the flow is accelerating in the first part of the volute and the first component of the loss is calculated by

$$\Delta p^0_{TVDL-f} = \omega_T \rho \frac{\left(v_{T3} - v_{T3-f}\right)^2}{2}$$

(2.48)

If v_{T3} is smaller than v_{T3-f} the first component states

$$\Delta p^0_{TVDL-f} = \rho \frac{\left(v_{T3} - v_{T3-f}\right)^2}{2}$$

(2.49)

In case of v_{T3} is larger than v_{T4} the flow is accelerating and the second component of the tangential velocity dump loss is given by

$$\Delta p^0_{TVDL-4} = \omega_T \rho \frac{\left(v_{T3} - v_{T4}\right)^2}{2}$$

(2.50)

Otherwise,

$$\Delta p^0_{TVDL-4} = \rho \frac{\left(v_{T3} - v_{T4}\right)^2}{2}$$

(2.51)

The total tangential velocity dump loss is the given by adding the two components:

$$\Delta p^0_{TVDL} = \Delta p^0_{TVDL-f} + \Delta p^0_{TVDL-4}$$

(2.52)

Another model describing the losses in compressor volutes is the one by Decker [29]. From his measurements of the flow in a compressor with different impellers and volutes, he specified three different types of losses:

1. Wall friction loss

Similar to Weber et al. (1986), Decker describes the wall friction loss in analogy to the pipe friction loss model.

$$\psi_{v,rb} = \frac{\zeta_{rb,SP} \cdot c_{SP}^2}{u_2^2} \qquad (2.53)$$

with c_{SP} as a characteristic velocity of the volute, here the average velocity in the 360 degrees cross section.

Taking into account the continuity equation the wall friction losses can be written as

$$\psi_{v,rb} = \zeta_{rb,SP} \left(\frac{A_2}{A_{SP}} \right) \varphi_r^2 \qquad (2.54)$$

2. Decker assumes that the flow performs according to the angular momentum equation. This implies, that the volute can only have the correct size for one flow coefficient $\varphi_{r,opt,SP}$, which represents the proper amount of flow.

The volute is either too large or too small for all other amounts of mass flow, so that the flow angle off the impeller is not according to the volute tongue angle. This results in impact losses, which can be written as

$$\psi_{v,st,SP} = \zeta_{st,SP} \left(\frac{A_2}{A_{SP}} \right)^2 \left(\varphi_r - \varphi_{r,opt,SP} \right) \qquad (2.55)$$

with $\varphi_{r,opt,SP}$ as the optimum mass flow coefficient.

3. The combination of a rotating impeller and the non-rotating volute implies a certain link between impeller and volute tongue.

This distance implies that a small part of the fluid flows through the gap between impeller and tongue and is forced to revolve around the impeller again, leading to a so-called kink-loss $\psi_{vs,SP}$, which is a linear dependence of the theoretical pressure coefficient ψ_{th}.

$$\psi_{vs,SP} = K_s \psi_{th} \qquad (2.56)$$

From his experimental and computed results, Decker assumes a linear dependence of the cross-section rate A_{SP}/A_2 for the friction- and impact coefficient:

$$\zeta_{rb,SP} = k_{rb} \frac{A_{SP}}{A_2} \ ; \ \zeta_{st,SP} = k_{st} \frac{A_{SP}}{A_2} \qquad (2.57)$$

For the volutes used by Decker the coefficients k_s, k_{rb} and k_{st} are constants.

The total volute losses are the sum of the three loss types:

$$\psi_{v,SP} = \psi_{v,rb,SP} + \psi_{s,st,SP} + \psi_{vs,SP} \qquad (2.58)$$

Huebl [28] introduced another model. He describes the losses in the volute consisting of two parts, the wall friction head loss and the interior friction head loss.

1. The wall friction head loss is the difference between the squared in-flow velocity c_0 and the squared velocity on the volute surface c_s:

$$h_{vw} = \frac{c_0^2 - c_s^2}{2} \qquad (2.59)$$

2. The tangential velocity in the volute is reduced by wall friction.

3. The difference between the friction induced reduction of the tangential velocity head and the original tangential velocity head is called interior friction head loss.

$$h_{vi} = \frac{c_s^2 - c_t^2}{2} \qquad (2.60)$$

Summation of the two loss types results in the local head loss for any location in the volute casing.

$$h_v = h_{vw} + h_{vi} \qquad (2.61)$$

The loss model given by Eck [17] contains of radial diffuser losses and friction losses. The radial diffuser losses developed due to the retardation of the flow in the radial diffuser. With the entry velocity into the volute is c_3 and the discharge velocity c_4, the losses can be written as

$$\Delta p''_{loss} = (0.1 - 0.2)(\rho/2)[c_3^2 - c_4^2]$$ (2.62)

In case that the casing width B is greater than the impeller width b an additional shock loss occurs, as the meridian velocity c_{2m} will change to c_{3m} following the continuity equation. The resulting loss can be described as follows:

$$\Delta p''_{loss} = (\rho/2)(c_{2m}^2 - c_{2m}^2) = (\rho/2)c_{2m}^2\left(1 - \left(\frac{b}{B}\right)^2\right)$$ (2.63)

Eck describes the friction losses as throughout the dynamic pressure of the meridian velocity in the radial diffuser.

$$\Delta p_{loss,total} = (\rho/2) \cdot c_{2m}^2$$ (2.64)

Relating the total loss coefficient to the dynamic pressure of the entry velocity, the friction losses are

$$\Delta p_{loss,total} = \zeta \frac{\rho}{2} c_2^2$$ (2.65)

and for the loss coefficient one can obtain

$$\zeta = \frac{\Delta p_{loss,total}}{(\rho/2) \cdot c_2^2} = \left(\frac{c_{2m}}{c_2}\right)^2 = \sin^2 \alpha_2$$ (2.66)

Lorett et al. (1986), has a simple loss model consisting of mixing losses and pressure drops caused by wall friction. He describes the energy losses of the volute as the

difference between the flow energy at the impeller exit and the energy at the volute outlet, without distinguishing single loss types.

The energy contributed by the impeller at each section of the volute, is given by Lorett as:

$$\Delta E_i = \Delta Q_i \left(H_{Si} + \frac{C_{2i}^2}{2g} \right)$$

(2.67)

The energy at the volute exit is

$$\Delta E_N = Q_{TOT} \left(H_{SN} + \frac{C_N^2}{2g} \right)$$

(2.68)

The total volute loss can now be obtained by subtracting equation (2.67) from equation (2.66):

$$L = \Sigma \Delta E_i - E_N$$

(2.69)

Eckert's loss model only takes into account the wall friction losses and gives equations to compensate them for volute design. He describes the head loss dh_v in relation to the friction coefficient λ :

$$dh_v = \lambda \frac{c^2}{2g} \frac{ds}{D_{hyd}}$$

(2.70)

Substituting ds by $ds = r_s \cdot d\varphi$ and integrating equation (2.70) the pressure loss for a volute section can be written as

$$h_v = \frac{\lambda}{2g} \int_{\varphi_0}^{\varphi_1} \frac{r_s \cdot c^2}{D_{hyd}} d\varphi$$

(2.71)

Eckert uses the circumferential velocity at the centriod c as an approximation for the cross-sectional velocity. D_{hyd} is the hydraulic diameter of the cross-section.

Ayder et al. (1993) described another three-dimensional model, which numerically calculates the volute losses by adding second order dissipation and wall shear forces to an Euler solver. They justify their method with the fact that the simplified one and two-dimensional prediction methods found in the literature are of limited interest, since the volute flow is highly three-dimensional. The flow in volutes is more affected by the losses in the core flow than by the losses at the wall. However because it is quite difficult to determine the core losses numerically and shear forces are calculated only on the walls and the internal friction is approximated by a viscous term. The wall shear stresses are given by

$$\tau_{wall} = c_f \frac{1}{2} \rho \cdot v^2 \qquad (2.72)$$

and its components are added to the loss vector, taking into account the energy dissipation due to wall friction. The viscous energy dissipation is achieved by the second order dissipation. The equations are not given here due to their complexity, they can be found in Ayder et al. (1993). They conclude that their model using an Euler solver with a loss model can predict the volute flow and losses accurately and causes a smaller computational effort than a solution of the full Navier Stokes equations.
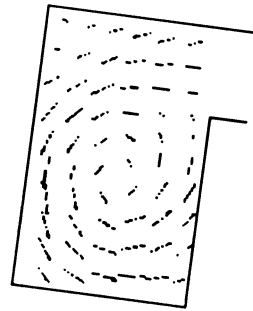
FIGURES

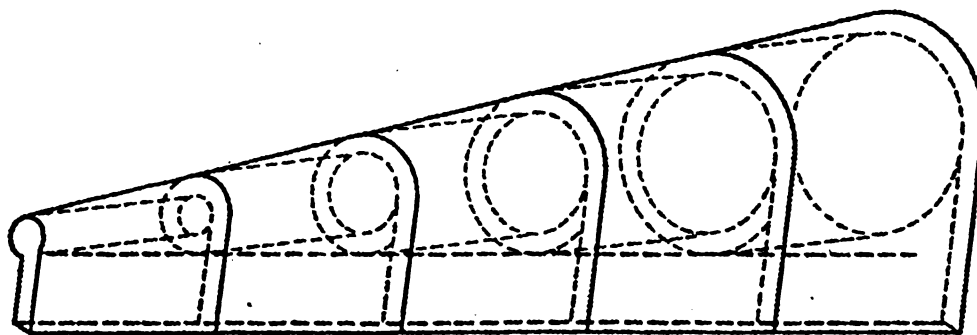Figure 2.1 Swirling Flow in a Volute

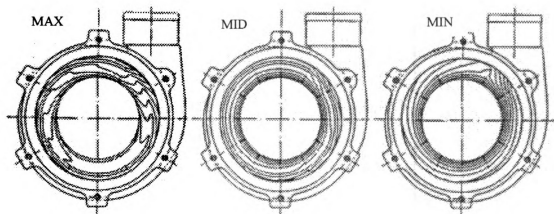
Figure 2.2: Superposition of Vortex Tubes in a Volute

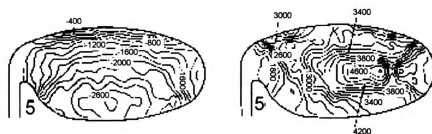Figure 2.3: Static Pressure Distortion for High, Optimum and Low Mass Flow

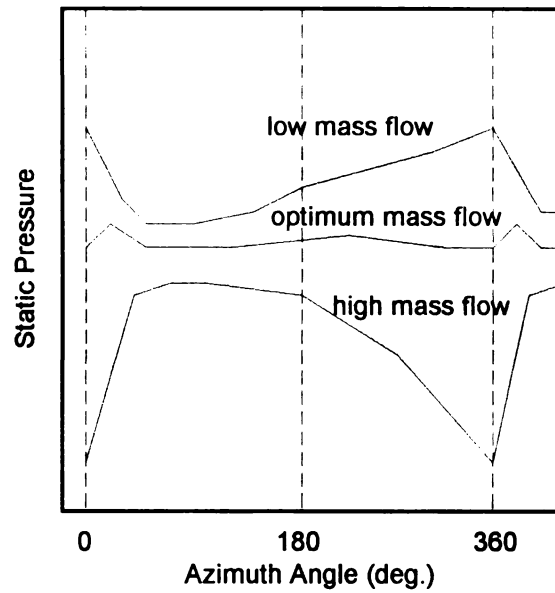Figure 2.4: Static and Total Pressure Variation (Pascal) over the Volute Cross

Figure 2.5: Circumferential Static Pressure Distribution on the Volute Wall
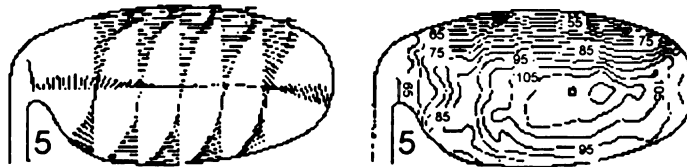

Figure 2.6: Swirl- and through flow Velocity Variation
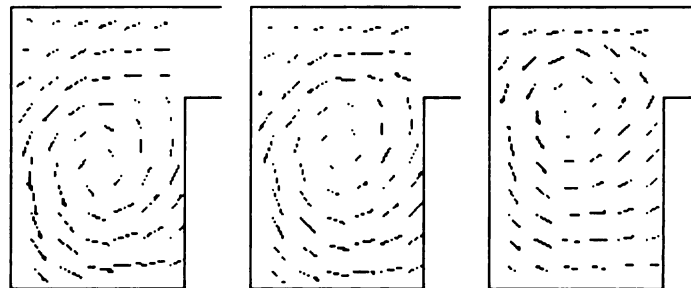(m/s) over the Volute Cross Section

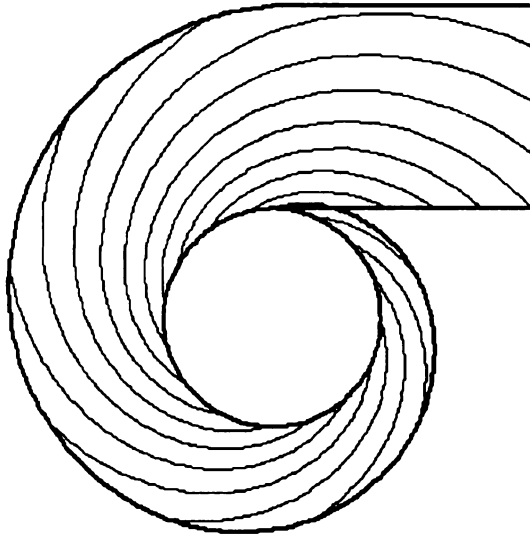Figure 2.7: Position of the Swirl Center for High, Medium and Low Mass Flow

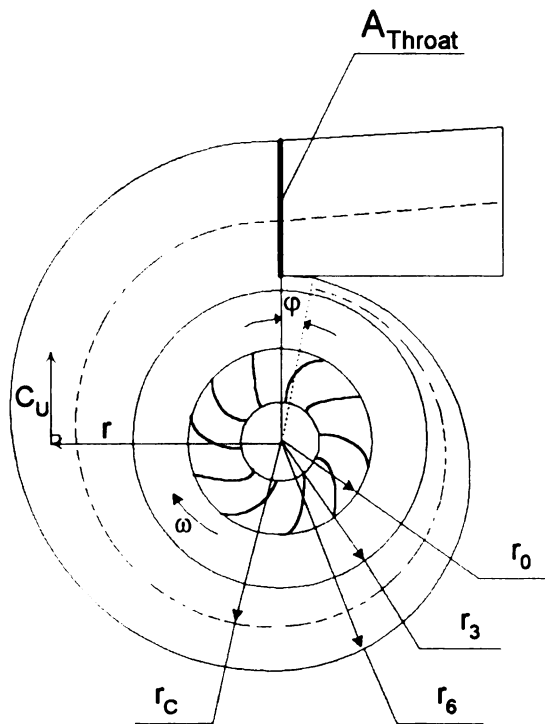Figure 2.8: Formation of the Volute Casing from the Streamline of a Vortex Source

Figure 2.9: Volute Casing with Logarithmic Shape

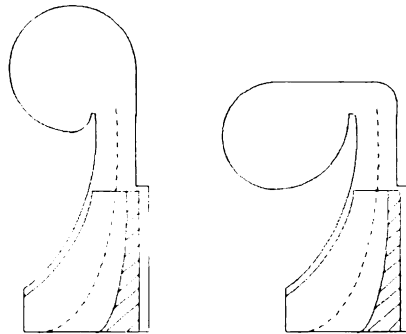Figure 2.10: External and Internal Volutes
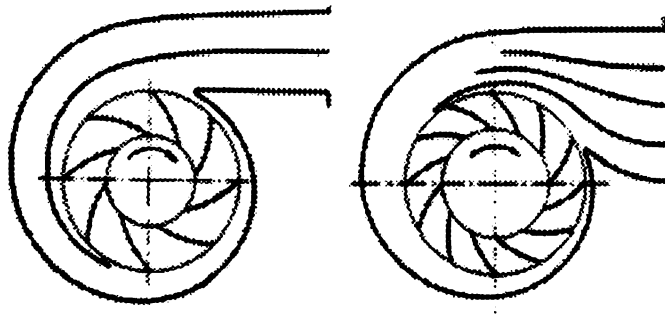
Figure 2.11: Volutes with more Subdivisions
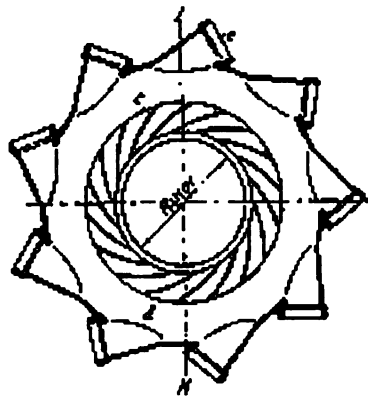
Figure 2.12: Volute with Multiple Discharge Points
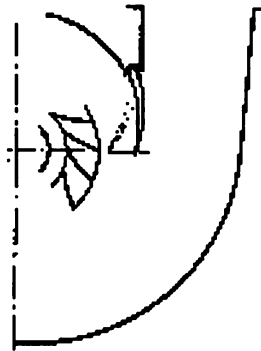
Figure 2.13: Volute with an Adjustable Tongue
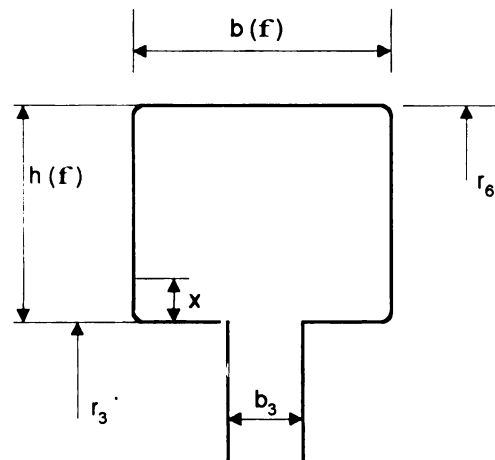
Figure 2.14: Volute with Rectangular Cross-Section
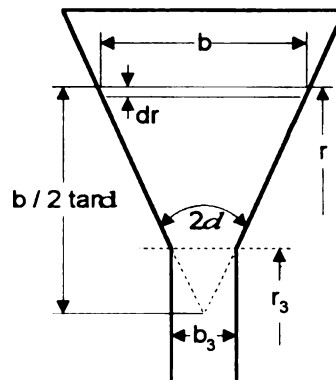
Figure 2.15: External Volute with Tapering Side Walls
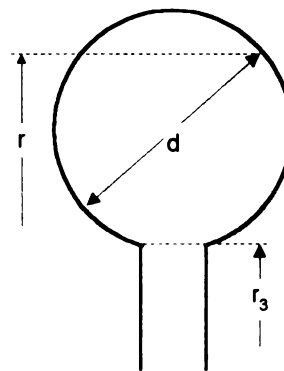
Figure 2.16: Volute with Circular Cross Section
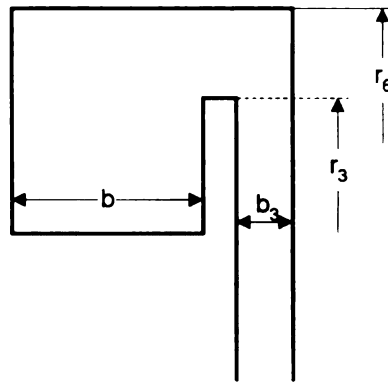
Figure 2.17: Internal Volute
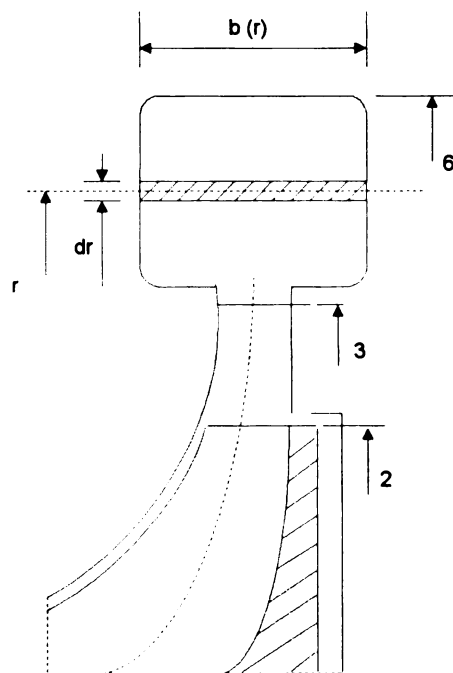
Figure 2.18: Basic Volute Geometry

69
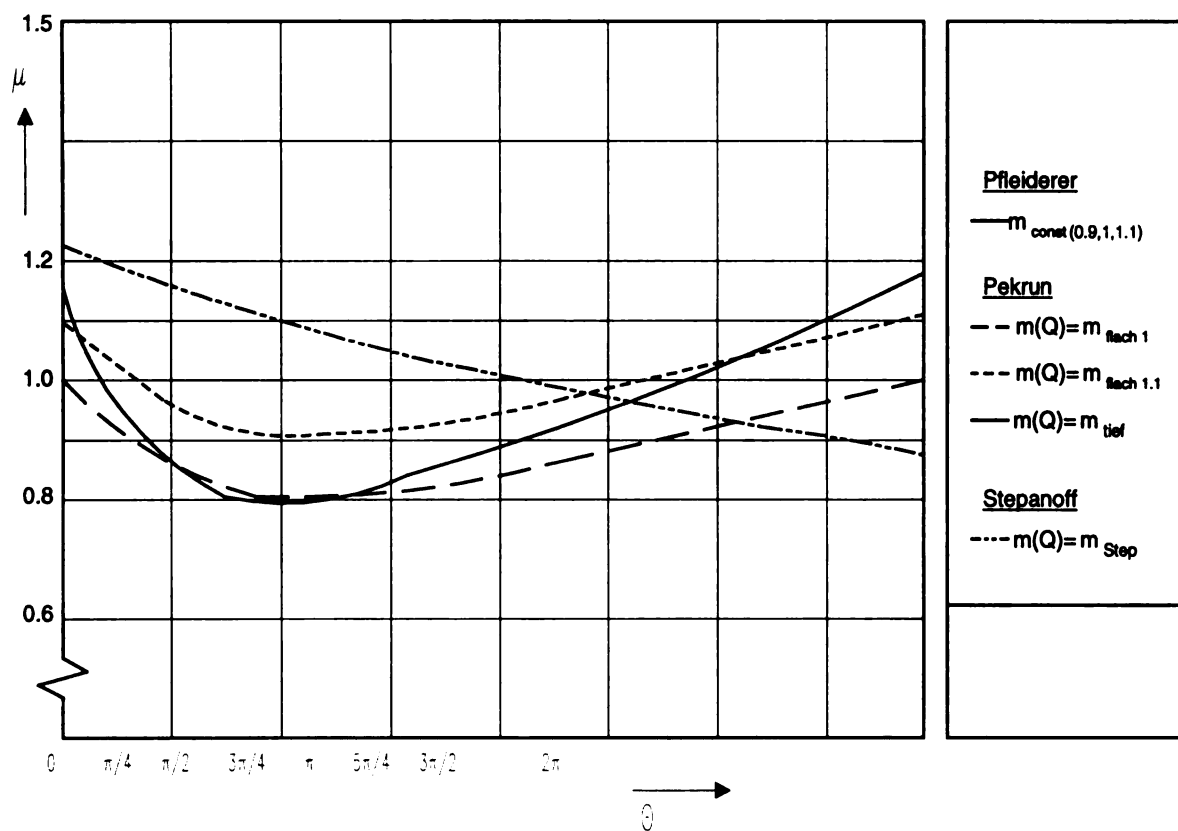
Figure 2.19: Distributions of Shape Coefficient of Volute Outer Wall
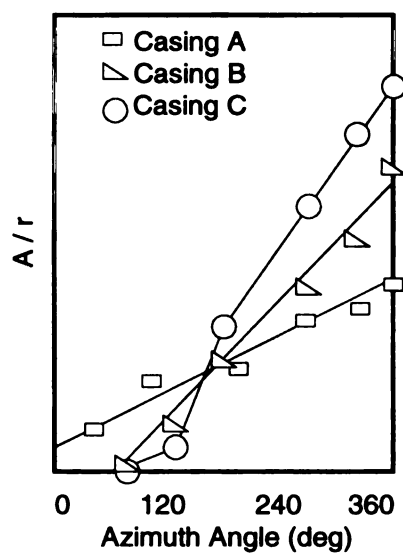
Figure 2.20: Distribution of area by centriod radius over azimuth angle

70
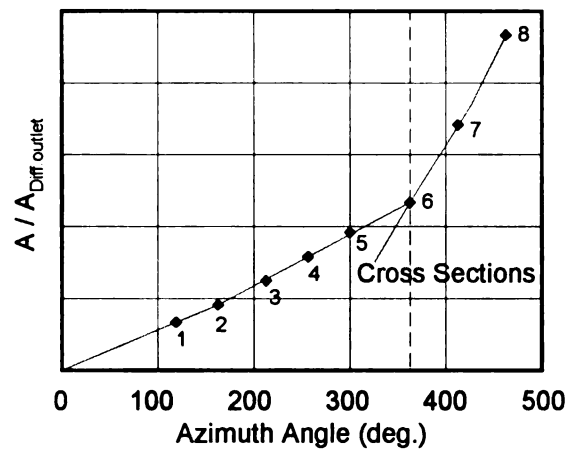
Figure 2.21: Circumferential Variation of Cross Sectional Area
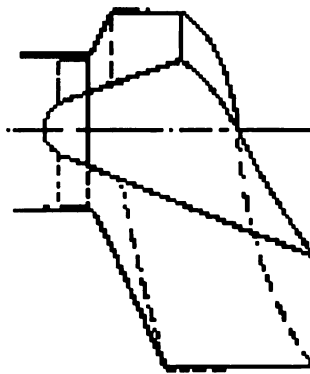
Figure 2.22: Helix Volute
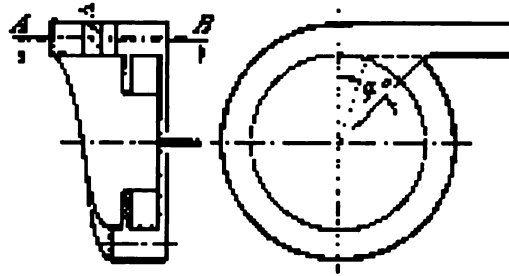
Figure 2.23: Axial Volute
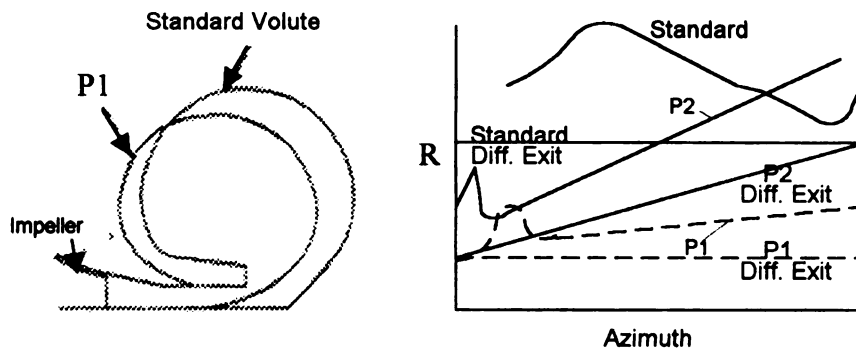
Figure 2.24: Comparison of Standard and Modified Volutes
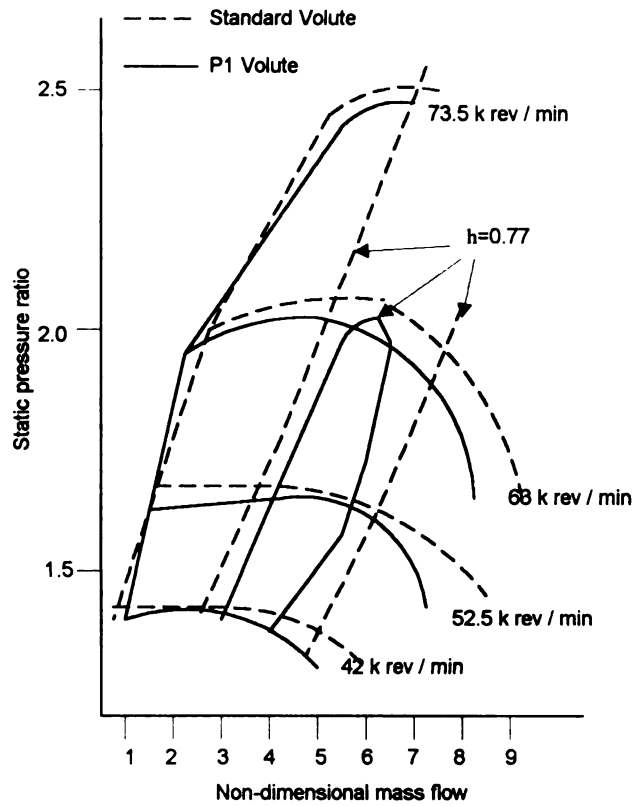
Figure 2.25: Comparative Performance Maps of Standard and Modified Volute
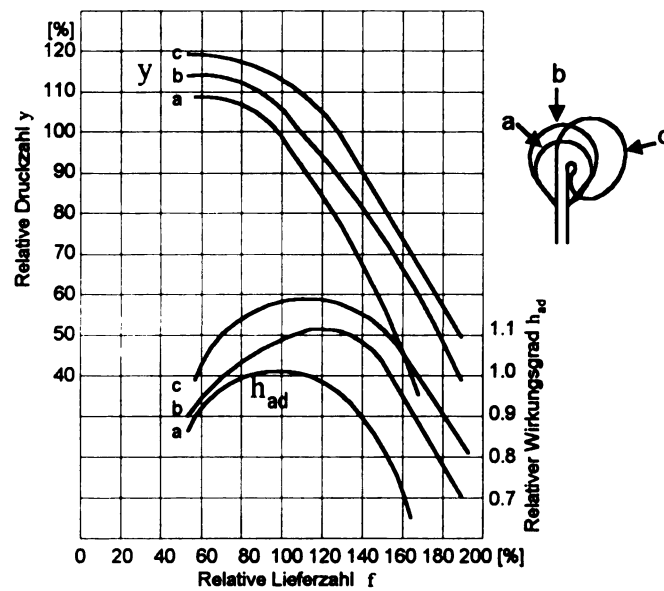
Figure 2.26: Influence of the Volute Casing on Compressor
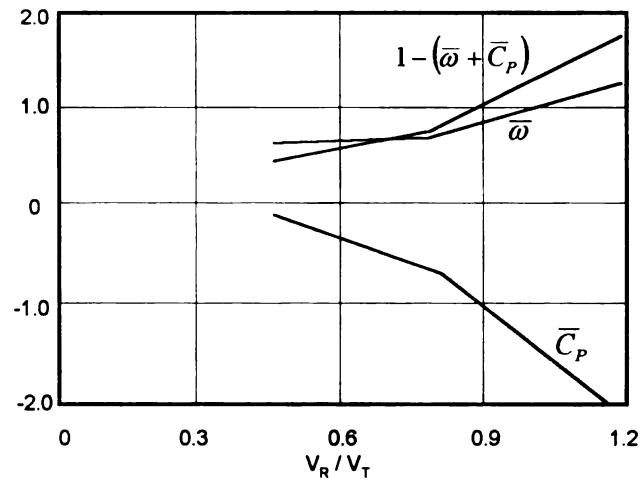
Figure 2.27: Variation of the Volute Loss Coefficient and the Pressure Rise
Coefficient as a Function of the Diffuser Outlet Swirl
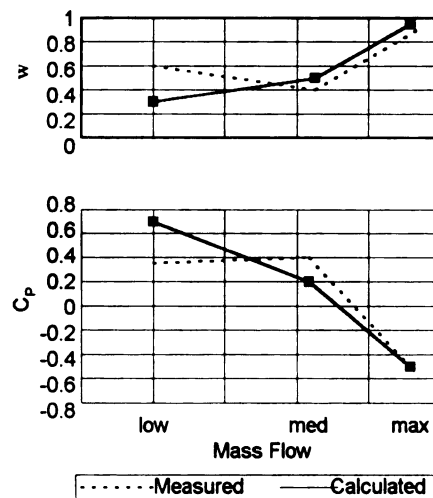
Figure 2.28: Loss and Static Pressure Rise Coefficient
for the External Volute
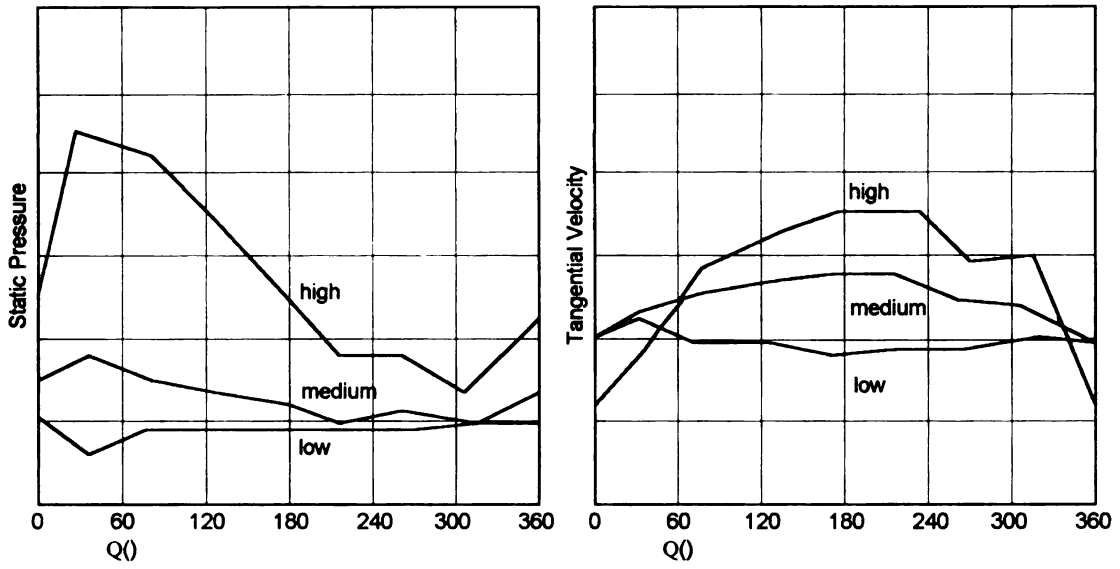
Figure 2.29: Circumferential variation of static pressure and tangential velocity at the volute inlet
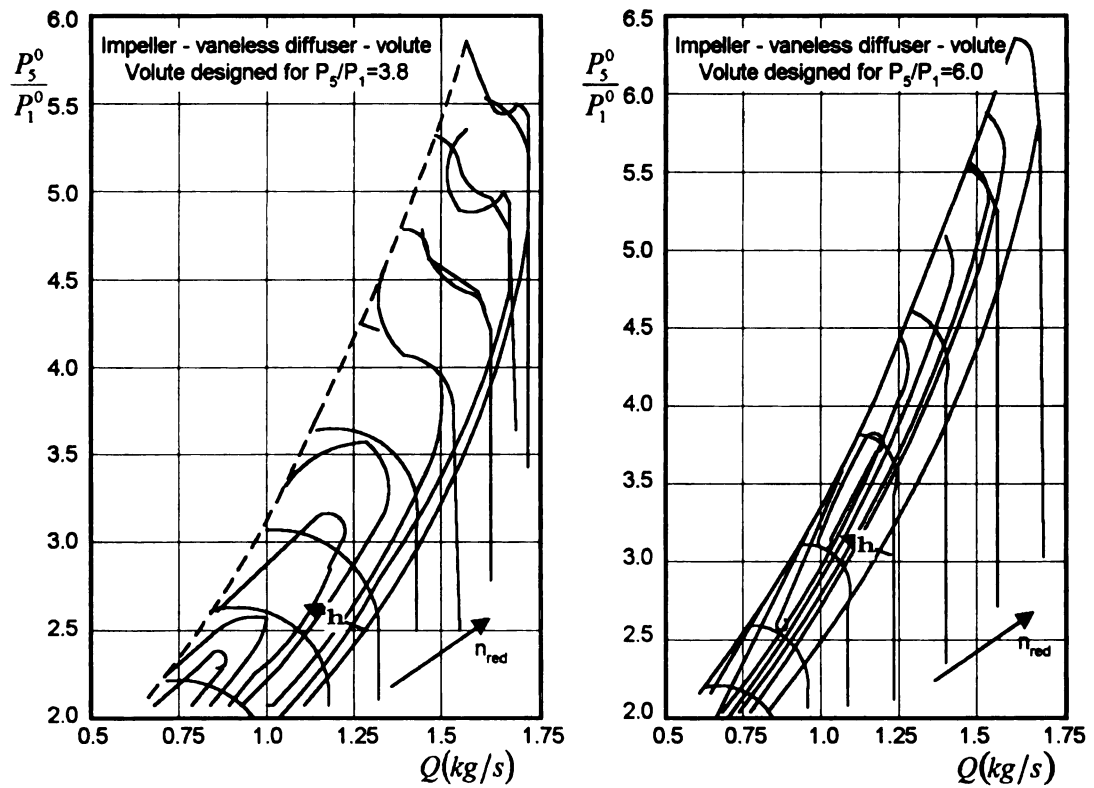
Figure 2.30: Influence of the Volute Size on Radial Compressor Performance
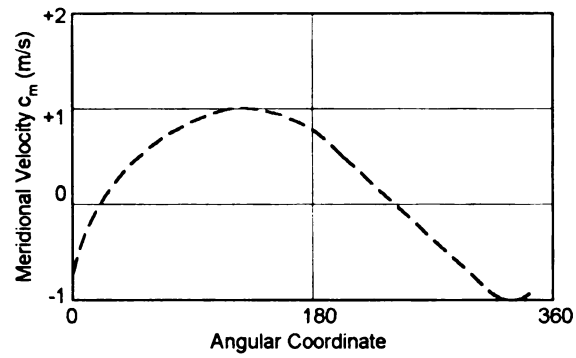
Figure 2.31: Reversal of Meridional Velocity at the Impeller for Low Mass Flow
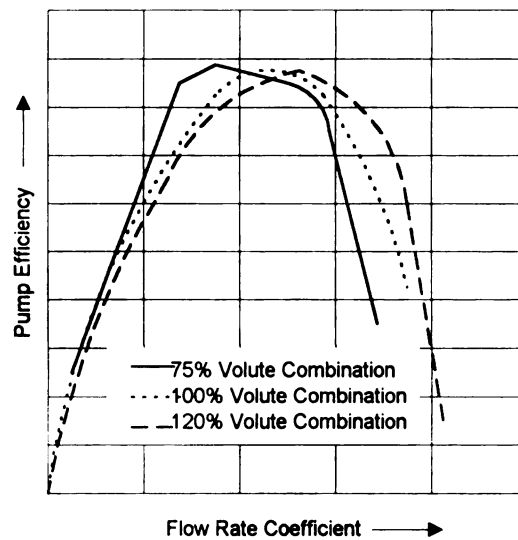
Figure 2.32: Pump Efficiency for three Impeller – Volute Combinations
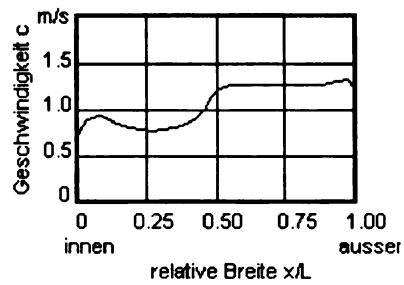
Figure 2.33: Velocity Distribution in a Volute
Conical Diffuser
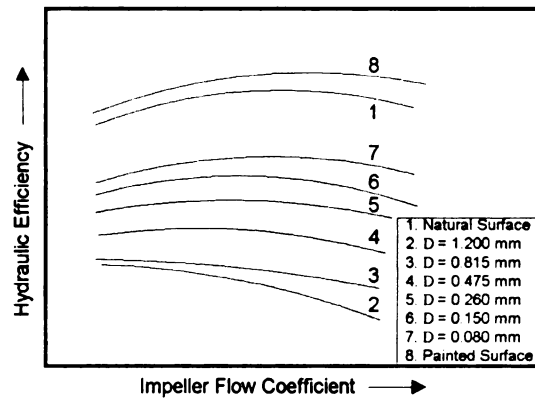
Figure 2.34: Hydraulic Efficiency for Different Volute
Surface Roughness

Legend:
1. Natural Surface
2. D=1.200 mm
3. D=0.815 mm
4. D=0.475 mm
5. D=0.260 mm
6. D=0.150 mm
7. D=0.080 mm
8. Painted Surface
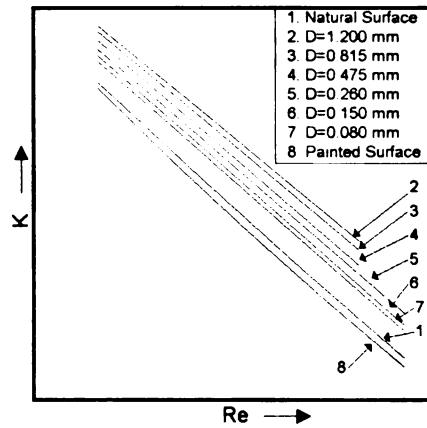
Figure 2.35: Hydraulic Losses K for Different Surface Roughness
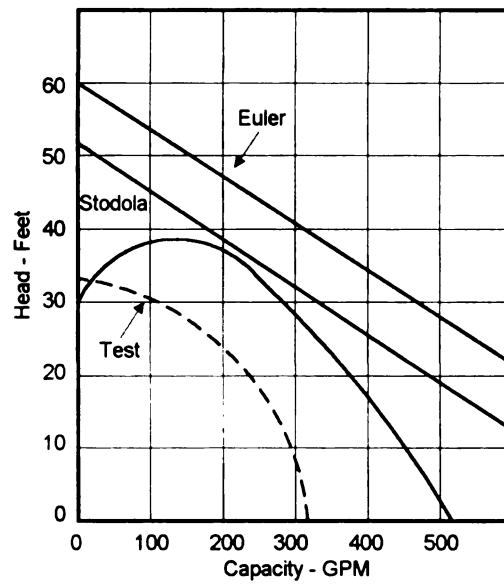
Figure 2.36: Pump Head-Capacity Relationship
Effect of Volute Mixing Losses

78
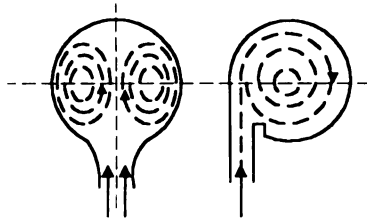
Figure 2.37: Asymmetrical and Symmetrical Volutes
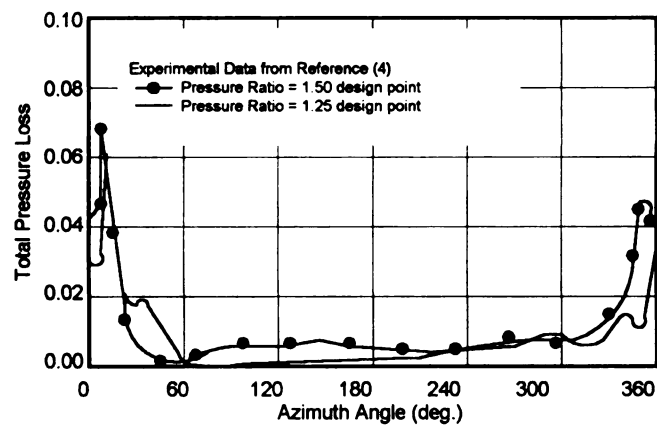
Figure 2.38: Casing Total Pressure Loss at Rotor Inlet

CHAPTER 3

EXPERIMENTAL APPARATUS

In this chapter, the details of the experimental facility setup and modifications are discussed. The initial measurement strategy and further changes were described. Note that because of the confidentiality of the compressor geometry, the author was not permitted to provide the details of the compressor geometry and they are not presented in this dissertation.

3.1 MODIFICATION OF THE TRANE COMPRESSOR

Trane Company donated a two-stage centrifugal compressor to Michigan State University (MSU) for this study. The unit operates with refrigerant gas R123 and is driven by hermetic motor (Figure 3.1). An electrical motor is installed on the casing and shares single shaft with the compressor (Figure 3.2).

In order to prevent working with refrigerant and high-pressure ratios in laboratory environment, air was selected as working fluid and modify the unit to a single stage compressor. The original modification plan suggested by Trane Company included the following (Figure 3.3):

1. Disassemble the compressor completely

2. Design and manufacture a new shaft to accommodate an external driving motor

3. Replace the 1st stage impeller by a spacer on the shaft

4. Provide a straight inlet to the second stage by placing a pipe inside the casing and block the 1st stage return channel

5. Reassemble the unit completely

After studying the design carefully and evaluating the resources, several modifications were performed as following:

1. The compressor was disassembled completely following the disassembly manual

2. The new shaft was designed and manufactured by a company outside the state

3. A pair of thrust bearing at the driver side and a journal bearing at the impeller side lubricated continuously during the compressor operation and the lubricant is gravity-drained back to the oil reservoir through the passages inside the casing and external piping. Trane Inc. provided a new pair of thrust bearing because the old ones were completely damaged. The old journal bearing was used in reassembling after passing the required inspection. The new thrust bearings were oven heated prior to the installation and installed on the shaft with respect to the required installation procedure. The journal bearing was installed after the shaft was located and aligned inside the casing. The bearing cover rings were bolted after inspecting the required tolerances.

4. Having the shaft assembled in the first step, it was decided to couple the shaft to the external motor's shaft and run the external motor in order to perform the vibration analysis and balancing before adding the 2nd stage impeller and the diffuser casing.

5. A stand was designed and built on the compressor platform to have a 300hp electric motor replace the original driver. The new shaft was designed longer than the original one in order to extend beyond the casing cover and be coupled to the new motor's shaft. The back cover plate of the motor casing was modified to let the shaft passes through and a new seal ring was provided to seal the oil coming from the thrust bearings. The motor was coupled to the shaft using a RING-flex Disc Couplings. This coupling provides reasonable tolerance for vibration analysis. A local company aligned the motor shaft with compressor shaft with the required coupling tolerances. The male and female coupling casings were bolted together to complete the coupling procedure.

6. The power line in the lab is 410 volts and a frequency controller provides the required power to run the motor with variable RPM, therefore, the motor was wired from the frequency controller at it's new location.

7. In the commercial setup the control box on the compressor's platform has various control instruments for operating the whole unit. The controlling process includes warming the oil prior to the operation in order to overcome the cooling effect from refrigerant and provide proper viscosity. In the modified setup, the control box was equipped with a transformer to provide the power to the oil pump and heater, an alarm for the required initial pressure in the oil supply line, and monitoring devise to control the maximum oil temperature. In the commercial setup the heat generated by friction was balanced with the refrigerant cooling and in the new design, the unit was cooled naturally by air. Therefore, the oil temperature rises naturally and there is no need for prior heating. In fact, the natural heating would be limiting because if the temperature of the oil increases more than 250 Fahrenheit, the lubrication process will fail. Hence, an alarm was provided to notify the maximum limit of the operation by monitoring the oil temperature in side the oil tank. It was found that there would be a window of one-hour experiment duration depending on the RPM.

8. After testing the coupling between the motor and compressor, the 2nd stage impeller was installed and the same procedure (4) was successfully repeated. Finally, the diffuser casing was installed and a Trane specialist approved the assembling process after performing the last vibration analysis.

9. Instead of reassembling the rest of the compressor components, a new inlet was designed in order to simplify the reassembling process and make the test rig practical for

adding any other parts for future investigations. In the previous plan, parts had to be assembled and reassembled very often and their extensive weight and size would make the process very expensive in time and labor. Therefore, after the seal ring of the 2nd stage impeller was installed, instead of installing the 1st stage return channel, a metal sheet was rolled into the casing opening of the 2nd stage impeller. Rather than installing the 1st stage return channel, the roll was designed to have ears on the side in order to bolt the roll to the casing. Because of the large size of the 2nd stage inlet, a reducer with a 12-inch diameter flange was welded to the roll afterwards. Consequently a 12-inch flange was welded to the reducer in order to use 12-inch diameter PVC pipes at the inlet.

10. The conical outlet of the commercial unit was connected to another pipe that carries the refrigerant to the heat exchanger unit. In the current design, the outlet conic was reduced to 12-inch flange by blocking it with a plate, which had a 12-in flange cut out. In the next step, a 90-degree PVC elbow was used to turn the flow to horizontal and a 12-inch diameter PVC pipe carried the flow to the flow control valve. The valve was providing different loading conditions for the compressor. In order to save lab space, the outlet flow was turned around the test rig by using more PVC 90-degree elbows and proper supports welded to the stand in order to carry the weight of the fittings and hold the pipes horizontal. Note that no silencer used at the outlet and the flow was exhausted into the laboratory directly after passing through the valve.

During the modifications, there were various challenges regarding to the assembly details and limited equipment resources in the laboratory. Parts were rusty because the compressor casing was made of cast iron and exposed to humidity in the atmosphere. One important fact about the installation was since the machine was

centrifugal; there was no need for the platform to be bolted to the floor. Contrary to reciprocating machines where forces make the machine "walk", in the centrifugal machines, if all the rotating parts are balanced, there will not be any motion since the forces are canceling each other. However, in this setup special rubber pads were located underneath the platform that provides enough friction to prevent any small motions.

In addition, there was a minor change in the lubrication. In the commercial setup, the oil shoots out of the journal bearing and is mixed with the refrigerant. Down stream this oil is separated from the stream and returned to the oil tank. In the current setup, when the compressor was running at higher than 2000 RPM oil leaked from the bearing but the amount depend on the load of the compressor. In order to avoid or at least reduce the amount of leak, more breath room was provided to the oil gravity drained loop by adding a "T" on the top of the oil tank. One side of the "T" was guided to the side of the compressor for breathing and refilling the tank and the other side was bolted to two flanges on the old motor casing. This return would provide the atmospheric pressure inside the motor casing. This modification reduced the leak significantly, however, oil was detected at the volute outlet at high speeds.

3.2 INSTRUMENTATION OF THE FACILITY

3.2.1 OVERALL PERFORMANCE INSTRUMENTATION

As previously explained, for performance analysis, the values of total and static pressures, temperatures and mass flow rate at the inlet and outlet of the compressor are of importance. Therefore, the following describes them individually:

3.2.1.1 TOTAL TEMPERATURE

The total temperatures were measured utilizing two United Sensor TCS-12-K-36-C-1-F temperature/thermocouple probes at the inlet and at the outlet. These probes are used to measure total temperature of air, gas or liquids in industrial application. These probes measure temperatures up to 2000°F in velocities from 100 to 2000 ft/sec. A variety of complete line of exposed-loop, insulated junction, radiation shielded, stagnation shielded and aspirated shielded is available and all are constructed of stainless steel. The type TC is commonly used in all types of compressors for efficiency measurements and up to 500°F.

3.2.1.2 TOTAL AND STATIC PRESSURES

Two United Sensors Kiel probes KBC-8 were utilized in order to measure the total pressure at each side of the impeller. These probes are used to measure total pressure in a fluid flow where the direction of flow is unknown. They can measure pressures in flows up to Mach 1.0 with some considerations for pitch and yaw angles. The outstanding advantage of Kiel probes compared with other total pressure probes is complete insensitivity to direction of the flow within certain limits. Their yaw and pitch characteristics are generally the same although stem interference on some designs will change one from the other.

The probes were setup in this test rig such that the average values of pressure were obtained by connecting the probes to each other by a "T" and reading the value at the outlet of the "T". Note that in both total temperatures and pressures, the probes were

installed in the direction of the mean flow path and immersed into the flow 1/3 of diameter of the pipe based on ASME standards for flow measurement.

Four steel capillary static pressure taps with an outer diameter of 1/16 inch were inserted at 90-degree intervals into the 12 inch diameter PVC pipe at the inlet and outlet. Static pressures were measured by averaging the readings from the four pressure taps. The surface of the taps were sanded and flushed to the surface in order to reduce the error in reading the static pressures. The average measurements of the three taps on the top and sides of the pipe surface were utilized because the leaking oil collected on the bottom surface of the pipe, making the tap at that location unusable.

3.2.1.3 MASS FLOW RATE

In this investigation, a thin plate orifice was used at inlet to compressor in order to measure the mass flow rate. An orifice is considered an obstruction of the flow in the basic duct of diameter D, where the flow is forced through an obstruction of diameter d. The β ratio of the devise is the key parameter

$$\beta = \frac{d}{D} \tag{3.1}$$

After leaving the construction, the flow may neck down even more through a vena contracta of diameter $D_2 < d$. Applying the Bernoulli and continuity equations for incompressible steady frictionless flow to estimate the pressure change will result in an ideal volume flow rate. However, the effect of the vena contracta and friction in the flow forces to calibrate the idea mass flow rate considering a discharge coefficient to fit relation

$$Q = A_t V_t = C_d A_t \left[\frac{2(p_1 - p_2)/\rho}{1 - \beta^4} \right]^{1/2} \tag{3.2}$$

where subscript t denotes the throat area of the obstruction. The discharge coefficient C_d accounts for discrepancies in the approximate analysis. By dimensional analysis for a given design it is expected

$$C_d = f(\beta, \mathrm{Re}_D) \quad \text{where} \quad \mathrm{Re}_D = \frac{V_1 D}{\upsilon} \tag{3.3}$$

Indices 1 and 2 indicate the inlet and outlet of side of the orifice and multiplying (32) by the density of the air, the mass flow rate will be calculated.

The thin plate orifice can be made with β in the range of 0.2 to 0.8 where the hole diameter d should not be less than 12.5 mm. To measure P_1 and P_2, three types of tappings are commonly used:

1. Corner taps where the plate meets the pipe wall

2. D: ½ D taps: pipe wall taps at D upstream and ½ D downstream

3. Flange taps: 1 inch upstream and 1 inch downstream of the plate, regardless of the size of the pipe

In this investigation type 2 which ASME standards recommends the following correlations resulting from curve fit:

$$C_d = f(\beta) + 91.71\beta^{2.5} \mathrm{Re}_D^{-0.75} + \frac{0.09\beta^4}{1 - \beta^4} F_1 - 0.0337\beta^3 F_3$$

$$f(\beta) = 0.5959 + 0.0312\beta^{2.1} - 0.184\beta^8 \tag{3.4}$$

where the correction factors F_1 and F_2 for this type of orifice are 0.4333 and 0.47.

Mass flow rate was measured by installing a ¼ inch thick orifice plate with $\beta = 0.63$ between two flanges at the inlet based on ASME standards for flow

measurements. Eight static taps were put on 1.5D and 2.5D across the orifice, four on each side, 90 degrees apart. The ambient temperature and pressure were used to calculate the density of the inlet flow. The standard mass flow rate measurements were performed utilizing these static pressure taps and calculated density, White (1999).

Note that the pressure measurement across the orifice was used to determine the operating condition of the compressor from surge to choke by monitoring the flow oscillation at surge in the inlet. For all the pressure measurements, handheld OMEGA pressure sensors were initially utilized but as will be described later, the Scannivalve pressure scanner replaced the handheld sensors.

3.2.2 FLOW STRUCTURE INSTRUMENTATION

The flow structure was studied by measuring the static pressure distribution over the inner surfaces of the vaneless diffuser and volute. Because of the high magnitudes of velocity and pressure, instruments such as hot-wire could not be used. Optical techniques were not useful either since providing optical access would be very expensive for a machine with the size of the Trane compressor.

3.2.2.1 VOLUTE PRESSURE TAPS

In the first step, when the volute inner surface was accessible during the reassembling process, a fixture was designed to hold a Magna drill on the volute's flange in various orientations. Because the volute casing was an inch thick, the fixture would help to hold the drill in an orientation that the drill bit was perpendicular to the casing in any angle with respect to the compressor shaft axis.

On the casing of the volute 3/8 inch holes were drilled at 45 degree intervals circumferentially and in different axial locations. The holes were first tapped and filled with epoxy and later the dried epoxy was drilled for 1/16-inch O.D. static pressure tap inserts. Similar to the taps at the inlet and outlet, the steel pipe inserts were cut and sanded on the tip. The epoxy on the volute casing was sanded from inside prior to drilling and the steel capillary pipes were inserted to be flush with the surface.

3.2.2.2 VANELESS DIFFUSER PRESSURE TAPS

In the diffuser, the same strategy was followed with minor changes. Holes were drilled every 60 degree circumferentially on the diffuser cover at different radial locations from impeller exit to before the diffuser bend. The desired locations were as in the volute but because of the structure of the diffuser cover casing, it was impossible to drill holes at every 45-degree. The casing had bases on the back in order to carry the vanes inside the return channel after the first stage. The holes were drilled for 3/16-inch I.D. steel pipe inserts and similar to inlet and outlet static taps, the tips were sanded and inserted flush to the surface of the diffuser cover.

There were pressure taps on the surface of diffuser cover that were initially used in Trane's design experiments. These taps were distributed at every 120 degrees at the inlet and outlet of the diffuser. Pressure taps were provided in addition to the Trane taps so that overall distribution included two taps installed at each 0, 120, 240 degrees and six at each 60, 180, 300 degrees and different radial locations. In addition, there were three total pressure taps were provided by Trane at every 120 degrees and depths of 25,

50 and 75 percent of the diffuser width. Note that Tygon tubes were utilized to connect both volute and vaneless diffuser's pressure taps to the pressure scanner's ports.

3.2.2.3 PRESSURE SCANNER

Due to the large number of the points on the volute and vaneless diffuser to be measured, two 16-channel differential Scannivalve DSA3017 pressure scanners were purchased. The DSA3000 series pressure acquisition systems represent the next generation of multi-point electronic pressure scanning. Model DSA3017 Digital Sensor Array, incorporate 16-temperature compensated piezoresistive pressure sensors with a pneumatic calibration valve, RAM, 16-bit A/D converter, and a microprocessor in a compact self-contained module. The result is a network ready intelligent pressure-scanning module.

The microprocessor compensates for temperature changes and performs engineering unit conversion. The microprocessor also controls the actuation of an internal calibration valve to perform on-line zero and multipoint calibrations. This on-line calibration capability virtually eliminates sensor thermal errors with a long-term system accuracy of $\pm 0.05\%$ full scale (FS). Pressure data are output in engineering unit via Ethernet using TCP/IP protocol.

The DSA3017 Digital Sensor Array is ideal for flight and turbine engine testing applications where ambient temperatures vary. It is also ideal for industrial pressure measurement where long calibration intervals are required or temperature can vary greatly. The DSA temperature compensated pressure sensors are more than ten times less sensitive to temperature than typical piezoresistive pressure sensors. They are not

attitude sensitive, so the units may be close coupled to the pressure sources to be measured. When further temperature stability is required or for use below 0°C, it is recommended that the Model DSA3018 to be used. The DSA3018 is basically a DSA3017 placed in an insulated, thermostatically controlled environment box.

With the initial experiments at 3600RPM, the pressure range of 2.5 PSID was selected for the units. Note that these units measure the pressures with respect to a common reference. Handheld pressure sensors were utilized to read pressures at the inlet and outlet initially but because the range of the pressures at these locations were in the range of the pressure scanners, it was decided that the pressure scanners take over the handheld sensors as well.

3.3 PLANNED MEASURMENTS

The initial goal was to find a design point for the operation of this compressor and compare the overall and component performances with an off-design condition. The design speed would determine the maximum mass flow rate that the size of the compressor could handle; therefore, the first objective was to find a design speed and the peak total-to-total efficiency point for that speed. At a certain speed, the amount of load on the compressor defines a datum point, which depends on the amount of mass flow rate that is being compressed. In the current setup, the exit valve was responsible for varying the mass flow rate from "Choke" (maximum flow rate) to "Surge" (minimum flow rate) where the compressor stalls.

The experiments were planned to evaluate the overall and component performances of the compressor at three speeds of 2500, 3000 and 3600 RPM. As

mentioned in previous sections, there were two limiting factors for not performing experiment in higher RPM. The first factor was the oil leakage at higher speeds and second was the air-cooled compressor. Hence, the performance experiment was performed at 2000RPM initially in order to avoid the higher RPM and to evaluate the efficiency of this compressor and consequently the design point. The result of the first set of experiments failed to show the general characteristics of a compressor on efficiency and pressure ratio diagrams. After checking the Excel spreadsheet's calculation for accuracy, a second set was performed but failed again. One of the main reasons for the failure was the outlet temperature variation that made the efficiency calculations wrong. In turbomachines, the thermal stability is essential and the larger the compressor is the longer the stability duration will be therefore; in the next set of the experiment data were collected every 15 minutes for every point. After obtaining initial data points, it was found that the waiting period should be longer since the temperature was still varying.

After observing the above, it was decided to change the strategy and take advantage of the physics of the flow inside the vaneless diffusers, as described in the theory, to find the design point of this compressor. The strategy was based on pressure measurement inside the vaneless diffuser and will not consider the total-to-total efficiency, which requires temperature measurement. Therefore, the pressure scanners were a great advantage in making the duration of the experiment shorter and collect more accurate data. The experiments were performed at speeds of 2000, 3000 and 3600 RPM and the data was analyzed to study the performance of this compressor.
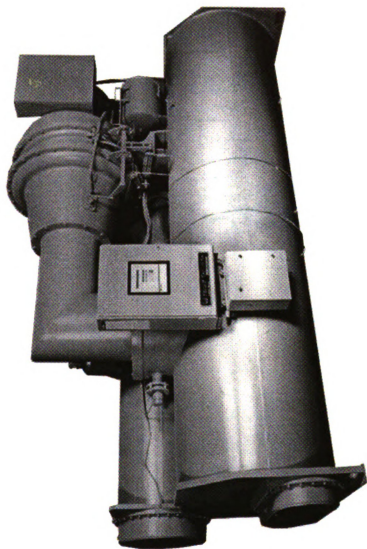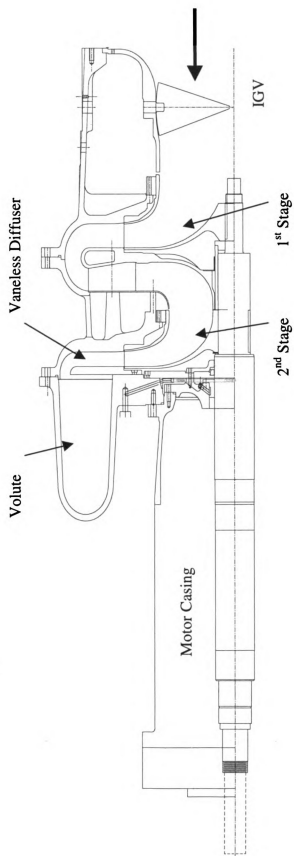
FIGURES

Figure 3.1: CVHF 1280 Trane Commercial Unit
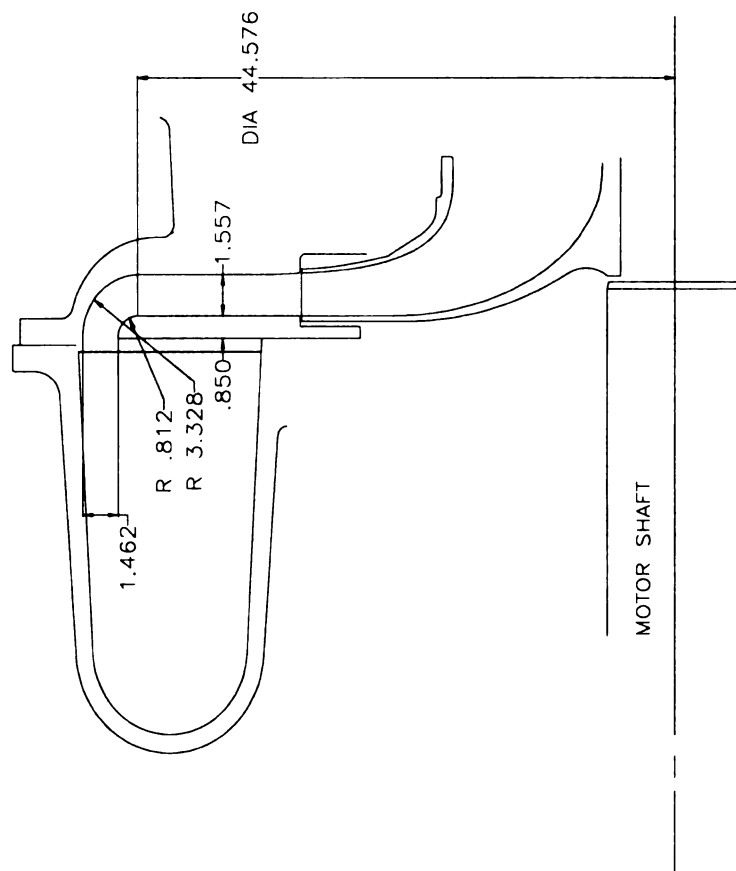
Figure 3.2 Trane two stage compressor's cross-section

Figure 3.3: Diffuser dimensions for setting up the flow path

CHAPTER 4

EXPERIMENTAL RESULTS AND ANALYSIS

In this chapter different approaches are described for the experimental analysis of the compressor performance. The experimental results for the vaneless diffuser and volute are analyzed. Results of the meanline analysis of the compressor impeller are presented. A few design modifications are suggested for future investigations on this compressor.

4.1 DIFFERENT APPROACHES

As mentioned previously, the first objective was to evaluate the compressor's performance curve with air as the working fluid. In order to achieve this goal, various experiments were performed to evaluate the isentropic efficiency of the compressor for different loads and speeds utilizing total pressures and temperatures at the inlet and outlet. At every speed, one load would determine the optimum operating point of the compressor.

After preliminary experiments, efficiencies were evaluated close to 100%, which were very unrealistic. The primary reason for such results was that the thermal equilibrium plays a major role in the performance calculation of turbomachines. The larger and the higher speed of the machine, the longer the time to reach thermal stability. Therefore, in this situation, the data should ideally be collected over a longer time frame and with compressor being air-cooled. This procedure was impossible due to the limited available running time because of the oil temperature rise in this setup. Therefore, an alternative approach had to be taken to evaluate the design point.

Meanwhile, possible oil droplets in the exit flow might have cooled the thermocouples as well. The reason for droplets existence was the design of the bearing

99

seals based on the pressure difference across the seal. In the commercial, unit the mass flow rate and the number of stages were different, therefore, the pressure difference across the seal is different than the new operating condition. This fact would lead to oil leakage in the current standard journal bearing seal. In order to improve the performance of the seal, portion of the seal was machined and a rubber shaft seal was added in front of the old seal. Adding the rubber seal increased the friction on the shaft and frequency controller, which provided the driving power to the electrical motor, couldn't sustain the required initial torque to start the compressor. Thus, running the compressor for the next set of investigations is due to adjusting the frequency controller for the initial required torque in the new configuration. However, the addition of the rubber seal happened when all the experiments of the alternative approach were performed. A better way to stop the oil leakage is to redesign the bearing seals by the company for air as the medium.

Another alternative approach could have been obtaining the performance curve of this compressor based on the definition of the efficiency but with different perspective. As noted before, the isentropic efficiency is the division of the ideal power by real consumption power in compressors. The real consumption power is calculated from first law of thermodynamics, which leads to total temperature ratio term in the efficiency calculation (1.3). The ideal power is obtained during an isentropic compression and by using the isentropic relations and the first law of thermodynamics; the total temperature ratio is converted to the pressure ratio term in the efficiency calculation. The mechanical power is impossible to measure in compressors; therefore, thermodynamical definition of power is used, which can be calculated from measuring

the fluid properties at the inlet and outlet of the compressor. If the braking power were measurable, the efficiency of the compressor would have been obtained utilizing those techniques similar to the internal combustion engines techniques for measuring the efficiency.

In this compressor, however, the input power could be measured by the electrical power input to the compressor. Having a constant voltage provided to the motor and measuring the consumption current, the electrical power input to the compressor motor could be calculated. There are losses in the frequency controller and power transmission, which have to be included to obtain the net power consumption in the compressor operation at every load. This power could replace the total temperature ratio term in the denominator of the efficiency definition (1.3) and the pressure ratio term in the numerator represents the ideal work input to the compressor, hence efficiency could be calculated for every load. There would be a small error in this method, which is due to the neglecting the electrical losses.

In this investigation, this technique was not utilized to find the best operating point of the compressor, instead the load with highest pressure ratio was referenced as a point with mid mass flow rate for the analysis. The reason behind such a selection was, even though the compressor works at off design, the operating conditions at the largest pressure ratio will be the closest to the optimum conditions when efficiency data can not be utilized. Since the focus of this investigation was performance of the volute as a component, evaluation of the stage performance left for the next investigation on this test facility utilizing the technique discussed above.

4.1.1 DIFFUSER RESULTS

In this investigation, the diffuser behavior was initially the essential component for defining the operating point. As described in Chapter 2, at a lower mass flow rate than the optimum point, there is not enough mass flow to fill the space, hence diffusion occurs. On the other hand, at higher flow rates, only by acceleration in the flow will the mass flow be conserved. Therefore, there would be a balance point between the two cases, which provides the highest efficiency of the compressor. Collapse of these points for a certain mass flow rate indicates a uniform circumferential pressure distribution at the diffuser exit and guarantees the best operation of the whole stage. In this condition the components are "matched" with each other.

To study this fact, the vaneless diffuser static pressure distribution was mapped by the pressure taps provided radially and circumferentially (Figure 4.1a). Hand held pressure sensors were initially utilized but with evaluation of the pressure range in the experiments, they were replaced with pressure scanners because of higher accuracy in their pressure range. Therefore, all the pressure taps on diffuser cover, inlet, and outlet to the stage were connected to the pressure scanners and measurements were repeated for the speeds of 2000, 3000 and 3497 RPM, which was the highest speed that the motor could reach. Figure 4.2 shows total pressure ratio versus flow coefficients from choke to close to surge at 2000 RPM. Figures 4.3-5 shows circumferential pressure distribution at different radius ratios on the vaneless diffuser shroud wall. The data points in each plot present the circumferential static pressure distortion for every radius ratio. As motioned before, at one flow coefficient point, the data points should have collapsed to represent the balancing point in the operation of the diffuser. Collapse of these points would have

shown zero circumferential static pressure distortion at each radius ratio. The numerical analysis will show that this distortion is because of the tongue effect in Chapter 6.

Figures 4.6-7 show the diffuser radial pressure distribution for the same flow rate coefficients at 60 and 180-degree angles with the reference to 12 o'clock facing the front of the compressor (Figure 4.1). These results show the radial diffusion inside the vaneless diffuser. Note that with increase in speed and mass flow rate, the rate of diffusion decreases. As described in Chapter 2, for mass flow rates above design point, acceleration will occur because the diffuser will be too small and flow has to accelerate.

Figure 4.8 represents the diffuser circumferential outlet pressures for the same flow coefficients as of previous plots. It is clear that the tongue region ($\theta=240$) has significant effect on the performance of the machine by creating distortion in the circumferential static pressure distribution at the diffuser outlet. This sudden drop in the static pressure at tongue region could have a direct effect on the flow back to the inducer and impact the bearings with unbalanced circumferential loads. The performance of the vaneless diffuser is similar to ones from other researchers presented in Chapter 2. The maximum and minimum pressure drops at the tongue region with respect to the average pressure at the diffuser outlet are 8.4% and 6.9% for this speed. Figures 4.10-16 and 4.18-24 are the similar results for the speeds of 3000 and 3497 RPM. Comparing Figures 4.2, 4.10 and 4.18 it is concluded that for air this compressor provides larger pressure ratios at higher speeds.

In the next chapter, three points were selected for the numerical analysis with minimum and maximum flow rates and a point with the largest pressure ratio (Figures 4.2,10,18) as the mid mass flow rate. The maximum and minimum pressure drops at the

tongue region are 11.8% and 8.0% percents for 3000 RPM and 12.1% and 8.3% for 3497 RPM respectively. This shows that at higher speeds and mass flow rates the impact of the tongue is less significant. Figure 4.20 shows that the compressor is close to the point where the data points will collapse at one mass flow rate. To reach the best operating point, where the components are matched, requires running the compressor at a speed higher than 3497 RPM, which is impossible with the current driver.

Note that the radius ratio of 1.125 is very close to the impeller tip, which implies that this point might be close to or in the unsteady impeller wake region of shear zone off of the impeller. In order to study the flow in this region unsteady pressure measurement equipments should be utilized for future experiments.

4.1.2 VOLUTE RESULTS

In order to map the static pressure distribution in the volute, pressure taps were provided as far as the geometry of the volute cross sections allowed. These taps were located on the flat portions of the volute casing, where normal drilling on the surface was possible. Therefore, depending on the circumferential locations on the volute casing, one to three taps were provided. These pressure ports were scanned for similar mass flow rates and speeds as the diffuser experiments. Results were averaged axially for every cross section at every operating point and shown in Figures 4.9, 4.17 and 4.25. Note that the reference of the angle in these plots is the tongue location, Figure 4.1.

The volute static pressure contours in numerical results and experimental data collected from each tap show that the axial variation of the static pressure on the volute casing on the outer diameter region of volute cross sections is not large. Therefore, this

averaging can be a good representative to compare the static pressure at different volute cross sections. However, the pressure distribution inside the volute may vary radially, which affects the flow structure inside the volute.

Reviewing the plots, the reader clearly observes that the performance of the volute is improving with increase in mass flow rate and speed. Diffusion occurs sharply in the cross sections with smaller areas and decreases as the flow enters the cone inlet. One primary conclusion would be that this volute is performing at off design condition. As was described before, the pattern of diffusion in the volute shows that the volute is too large for these mass flow rates. Experiments show that this is true for all speeds and mass flow rates.

The ideal volute performance is collecting the flow leaving the diffuser and providing uniform circumferential pressure distribution at vaneless diffuser exit. As stated previously, the uniformity of the pressure will improve the impeller and vaneless diffuser performances. Having mentioned the above, there is a large pressure drop at the tongue region between the cone and tongue entrances, which forces the flow to reenter the volute. Because of the curvature of the scroll casing the reentry flow creates a circulation region at the beginning of the scroll and corresponding losses within the volute. The CFD results will reveal this fact by calculating the vorticity magnitude at the first volute cross sections and presenting the velocity vectors in this region (Chapter 6). The flow circulation region at the beginning of the volute creates a region of low pressure and pressure recovers further downstream inside the volute.

On the other hand, the wavy shape of the plots for 2000 RPM speed indicates the nonuniform circumferential distribution of the static pressure in addition to the pressure

drop across the tongue region. Increasing the speed and mass flow rate, improves the uniformity of this pressure distribution and therefore reduces the loss in the stage operation. However, the pressure drop across the tongue region is inevitable and depends on the design of the tongue. Note that the reentrance of the flow to the volute at the tongue region could help reduce and balance the circumferential pressure drop at tongue region.

In the design of the tongue for this model, if the distance between the tongue and scroll is reduced, the length of the sharp pressure gradient region decreases and would reduce the nonuniformity of the circumferential pressure distribution. Flow could be fed to this region by a return supply line from the cone outlet to balance the pressure circumferentially. A valve can be utilized at the supply line to adjust the inlet pressure and mass flow rate to this region dynamically. This modification could improve the volute performance significantly in both the laboratory and commercial models.

4.2 IMPELLER ONE DIMENSIONAL ANALYSIS

Having the mass flow rate and impeller geometry information, a one-dimensional analysis of the impeller was performed for various purposes. In order to do the numerical simulation, boundary conditions had to be provided for diffuser inlet and cone outlet. Having only experimental static pressure data at the diffuser inlet was not sufficient for the simulation. Therefore, this analysis would provide the absolute velocity and angle of the flow leaving the impeller, which were sufficient for the inlet boundary condition.

In addition, the relative velocity ratio inside the impeller was to be evaluated. If this ratio is too small, there will be a strong pressure gradient inside the impeller passages, which leads to flow separation. At the same time, having the velocity information enables evaluation of the vaneless diffuser stability based on performance of the diffuser in Jansen chart.

Figures 4.26-27 present the results of this study utilizing the design methods described in Chapter 1 for speeds of 2000, 3000 and 3497 RPM and corresponding mass flow rates. In this analysis, absolute flow angle was calculated with respect to the radial direction. Figure 4.26 shows that the flow angles decreases as the mass flow rate increases. The cobra probes were installed on the vaneless diffuser for measurement of these angles for the future investigations. In these results C_2, absolute velocity leaving the impeller, follows the same trend of the absolute flow angle. Note that these results are based on meanline analysis and no loss was included in the analysis. However, performing the numerical simulations based on these boundary conditions led to results with good agreement with the experimental results (Chapter 6).

Referring to Jansen chart, Wilson (1998), and calculating the average Reynolds number of 2×10^6 for the flow leaving the impeller, the diffuser was stable with the flow angles between 70-75 degrees respect to radial direction. In low mass flow rates where flow angles are more than 75 degrees respect to radial direction, the vaneless diffuser becomes unstable and rotating stall occurs inside the diffuser. In general, centrifugal impellers are designed for the range of 60 to 65 degrees of absolute flow angles at the impeller exit, which is lower than the calculated range.

Figure 4.28 depicts the variation of relative velocity ratio versus mass flow rates, in which W_2/W_1 increases with increase in mass flow rate. Small relative velocity ratios mean large diffusion rate inside the impeller passages, which lead to separation of the flow and impeller stall. In order to prevent separation or reduce the separation losses inside the impeller passages, impellers are designed for relative velocity ratio W_2/W_1 about 0.7. The meanline analysis of the Trane impeller produced a maximum ratio of 0.4, since it is operating in low mass flow rates, (Figure 4.28). This predicts that the flow might be separated inside the impeller in all cases of the experiments and separation losses should be considered depending on its intensity. In comparing the cases, the loss is predicted to be the least in 3497 RPM case and increase as the speed and mass flow rate decrease. Note that the compressor's impeller was designed for a prewhirl flow at the inlet to the stage where in current investigation no inlet guide vanes were utilized. The meanline analysis was performed for uniform flow at the inlet as was in the experiments.

For the next set of experiments on this compressor, inlet guide vanes can be installed and the effect of the prewhirl flow at the inlet to the stage investigated. Numerical simulations can be performed for the flow inside the impeller as well in order to investigate the flow structures for such low relative velocity ratios. It is predicted that separated flow regions should be diagnosed inside the impeller passages.
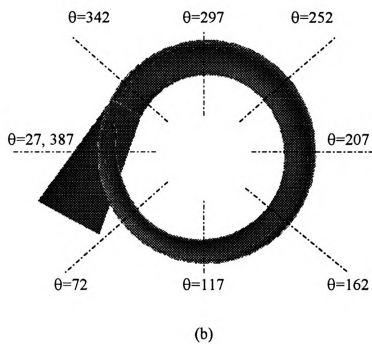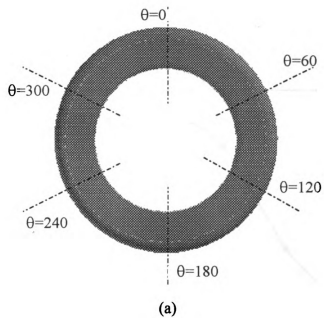
108

FIGURES

(a)

(b)

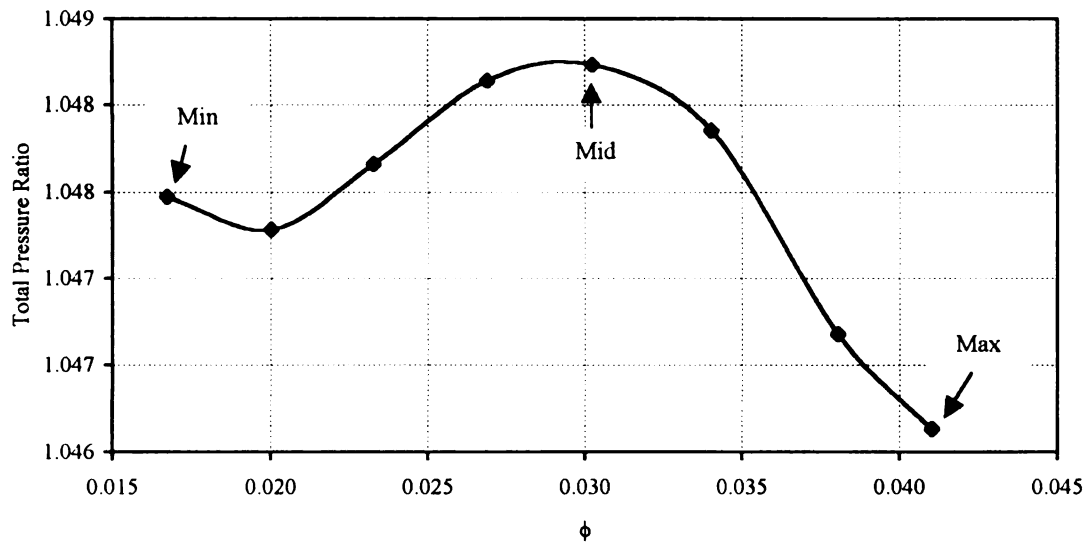Figure 4.1: Probe Locations on (a) Vaneless Diffuser (b) Volute

Figure 4.2: Total Pressure Ratio for 2000RPM Operating Condition
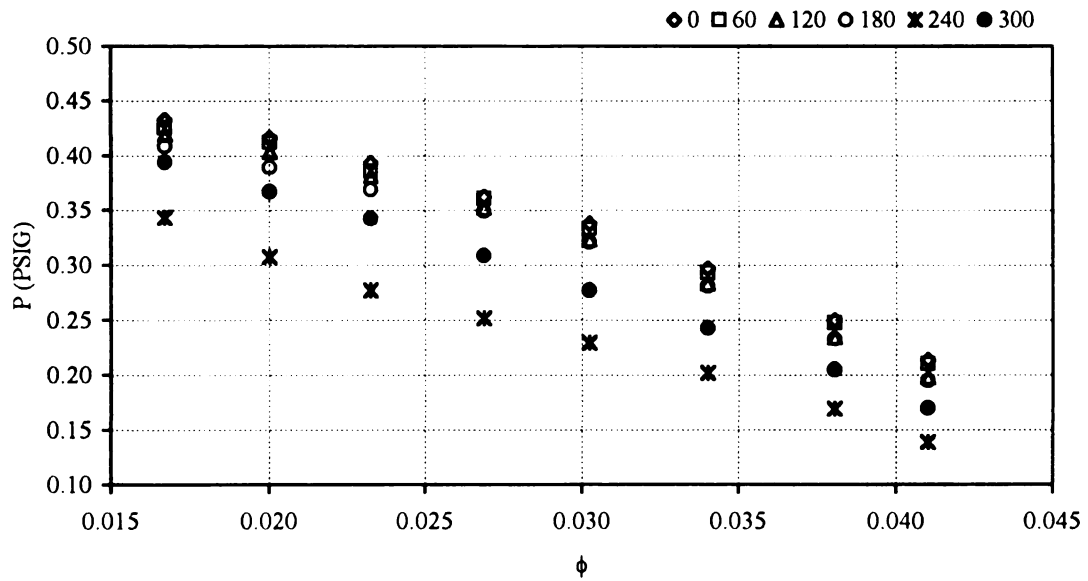

Figure 4.3: Vaneless Diffuser Static Pressure Distribution at r/r_2=1.125, 2000RPM and θ=0, 120, 180, 240, 300 Degrees
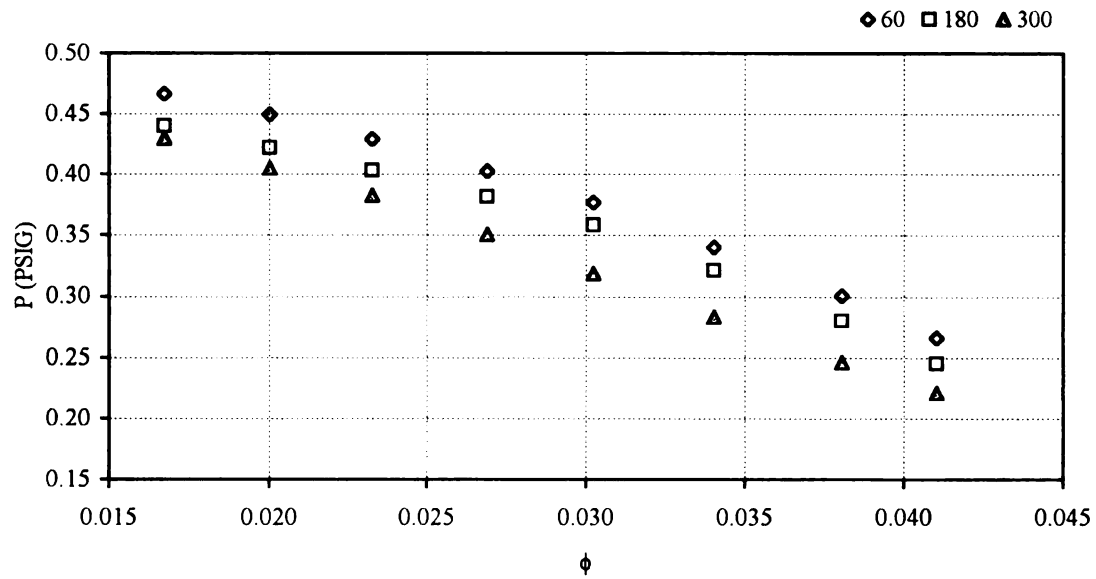
111

Figure 4.4: Vaneless Diffuser Static Pressure Distribution at r/r$_2$=1.27, 2000RPM and
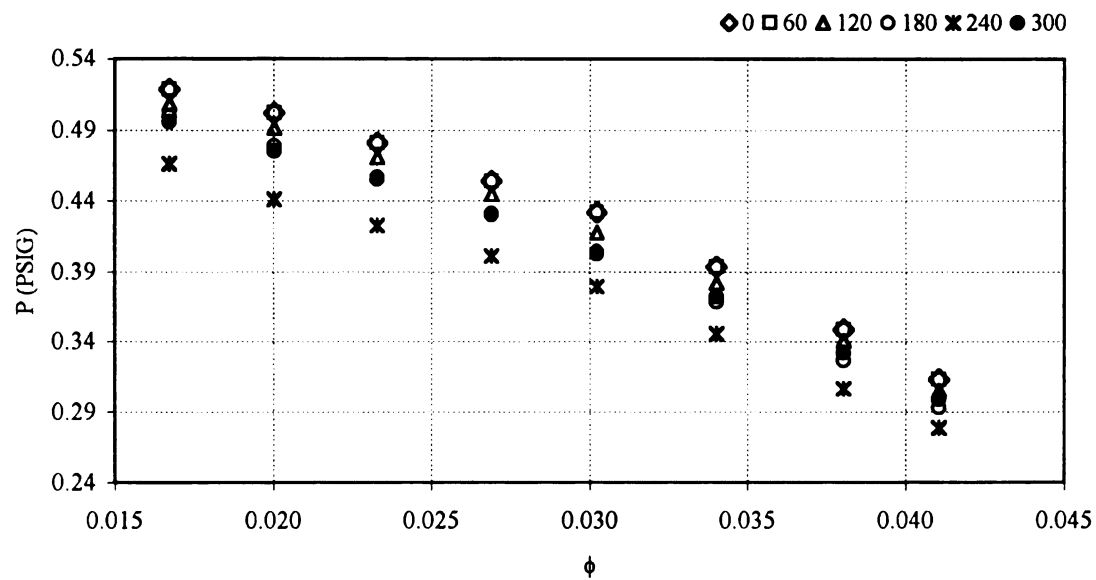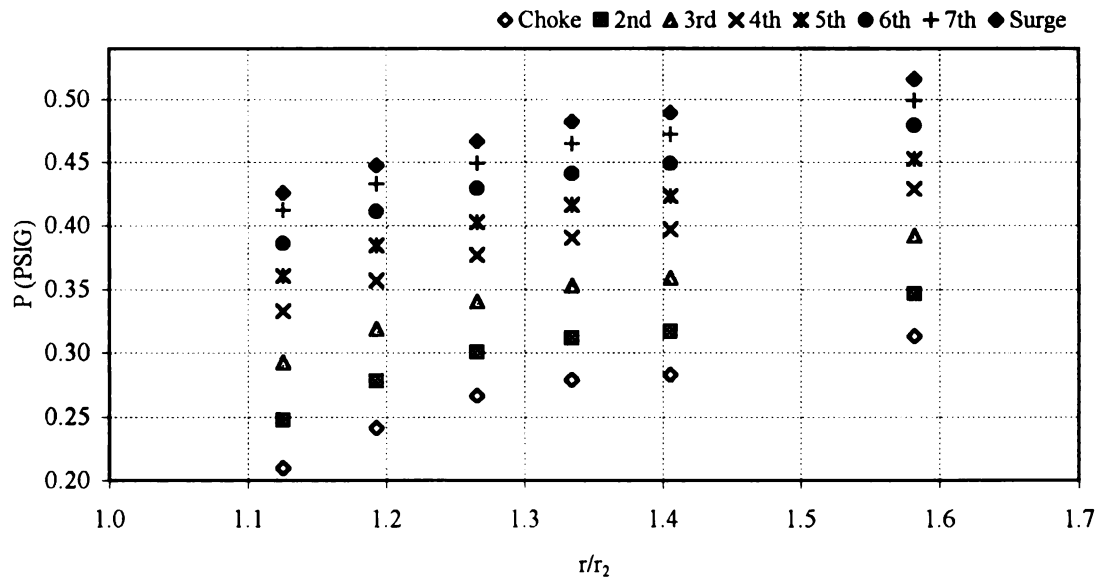θ=60, 180, 300 Degrees

Figure 4.5: Vaneless Diffuser Static Pressure Distribution at r/r$_2$=1.59, 2000RPM and
θ=0, 60, 120, 180, 240, 300 Degrees

112

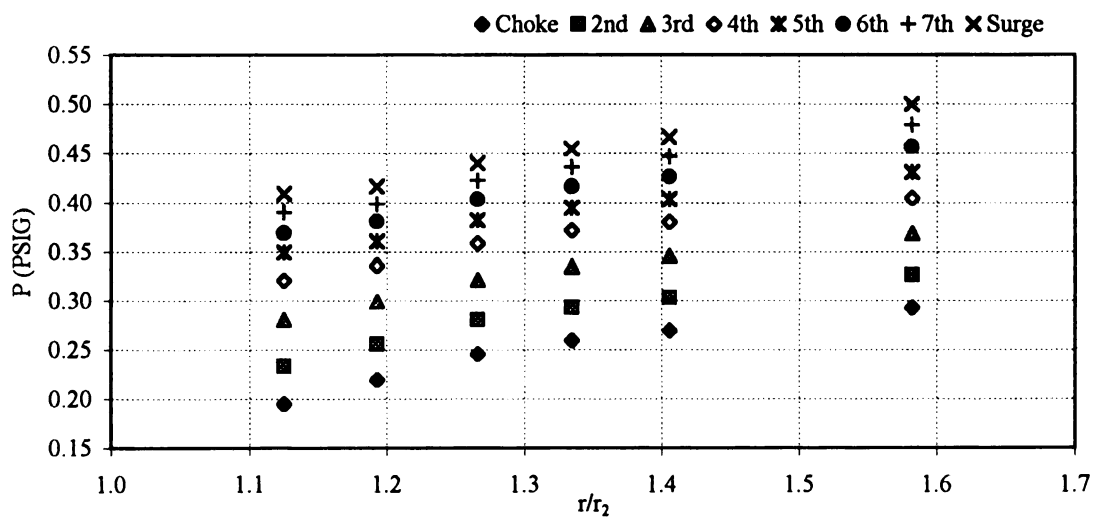Figure 4.6: Vaneless Diffuser Static Pressure Distribution at θ=60 and 2000RPM

Figure 4.7: Vaneless Diffuser Static Pressure Distribution at θ=180 and 2000RPM
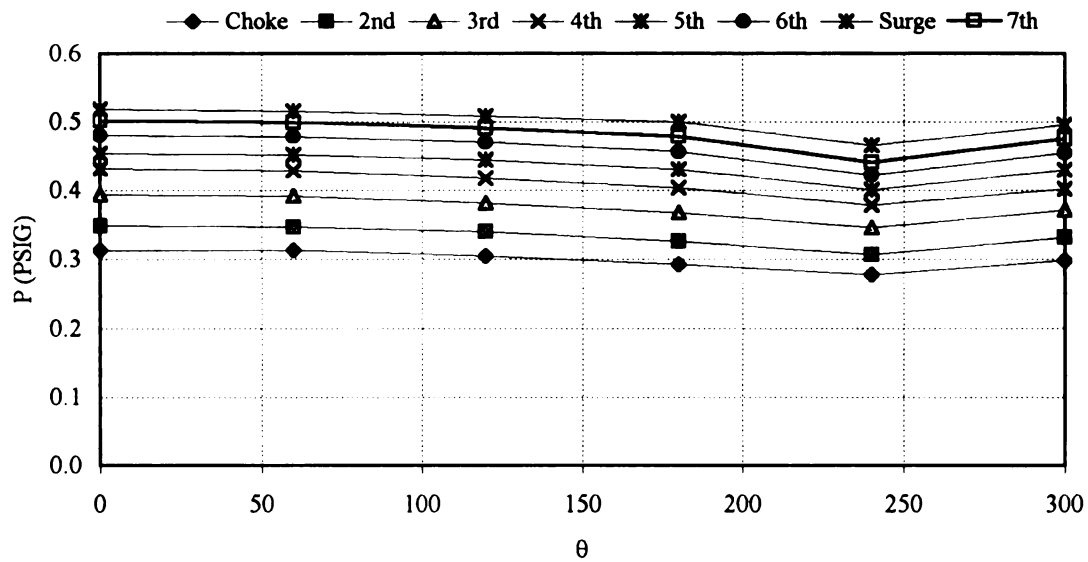
113

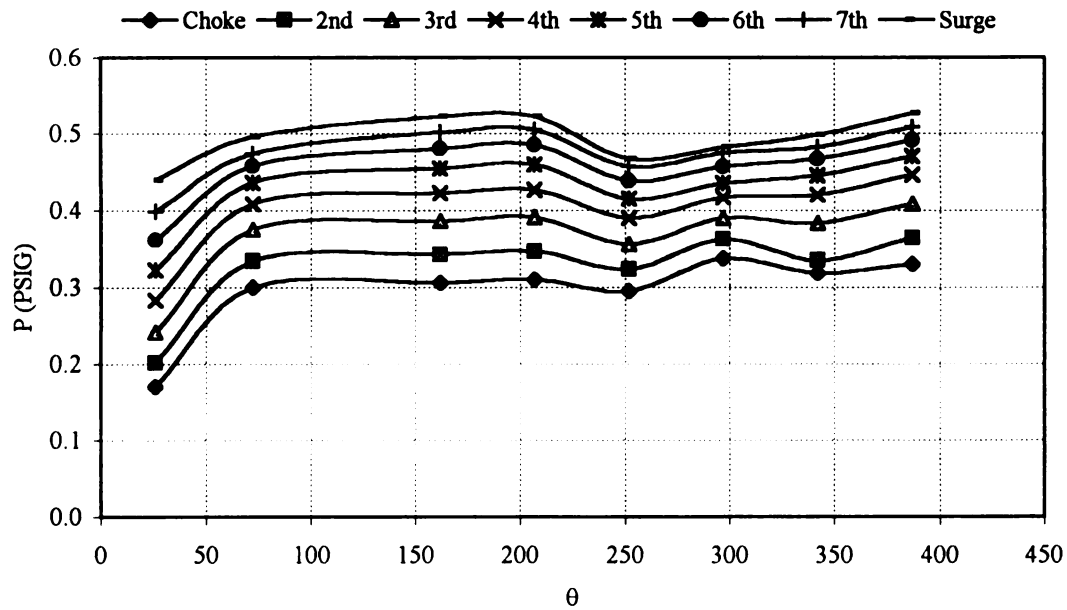Figure 4.8: Static Pressure Distribution at Vaneless Diffuser Outlet and 2000RPM

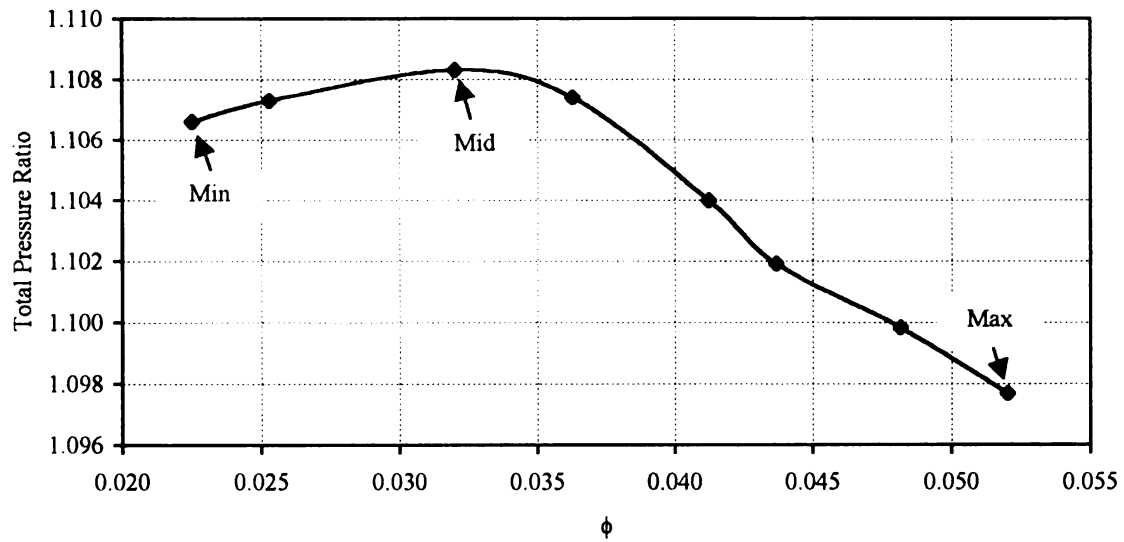Figure 4.9: Volute Static Pressure Distribution at 2000RPM

114

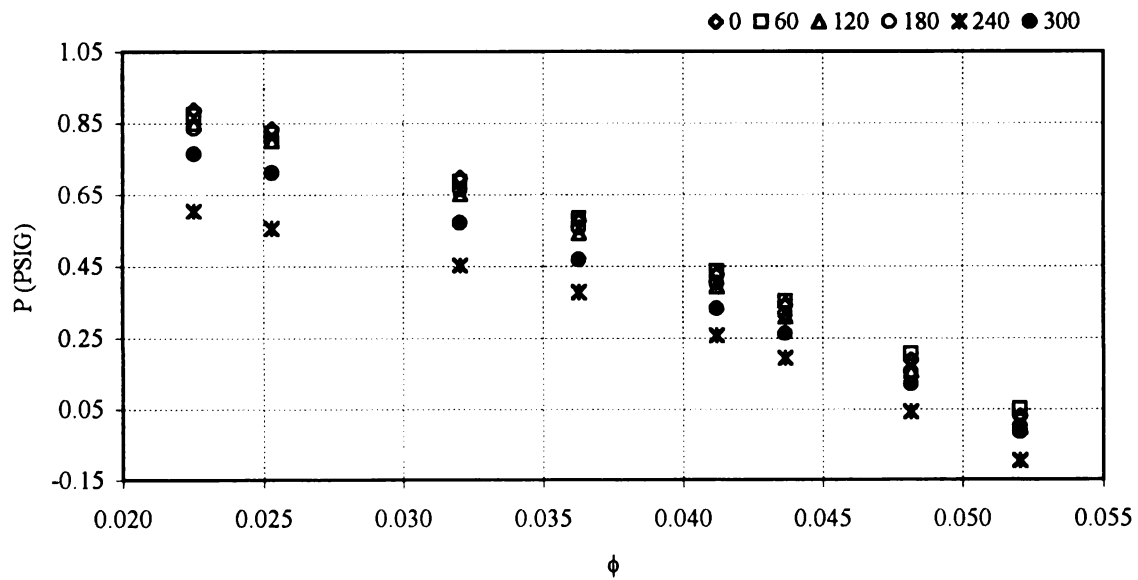Figure 4.10: Total Pressure Ratio for 3000RPM Operating Condition

Figure 4.11: Vaneless Diffuser Static Pressure Distribution at r/r$_2$=1.125, 3000RPM and
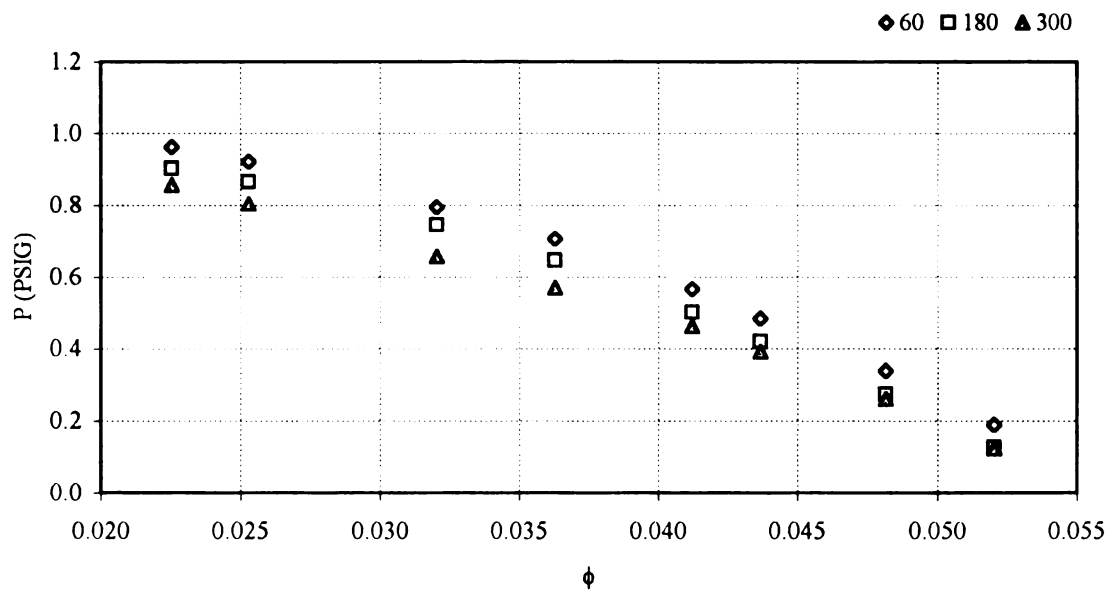θ=0, 60, 120, 180, 240, 300 Degrees

Figure 4.12: Vaneless Diffuser Static Pressure Distribution at r/r_2=1.27, 3000RPM and θ=60, 180, 300 Degrees
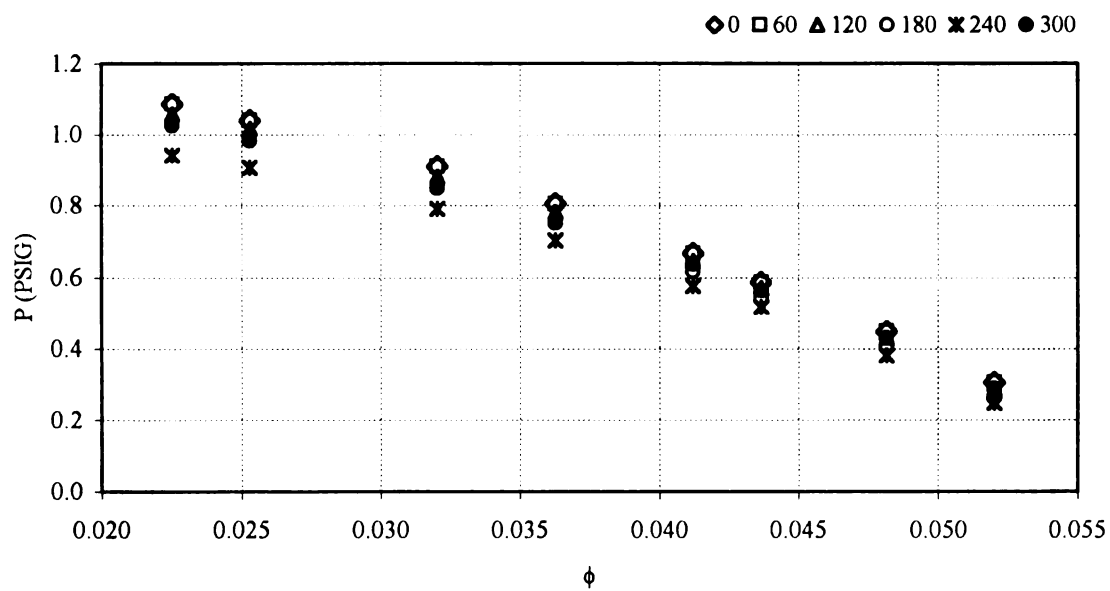

Figure 4.13: Vaneless Diffuser Static Pressure Distribution at r/r_2=1.59, 3000RPM and θ=0, 60, 120, 180, 240, 300 Degrees
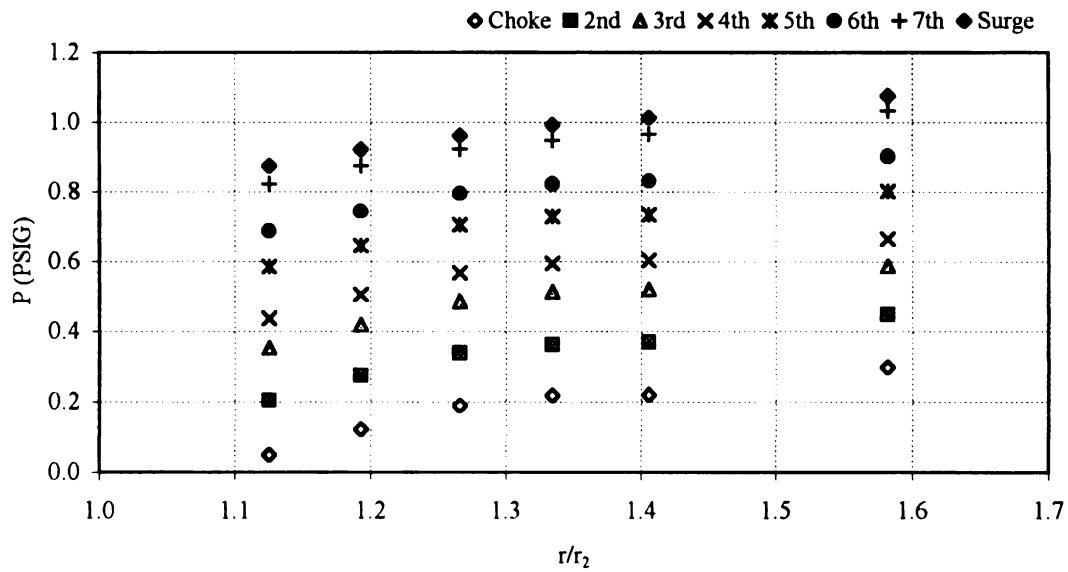
Figure 4.14: Vaneless Diffuser Static Pressure Distribution at θ =60 and 3000RPM

Figure 4.15: Vaneless Diffuser Static Pressure Distribution at θ=180 degree and 3000RPM

117

Figure 4.16: Static Pressure Distribution at Vaneless Diffuser Outlet and 3000RPM

Figure 4.17: Volute Static Pressure Distribution at 3000RPM

Figure 4.18: Total Pressure Ratio For 3497RPM Operating Condition
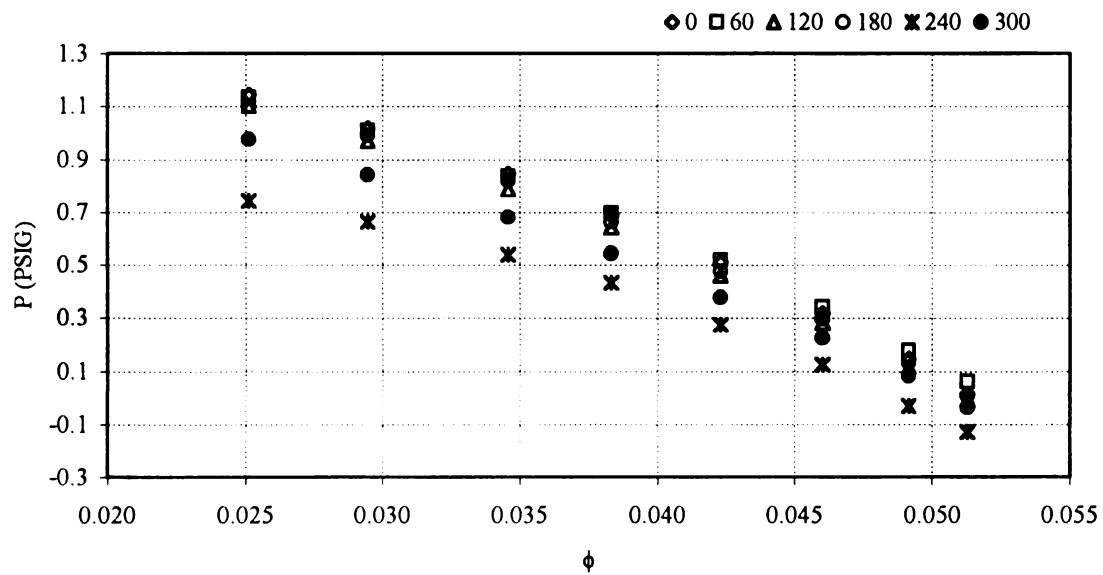
Figure 4.19: Vaneless Diffuser Static Pressure Distribution at r/r$_2$=1.125, 3497RPM and
θ=0, 60, 120, 180, 240, 300 Degrees
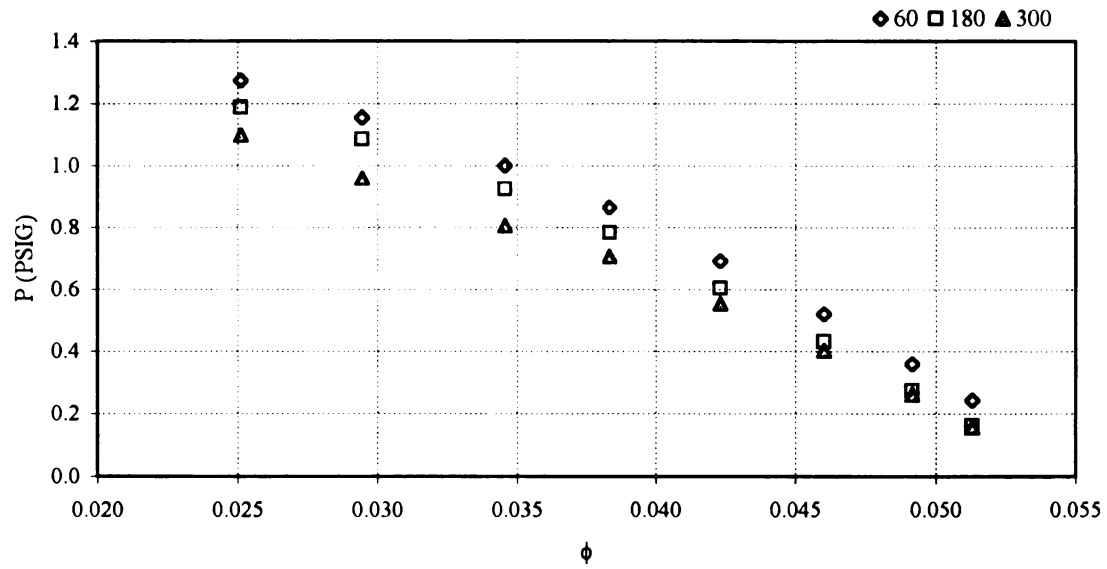
Figure 4.20: Vaneless Diffuser Static Pressure Distribution at r/r₂=1.27, 3497RPM and θ=60, 180, 300 Degrees
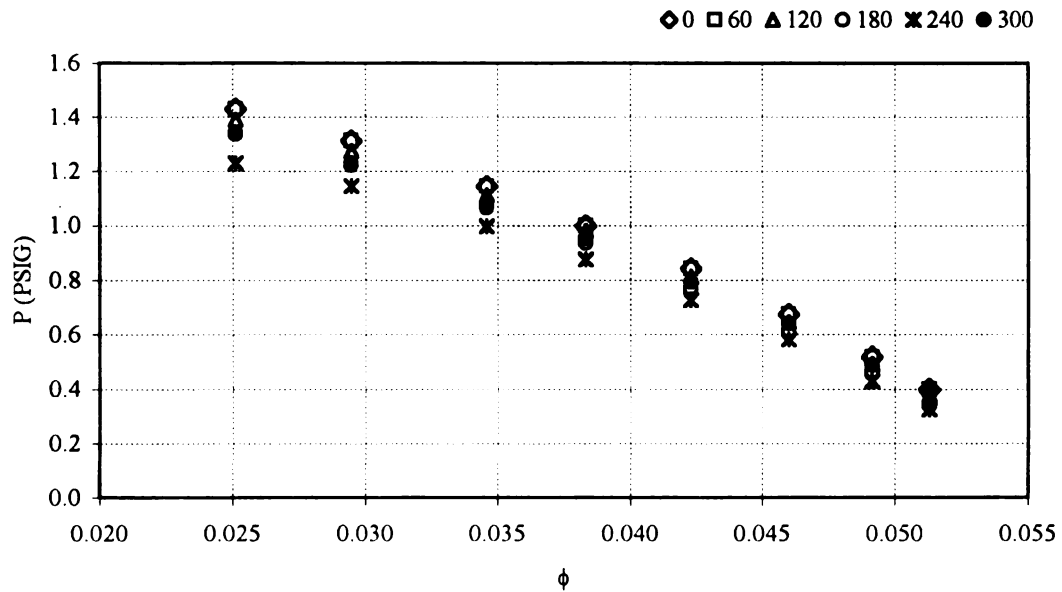
Figure 4.21: Vaneless Diffuser Static Pressure Distribution at r/r₂=1.59, 3497RPM and θ=0, 60, 120, 180, 240, 300 Degrees
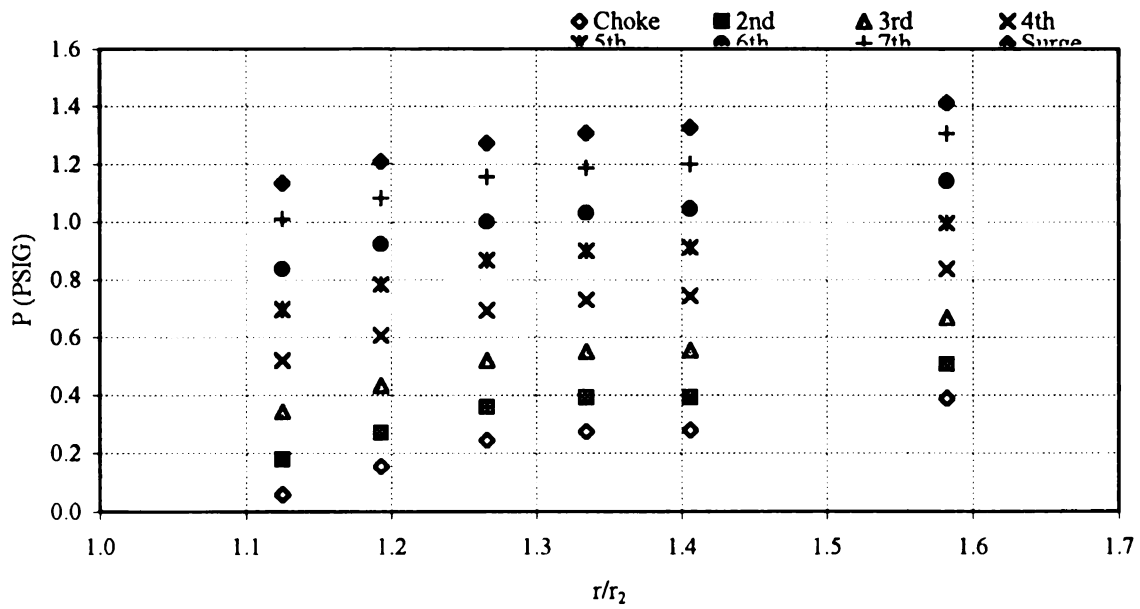
Figure 4.22: Vaneless Diffuser Static Pressure Distribution at θ=60 and 3497RPM
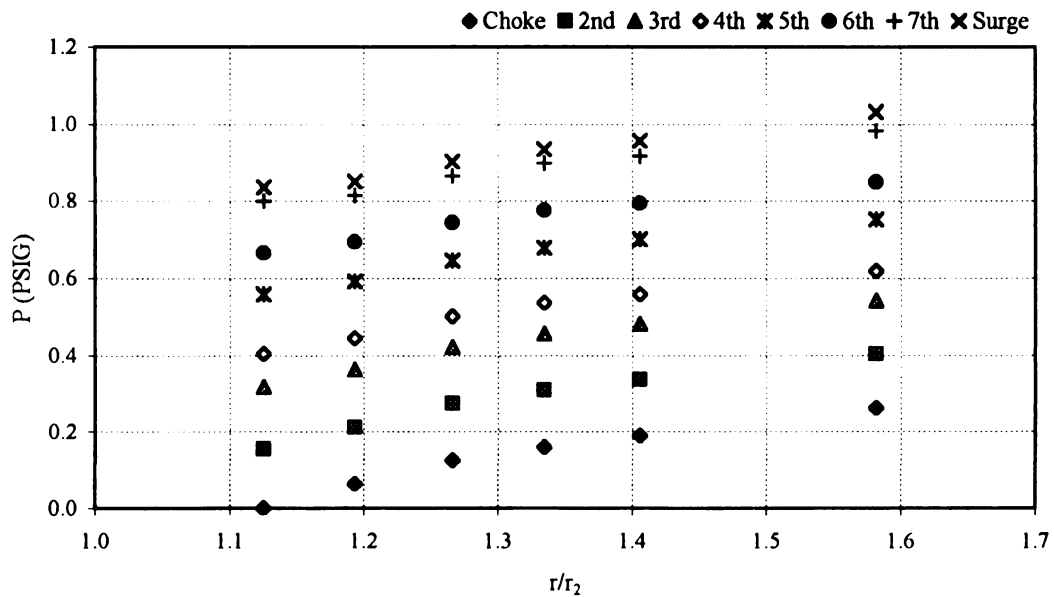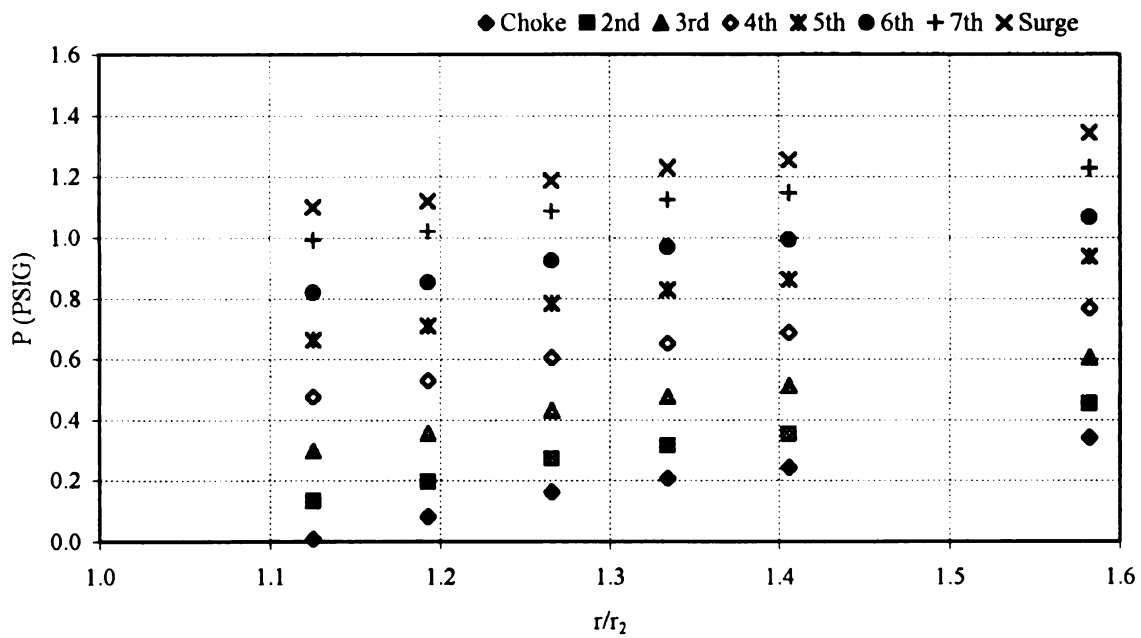

Figure 4.23: Vaneless Diffuser Static Pressure Distribution at θ=180 degree and 3497RPM
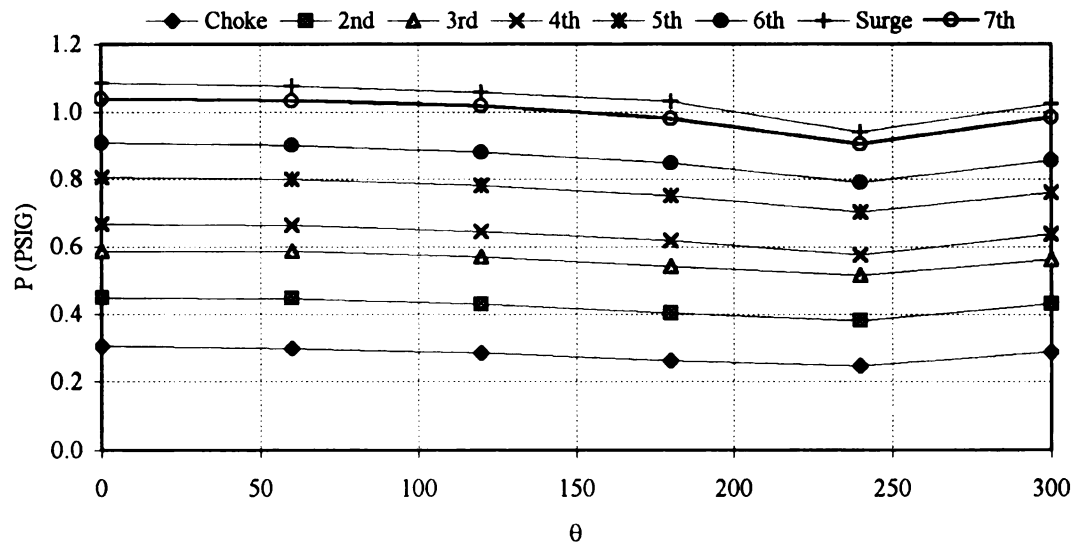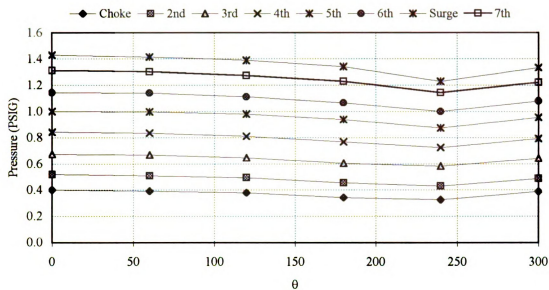
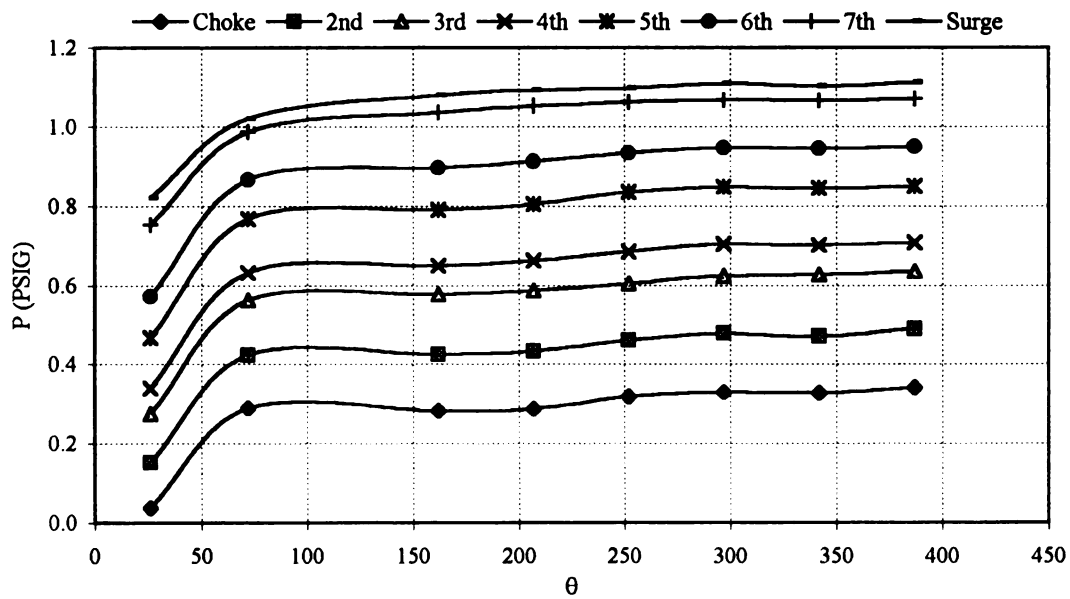Figure 4.24: Static Pressure Distribution at Vaneless Diffuser Outlet and 3497RPM
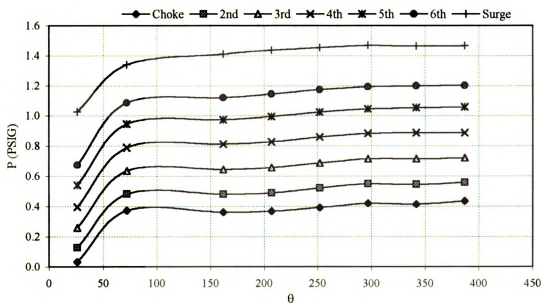
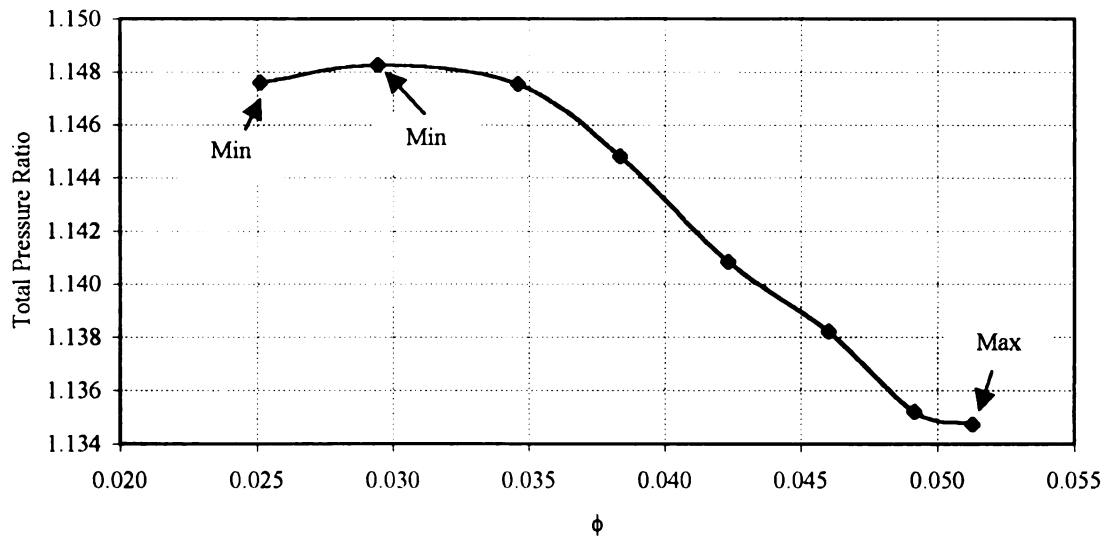Figure 4.25: Volute Static Pressure Distribution at 3497RPM

122
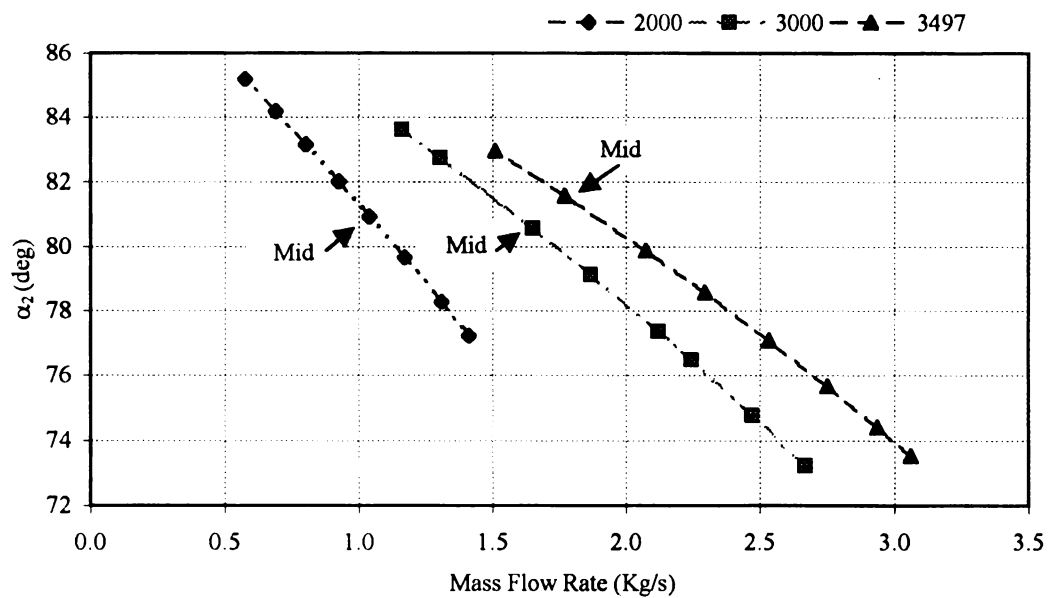
Figure 4.26: Impeller Exit Flow Angle For Different Speeds and Mass Flow Rates
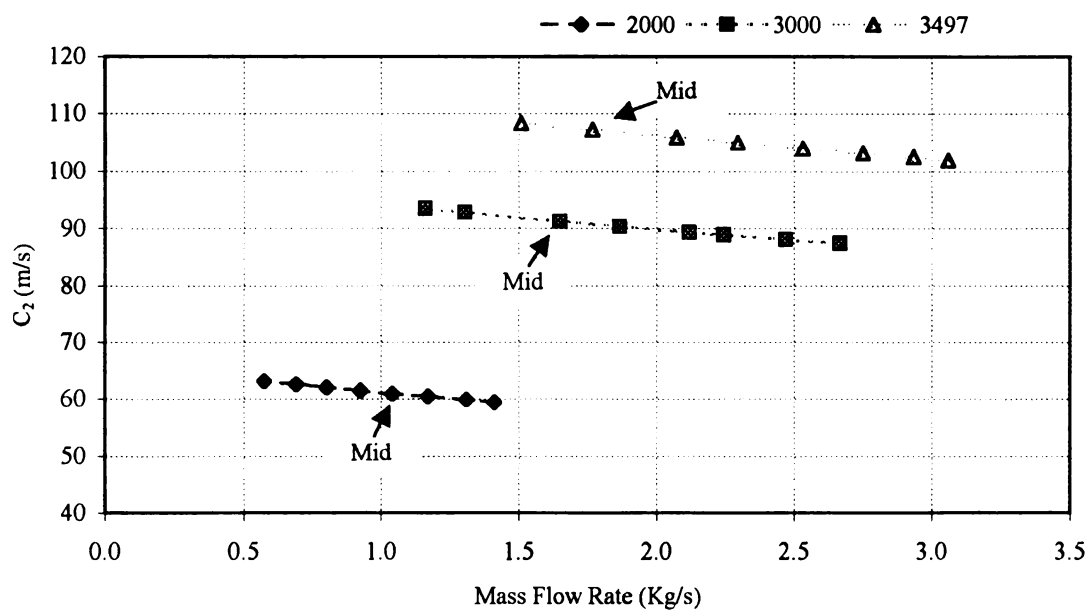
Figure 4.27: Impeller Exit Absolute Velocity For Different Speed and Mass Flow Rates
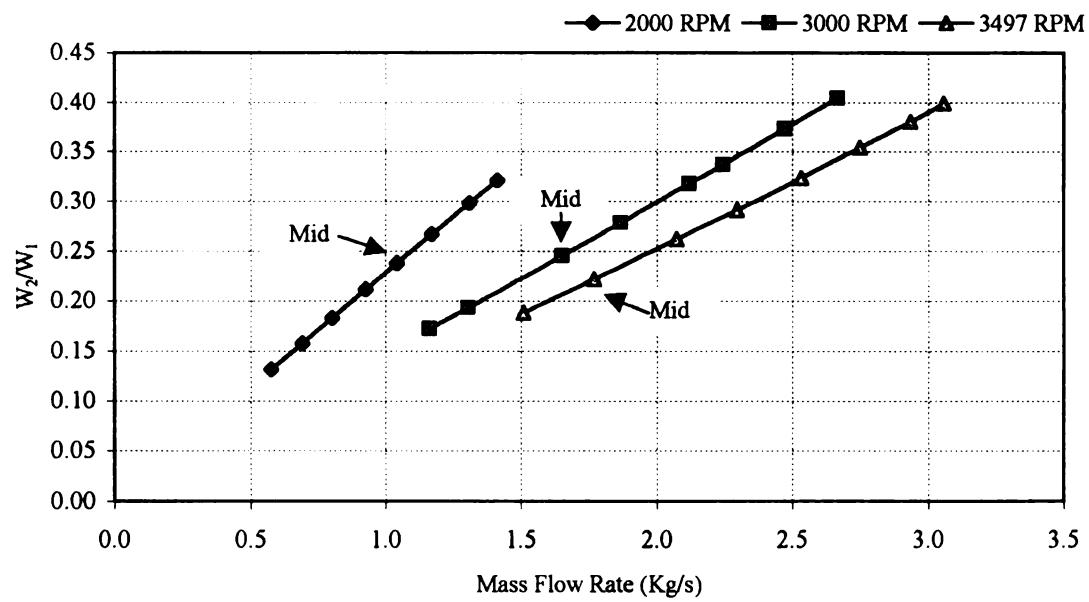
Figure 4.28: Relative Velocity Ratio For Different Speeds and Mass Flow Rates

CHAPTER 5

NUMERICAL ANAYSIS SETUP

In this chapter, various approaches in performing numerical analysis for this investigation are discussed. Advantages and disadvantages of each approach were described in detail. Later in the chapter, the numerical setup of this investigation was presented step by step. The author was not permitted to present the detail of the geometry graphically because of the confidentiality agreement with Trane Company; however, the final grid for the complete flow passage is presented as the conclusion of this chapter.

5.1 INTRODUCTION

With recent software development, Computational Fluid Dynamics (CFD) has become more reliable in flow analysis in fluid mechanics and aerodynamics. In thermo-fluid research area, CFD predictions have been utilized for analysis because of their reasonable accuracy. However, there are still cases such as turbulence modeling and industrial applications, which challenge this tool. There are ongoing developments in simulating the flow structures inside turbomachines utilizing commercial and in-house codes and the results are comparable up to certain accuracy. In blade design, either axial or radial, CFD is becoming very reliable tool, however, researchers have not been able to model the losses properly utilizing this tool.

Recent research areas are based on how to polish the physics and optimization of designs such as blade cooling and passage configuration. Generally, the overall size and geometry of turbomachines are large and complicated in comparison to the benchmark problems that have been solved to approve the credibility of the CFD analysis.

Simulation of the volute flow in centrifugal compressors is still a major challenge for CFD vendors because of the complexity of the flow path topology.

In addition, current commercial solvers utilize various turbulence models, which have their own arguments as to how accurately they can predict a three-dimensional and highly rotational volute flow. Often because of the size of the geometry and to avoid memory expenses, there are simplifications made to the geometry and meshing schemes, which reduce the accuracy in flow prediction. Therefore, the results are reliable only for qualitative flow structure.

Most of the turbomachinery companies have developed in-house solvers, in which inviscid theory for flow analysis and empirical correlation for loss mechanism inside the volute are utilized. This approach reduces the cost of the simulations and the design analysis is obtained in a shorter time than solving the full Navier-Stokes equations. This will enable the designers to perform optimization analysis of their designs in a shorter time and make the development process cheaper. However, these approaches cannot be sophisticated tools for various configurations because they can vary from case to case and geometry to geometry.

Despite all the facts mentioned above, CFD can still be a supplement to experimental analysis. CFD can provide reasonable insight to the problem despite its reduced accuracy. With the current developments, CFD have found its place among the designers and researchers and increased their analysis capabilities extensively. However, complete replacement of expensive experiments by CFD analysis is still questionable and to be answered in future.

5.2 CONSIDERATIONS FOR THE NUMERICAL ANALYSIS

In this investigation, initially CFX-TASCFLOW solver, which is designed for turbomachinery applications, was going to be utilized for the numerical analysis. This solver is a structured based solver and specifically designed for turbomachinery applications. Anormous amount of work is facing the designer to generate grid for a complex topology such as volutes. However, in different cases this solver has presented reasonable results for the impeller geometries and predicted these flows more accurately than the other vendors.

There are ongoing developments in CFD grid generators and solvers for flow inside the volute geometry. A code has been developed at MSU that generates grid for all types of volutes with certain modifications, Gu (2000). In this code instead of generating grid for the complete volute volume, it is broken up to 40 cross section profiles, which are connected to each other linearly. Utilizing the butterfly technique, planar grid is generated for each profile and a volume mesh is generated utilizing linear interpolation consequently. The butterfly technique improves the quality of the mesh and increases the convergence rate of the simulation iterations. Note that this technique is popular among TASCFLOW users because it is the only way to generate structured grid for such geometries. In addition, it has been proven that the simulation converges faster for a structured mesh and the post-processing would be much easier than the unstructured grid. Meanwhile, for the same accuracy in results, the number of required structured mesh is less than unstructured one. Therefore, there is a significant advantage of using the structured grid in reducing the cost of the numerical simulations.

Profile technique requires some simplifications in the geometry especially in the tongue region. The configuration of the tongue region in the Trane compressor, forces the flow to reenter the scroll partially. Because of incompatibility of the cross sections in this region with the rest of the volute geometry, the profile technique cannot be successful in predicting the reentry flow. Thus, by ignoring this region the designer has to compromise portion of the geometry in order to have structured grid inside the volute. In addition, if the curvature radius of the volute casing is small, then a line replaces the curvature and its length depends on the number of the cross sections in the volute volume. Therefore, this meshing scheme and CFX-TASCFLOW solver cannot handle many industrial problems and for the same reasons vendors created unstructured solvers. FLUENT Corporation performed this conversion in order to adapt itself to the variety of the industrial applications.

In this investigation there was another reason for the choice of the commercial CFD software and that was the rotating frame in the turbomachinery applications. CFX-FLOW has shown very good performance in simulating the flow inside rotating impeller passages. However, since the volute casing is stationary, this simulation could be performed almost with any solver. The only limitation was if the grid generator could handle grid generation of this volute.

However, many researchers believe that in order to have more accurate simulation results in centrifugal compressor flows, one must perform the simulation for the complete stage in order to include the interaction between the impeller and diffuser. To do such an analysis, it requires strong computation wealth, which is not available extensively in academic level.

In all grid generation techniques, the first requirement is to have the CAD drawing or profiles of the volute geometry. Since the CVHF 1280 compressor was one of the older Trane designs, the only available geometry information was an AutoCAD file, which was drawn for casting purposes. It was possible to extract profiles geometry out of the CAD file but the information had to be transformed to a group of coordinates for every cross-section and that required an AutoCAD professional. In addition, cross-sections of the vaneless diffuser geometry at the same angles as the volutes had to be extracted in order to complete the flow path.

Having studied FLUENT 5.0 capabilities and the geometry, it was decided to utilize this software for numerical analysis portion of this investigation. Although FLUENT 5.0 is capable of reading grid files from various grid generator software GAMBIT, the default grid generator for FLUENT 5.0, was utilized to generate mesh for this geometry. Note that this simulation has been the first successful attempt in utilizing FLUENT for such geometry among other FLUENT's applications, to the best knowledge of the author.

5.3 GEOMETRY AND GRID GENERATION PHASE

5.3.1 GAMBIT

GAMBIT is a single, integrated preprocessor for CFD analysis. It has ACIS solid modeling capabilities, which enable the user to import CAD solid model files directly. It has the capability of reading IGES CAD format, which has only the information of the vertices and surfaces. GAMBIT enables the user to cleanup and modify the geometry for grid generation purposes. This software can generate mesh for all FLUENT solvers

including FIDAP and POLYFLOW. It enables the user to generate a grid in structured and unstructured hexahedral, tetrahedral, pyramid, and prisms and assign boundary zones to the grid.

GAMBIT provides a strong set of solid modeling-based geometry tools. Top down geometry construction using 3D primitives allows user to create geometries fast, without the complexity of a full-fledged CAD package. Different CFD problems require different mesh types, and GAMBIT gives user all the options needed for these applications. Meshing toolkit in GAMBIT lets user decompose geometries for structured hex meshing or perform automated hex meshing with control over clustering. Triangular surface meshes and tetrahedral volume meshes can be created within a single environment, along with pyramids and prisms for hybrid meshing.

5.3.2 TRANE VOLUTE GRID

As mentioned previously, Trane Company provided the AutoCAD file of the volute casing design, which was in solid model format (ACIS). This file included a solid volume of the volute that showed the casing with its wall thickness, oil passages and holes for bolting the flanges on the compressor casing. Note that in the first attempt, an IGES format, which had the surfaces information, was utilized but the universities UNIX workstations were not capable of handling the large size of these files.

After importing the ACIS file, the volume was deleted and only the inner shell of the volute was kept (Figure 5.2). In the next step, the vaneless diffuser was generated in the same volute file. An attempt was made to attach both geometries but it was not

possible due to the geometry mismatch at the interface of the two (Figure 3.4). After studying GAMBIT capabilities, the vaneless diffuser and volute volumes were generated and meshed in two separate files. Later in Fluent, the non-conformal meshing technique was utilized to attach the two meshes in a single file.

In order to create the volume mesh, the geometry must be a closed area in order to be recognized by GAMBIT as a volume. Therefore, the volute shell had to be covered by an interface surface between volute and the vaneless diffuser exit. Having the dimensions of the vaneless diffuser (Figure 3.4), it was created in a separate file and the outlet face was mapped over the volute shell in order to create the required interface. Note that in the tongue region, the diffuser outlet was blocked by a portion of the casing wall, which created a passage between the tongue and beginning of the scroll. At the same time, the outer flanges of the diffuser and volute were offset. Hence, considerations were applied to accommodate the mismatch. These details were challenging at every step, however they contributed to a more accurate flow diagnosis.

In defining the volute volume, it was found that since the scroll surface of the volute was defined in multiple long spiral pieces, GAMBIT was unable to recognize the surfaces after closing the volume. It was recommended that all long surfaces be broken into small surfaces in the original CAD file, which meant that the volute had to be redrawn. Having that modification, GAMBIT would have been able to generate an structured mesh for the volute.

In order to avoid additional work for an older design, it was decided to continue with the same file and create an unstructured grid for the volute. Having tried various

ways to resolve the volume recognition in GAMBIT, it was found that by generating the grid on the surface prior to defining the volume, GAMBIT could recognize the volute volume. This was due to the fact grid nodes on the surfaces would define more coordinates over the curved and spiral surfaces and function in a similar way if the surfaces had been redefined in pieces.

The configuration of the spiral surfaces in few pieces was a disadvantage to the quality of the grid. Hence, by using the virtual geometry in GAMBIT, those surfaces were merged into cleaner surfaces. Though, virtual geometry would increase the level of difficulty of attaching the surfaces and defining the volume. In addition, generating the grid on the long virtual surfaces wouldn't allow any Boolean operation between the surfaces. Once the grid was generated, changing the parameters was not possible and forced GAMBIT not to recognize the volume. Therefore, certain precautions had to be considered in merging the surfaces in order to avoid volume recognition problem.

Having the above as obstacles, the volute volume was generated with all surfaces and solid edges. Note that in this study the only geometry simplification was the step at the connecting flanges of the two volumes, which was modified to an inclined connection. The height of that step was 0.182 inch, which was very small in comparison to the overall size of the volute. Other than that, there was no other simplification in the geometry and entire the casing art effects were included in the domain as far as the accuracy of the drawing software would permit.

The first tetrahedral grid meshes were generated for both diffuser and volute with 1 inch spacing. After the first simulation, it was found that finer grid would provide

better convergence rate. Meanwhile, at some areas such as tongue region, the initial size of the mesh was not sufficient to cover the flow path. Therefore, a second grid set was generated with 0.25 inch grid spacing, which converged the simulation faster than the initial grid.

Upon creating totally 140,000 grid nodes for volute and diffuser in two separate files (Figures 5.4-5), boundary zones were defined in order to extract data over any desired surface in post-processing phase. There were multiple ways to merge the two grid files into one. In this study "TGRID", which is one of the FLUENT's older grid generator software, was utilized to do so. However, the diffuser and volute interfaces were assigned "Interface" zone prior to merging the files in order to be recognized in non-conformal technique.

5.4 SIMULATION PHASE

5.4.1 FLUENT

FLUENT provides a wide variety of physical models for turbulence, combustion, and multiphase applications. The fully unstructured mesh-based technology in FLUENT 5.0 has proven over time by multiple validations in benchmark problems. FLUENT turbulence models include simple k-ϵ modeling to second-moment closure Reynolds stress models and large eddy simulation. Species transport and chemical reaction models with materials and reaction database are available as well.

Mesh quality can be the primary factor in CFD solution accuracy. FLUENT lets the user improve the mesh as part of the solution process by examining the preliminary

solution using FLUENT tools for solution-based mesh adaptation to get a more accurate result. A set of solver algorithms are existing in FLUENT, which is tuned to specific problem physics, such as advanced coupled solvers for compressible and incompressible flows, and segregated solvers for the complicated numerical tasks.

Parallel processing is the key to fast turnaround of CFD calculations. FLUENT has the capability of parallel computing, with all the interactive tools one needs. By taking advantage of the user-defined functions capability in FLUENT, user can create a custom version of the software that suits his/her needs. This flexible capability lets user specify volumetric sources, reaction rates, custom physical properties, boundary conditions, scattering phase functions for radiation modeling, and body force, drag, and source terms for discrete phase modeling. One can also create custom post-processing variables and define own scalar transport equations.

5.4.2 GOVERNING EQUATIONS IN FLUENT

There are various governing equations available in FLUENT that depending on the flow regimes any of them can be selected. In this investigation the flow regime is turbulent and the momentum equation should be companied with a turbulence model. As was stated previously there are various models available, however, the simplest one (k-ε) was selected to perform this simulation.

The governing equations in this model in mean form are as following

Conservation of mass:

$$\frac{\partial \rho}{\partial t} + \frac{\partial}{\partial x_j}(\rho\, u_j) = 0 \qquad (5.1)$$

Momentum:

$$\frac{\partial}{\partial t}(\rho\, u_i) + \frac{\partial}{\partial x_j}(\rho u_j u_i) = -\frac{\partial P}{\partial x_i} + \frac{\partial}{\partial x_j}\left\{\mu_{eff}\left(\frac{\partial u_i}{\partial x_j} + \frac{\partial u_j}{\partial x_i}\right)\right\} \qquad (5.2)$$

Where: $\qquad\qquad\qquad \mu_{eff} = \mu + \mu_t$

The turbulent (eddy) viscosity term is defined based on the (k-ε) model:

$$\mu_t = \rho\, c_\mu \frac{k^2}{\varepsilon} \qquad (5.3)$$

where ε is the dissipation rate of the k, turbulent kinetic energy. The amount of k per mass and time converted into the internal energy of the fluid by viscous action. C_μ is the model constant which is equal to 0.09.

Local values of k and ε are obtained from the solution of the following semi-empirical transport equations:

$$\frac{\partial(\rho\, k)}{\partial t} + \frac{\partial(\rho\, u_j k)}{\partial x_j} = \frac{\partial}{\partial x_j}\left(\Gamma_k \frac{\partial k}{\partial x_j}\right) + P_k - \rho\varepsilon$$

$$\frac{\partial(\rho\varepsilon)}{\partial t} + \frac{\partial(\rho u_j \varepsilon)}{\partial x_j} = \frac{\partial}{\partial x_j}\left(\Gamma_\varepsilon \frac{\partial\varepsilon}{\partial x_j}\right) + \frac{\varepsilon}{k}\left(c_{\varepsilon 1}P_k - \rho c_{\varepsilon 2}\varepsilon\right) \qquad (5.4)$$

where the diffusion coefficients are given by,

$$\Gamma_k = \mu + \frac{\mu_t}{\sigma_k}$$

$$\Gamma_\varepsilon = \mu + \frac{\mu_t}{\sigma_\varepsilon}$$

(5.5)

The production rate of turbulent kinetic energy P_k is given by

$$P_k = \mu \left(\frac{\partial u_i}{\partial x_j} + \frac{\partial u_j}{\partial x_i} \right) \frac{\partial u_i}{\partial x_j}$$

(5.6)

and the model constants are given

$$c_{\varepsilon 1} = 1.44$$
$$c_{\varepsilon 2} = 1.92$$
$$\sigma_k = 1.0$$
$$\sigma_\varepsilon = 1.3$$

(5.7)

In this investigation for simplicity, the standard k-ε model with wall function was utilized as the turbulence model. The k-ε default constants were used, however, they can be modified with in FLUENT. The simulations were performed for steady state condition, in which the transient terms of the governing equations were eliminated. The convergence criterion was chosen 1E-4 for the residual and default algorithms were utilized for discretization of the governing equations. The default schemes are first order upwind for momentum and turbulence kinetic energy and SIMPLE for pressure-velocity coupling.

5.3.3 VOLUTE FLOW SIMULATION

The grid generated in GAMBIT was imported into FLUENT 5.0. The boundary conditions and materials had to be defined prior to the simulation. There are various ways of defining boundary conditions for a simulation in FLUENT. For momentum boundary conditions, total and static pressures, mass flow rate at the inlet and outlet are among the choices. The boundary surfaces are named after the type of condition provided there, such as "Pressure Inlet" or "Inlet Mass Flow". Depending on the additional equations engaged in the simulation, such as energy equation, one could define the corresponding variables at the boundaries. If the momentum equation is companied with energy equation, flow temperatures must be provided in addition to the momentum boundary conditions.

Initially in the simulation, the energy equation was employed and in the material section, air with ideal gas status was chosen as the working fluid. This choice would let the density of the air vary with the pressure and temperature along the flow path. However, experimental results showed later that the compressor has low pressure ratio and flow at the impeller exit has low Mach numbers. Therefore, the assumption of constant density would suit the flow simulation from impeller exit to the conic outlet. Meanwhile, the previous temperature measurements were not reliable for boundary conditions because of the thermal stability of the compressor as was described in previous chapters. Hence, it was decided to eliminate the energy equation and perform only momentum simulation.

To define the momentum boundary conditions, the combination of "Inlet Mass Flow Rate" and "Static Pressure" at the outlet was considered initially but the flow angle at the diffuser inlet would have been neglected. Therefore, velocity magnitude and flow angles with respect to radial direction at the vaneless diffuser inlet, which were calculated from the impeller meanline analysis, were provided as the inlet condition. This boundary condition included both the mass flow rate information and flow angles at this face.

As mentioned in the introduction section of the chapter, if the simulations were performed for the stage, the velocity and flow angle distributions could have been extracted at the vaneless diffuser inlet. Circumferential and axial variation of the velocity vectors and flow angles at this face, would have determined the interaction of the impeller and the vaneless diffuser. However, the results in the next chapter shows that assigning uniform velocity and flow angle distribution in this region has provided reasonable performance results for these components.

In the case of simulation without the impeller, the best inlet boundary condition was to measure velocity magnitudes and flow angles at different circumferential and axial locations at the vaneless diffuser inlet, Ayder (1991). A profile that included circumferential and axial velocity distribution could be provided in FLUENT. For the future investigations on this compressor, the Cobra probes are utilized to perform these measurements.

For the conic outlet, the experimental measurements of static pressure were provided as the boundary condition. FLUENT provides the option of correction of the

flow at the outlet with respect to the upstream condition. This means that if the flow upstream becomes supersonic or separated, the outlet flow properties would be extrapolated from the results upstream.

In addition to definition of the working fluid, the wall material had to be defined in order to include the effect of surface roughness. In the initial simulation smooth wall was chosen for the volute casing and after validation of results, the next simulations were performed with the same smooth wall material.

FIGURES
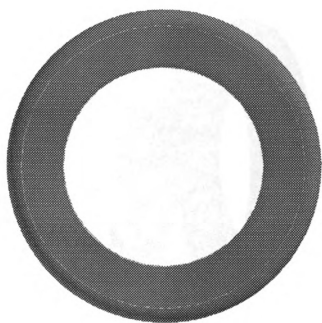
Figure 5.1: Vaneless Diffuser
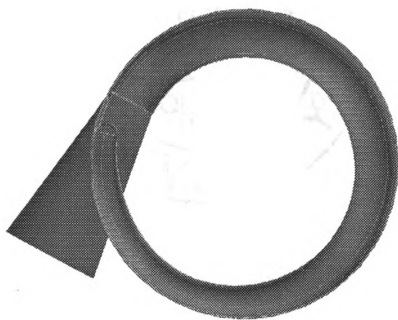
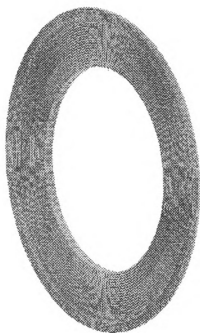
Figure 5.2: Volute Casing
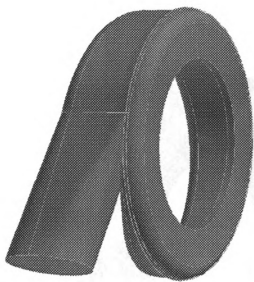
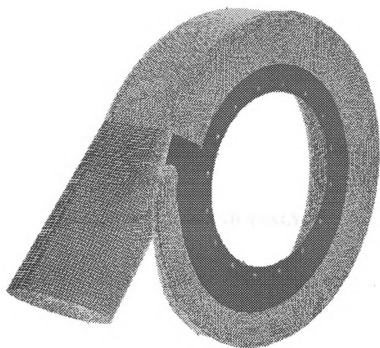Figure 5.3: Complete Flow Path

Figure 5.4: Diffuser Grid

Figure 5.5: Volute Mesh

CHAPTER 6

NUMERICAL RESULTS AND ANALYSIS

.

In this chapter, the simulation results are validated by comparing them to the experimental results. In addition, performance, flow structures, and loss mechanisms for the vaneless diffuser and volute are discussed in detail.

6.1 VALIDATION

The simulations were validated by comparing the overall properties in the simulation to those in the experiments results. The properties obtained experimentally were averaged circumferentially (vaneless diffuser) and axially (volute) at every desired cross section of the flow. The properties obtained numerically were mass averaged over the cross section, which is a popular technique among numerical analysts because of its accuracy.

As mentioned in the previous chapter, the boundary condition at the diffuser inlet includes the velocity magnitude and flow angle extracted from the meanline analysis. Figure 6.1, compares the diffuser inlet static pressure for different speeds and maximum mass flow rates obtained from experiments and CFD analysis. Note that static pressure was not the boundary condition at this cross section and could vary from the impeller meanline analysis. There is an offset between the two static pressures, which propagates in the next results as well, Figures (6.2-3). Without including impeller flow in the simulation, CFD cannot predict accurately the boundary layer development at the beginning of the vaneless diffuser. The development of the boundary layer on vaneless diffuser walls increases the entrance speeds and reduces the static pressure at the diffuser inlet. In order to prevent this situation, the measured mass flow rate at the vaneless diffuser entrance could be utilized as the boundary condition for each case. Simulations

146

had to be repeated with different flow angles until the CFD and experimental static pressures at this face were matched. This matching between the two values concludes the most accurate flow angle for the flow at the vaneless diffuser inlet. Another alternative would have been to provide experimental values for the flow angles and speeds at the vaneless diffuse inlet, which were described in the previous chapter. However, with the provided boundary conditions, the CFD and experimental results are in good agreement. The minimum and maximum offset for results in Figures (6.1-3) are 0.35% and 2.4%, which are reasonable.

Figures 6.2-3 compare the diffuser outlet static and total pressures at different speeds and maximum flow rate. The CFD prediction has a small offset and follows the same trend as the experimental results. As rotational speed increases, both static and total pressures at vaneless diffuser exit increase. Note that similar results for different mass flow rates were available, however, for validation purposes maximum, minimum, and intermediate mass flow rates were selected.

Figures 6.4 through 6.12 present the volute static pressure distribution at different volute cross-sections where the static probes are located in the experiments (Figure 4.1). These results show the behavior of the volute at different speeds and mass flow rates. Numerical simulations predict the initial diffusion at the beginning of the scroll with the same trend and rate of the experimental results. They confirm the near uniformity of this pressure distribution downstream of the scroll, however, there are also diffusion patterns in this region for all cases.

In all cases the experimental and numerical results are in good agreement with each other, which indicates the validity of the simulations.

6.2 PERFORMANCE

Figures 6.13-14 show the static pressure recovery and loss coefficients (2.37-38) for the vaneless diffuser. Clearly the vaneless diffuser raises the static pressure more in higher mass flow rates and speed. Losses in the vaneless diffuser decrease as the mass flow increases because the flow obtains the momentum to overcome the adverse pressure gradient. The largest losses in the vaneless diffuser occurred at low mass flow rates and 2000 RPM due to the flow separation in this component.

Figures 6.15-16 show the static pressure recovery and loss coefficients for the volute and cone. This plot presents the overall performance of these two components together. The static pressure recovery of the volute and cone decreases with increase in the mass flow rate and speed. Generally at off design condition, flow is decelerated inside the volute, resulting in a slight pressure rise inside the volute. However, larger mass flow rates in the volute reduce the diffusion inside this component. The conic diffuser transforms the kinetic energy left in the flow to pressure regardless of the volute performance, unless the flow separates inside this component. Figure 6.16 shows that the loss at 3000 RPM decreases with increasing in mass flow rate while the 3497 RPM remains almost constant in that flow range. 2000 RPM and minimum mass flow rate has the maximum loss, which indicates worst operating condition of the compressor.

The radial component of the velocity at the vaneless diffuser outlet generates a strong rotational flow in smaller areas of the volute, which is in the form of a forced vortex flow. Further downstream, fresh fluid wraps around this rotational flow and as the volute area increases a counter vortex is generated, as was described in Chapter 2. Figures 6.17-20 show the average vorticity magnitudes at the volute cross-sections for

2000, 3000, 3497 RPM and maximum, medium and minimum mass flow rates. In all cases, high vorticity levels are observed at the beginning of the scroll and stay at a constant level further down stream. The primary observation is that the trend is independent of the mass flow rates and speeds. Further in the chapter the flow structure will describe the reasons for this tendency. Note that in all case, the minimum mass flow rates are generating slightly different vorticity distribution in upstream of the volute due to the strength of the initial vortex flow. In lower mass flow rates, the radial velocity component at diffuser outlet is smaller than higher mass flow rates; therefore, the vortex flow is weaker. Figure 6.20 presents a comparison of the same flow property for different speeds at maximum mass flow rate. There is a decrease in vorticity at 2000 RPM due to smaller radial velocities the volute inlet as compared with the other two speeds

Figures 6.21-23 show the tangential velocity distribution inside the volute for different speeds at varying mass flow rates. It was observed that the flow goes through acceleration and deceleration in the smaller cross sections and minimum mass flow rates. In higher mass flow rates, diffusion decelerates the flow inside the volute and the tangential velocity decreases. The tangential velocities decrease more when the flow arrives inside the conic diffuser because of the larger diffusion rate in this component. Note that in 2000 RPM cases, the flow decelerates so much that might not be able to recover from the adverse pressure inside the volute. Therefore, boundary layer on the volute walls may become separated and reversed flow occurs. In addition, the convex surface of the inner wall of the volute could contribute to this phenomenon as well. Figure 6.24 compares the tangential velocity distribution for three speeds and maximum flow rates.

6.3 FLOW STRUCTURE

6.3.1 VANELESS DIFFUSER FLOW

Figures 6.25-33 present the static and total pressure contours and meridional velocity vectors in the volute cross-sections at 27, 117, 207 and 297 degrees for 3497, 3000 and 2000 RPM and varying mass flow rates.

At the diffuser inlet, the static pressure is constant over the diffuser width because the boundary condition at this face is uniform absolute velocity and angle. The static pressure increases radially towards the diffuser exit. The 90 degree bend on the hub wall affects the upstream flow and results in separated flow on this wall. Decrease in mass flow rate, decreases the radial component of the velocity inside the vaneless diffuser, which reduces the momentum of the flow to overcome the existing adverse pressure. In 2000 RPM and minimum mass flow rate, the radial component of the velocity is so small that the separated regions cover the whole wall. This due to the fact that the flow angles at this condition is very large and it is predicted that the diffuser stalls.

If the impeller were included in the simulation, the mixing region between the impeller and the vaneless diffuser would wash out the nonuniformity of the velocity profile of the flow leaving the impeller. Therefore, considering a uniform velocity distribution at the vaneless diffuser inlet was not far from reality. In addition, more flow exits the impeller on the shroud side in lower mass flow rates, while more flow exits from the hub side of the impeller at higher mass flow rates. This is due to the nature of the centrifugal flow, which forces inevitable secondary flows inside the impeller passages. Thus, this lack of momentum on the hub wall would have been superimposed on the current simulation results.

The contours of the total pressures confirm the flow separation on the hub wall as well. In lowest mass flow rate (Figure 6.33), a pattern of an almost returned flow can be observed on the hub wall and the separated region is very close to the impeller. This suggests the possibility of the stall inside the vaneless diffuser. Note that these are steady state results and unsteady simulations would predict oscillation patterns in these regions.

It is concluded that the vaneless diffuser is too large for these mass flow rates and the hub wall has to be pinched in order to prevent this separation. Pinching the diffuser increases the speeds and provides the required momentum to overcome the adverse pressure.

6.3.2 VOLUTE FLOW

In general, the flow from the diffuser is turned from a radial to a horizontal in the 90-degree bend between the diffuser and the volute. The radial component of the velocity entering the volute, initiates a rotating flow inside the volute. The curvature of the volute casing contributes to this flow structure as well. The vortex is initially formed in smaller areas and expands further downstream. Downstream in the volute, a counter vortex is formed in lower pressure region inside the volute, which shows the reason for vorticity magnitude decay in the vorticity plots. Those plots show the resultant vorticity distribution in the cross sections.

The rotational velocity of this vortex flow increases from zero at the center to a higher value radially out. The velocity distribution at the vortex core has linear distribution to some radial distances, thereafter the distribution is affected by the geometry of the volute cross section. Ayder (1993) observed more or less linear

distribution of swirl velocity outside the vortex core for elliptical volute cross section, which indicates that the flow has a solid body rotation regime. However, Hagelstein et al. [23] reported a constant velocity distribution outside the vortex core for a rectangular volute cross section. In this case, the vortex losses primarily occur in the transition region between the frictionless solid body core and the outer shell in which small velocity gradients predominate.

Similar forced vortices are detected in the Trane volute cross sections, however, since the mass flow rates are much lower than the design point, the intensity of these vortices are not as much as the above cases. Therefore, outside core flow is swept away by the through flow, which impacts the velocity distribution. Note that in the 2000 RPM case, the twin vortex is never formed, instead, the single vortex has occupied a large region downstream of the volute. Existence of these vortices results in larger radial velocities at the walls, which increase the friction losses inside the volute. Another important observation is the rotational flow close to the volute hub wall, returns to the vaneless diffuser in case of 2000 RPM and minimum mass flow rate, (Figure 6.33). This is due to the fact that separated flow on the diffuser hub wall created a pressure sink in the flow path, which causes the flow return.

Observing the static pressure contours in Figures 6.25-33 shows that the axial variation of the pressure on the outer casing of the volute is not significant and validates the averaging method utilized in the experimental measurements, described in Chapter 4. As predicted previously, the flow decelerated inside the volute and the expansion of large static pressure areas further downstream indicates the fact. In other words, the compressor is working off design and the volute is too large.

The static pressure variation over the cross section results from swirl and the circumferential curvature of the volute channel. The centrifugal forces due to swirl are in equilibrium with the static pressure increase from center toward the walls:

$$\frac{dP}{dr} = \rho \frac{V_s^2}{r_c}$$

(6.1)

where r_c is the curvature radius of swirling component velocity and r is radial distance from the swirl center. In the Trane volute this happens only in small area cross sections, where the intensity levels are high. In larger area cross sections the intensity of the vorticity decays, therefore, it doesn't impact the static pressure distribution. Thus the through flow velocity and circumferential curvature create a pressure gradient between the inner and outer wall:

$$\frac{dp}{dR} = \rho \frac{V_T^2}{R}$$

(6.2)

which can be observed in the figures. Van den Braembussche et al. (1990) show how the variation of through flow velocity over the cross section results from the static and total pressure distribution:

$$P_0 - P = \frac{\rho}{2}(V_T^2 + V_s^2)$$

(6.3)

At the volute inlet sections both total and static pressures decrease from the volute wall toward the center resulting in a nearly uniform through flow distribution. In Trane volute at the downstream sections and minimum mass flow rates, forced vortex cores are extended resulting in more uniform total pressure distribution. The total pressure contours in Figures 6.25-33 show a strong total pressure gradient zone at small areas of the volute

indicating that the total pressure loss primarily happens in the areas immediately downstream of the tongue.

In addition, the periodic increase and decrease of swirl velocity during rotation around the volute cross section periphery results in extra diffusion and mixing losses. Increased turbulence mixing between the low energy fluid in the boundary layers and the high energy fluid at the center due to the curvature of the walls, and the fact that after each rotation the boundary layer is absorbed by the new fluid coming out of the diffuser, further contribute to a distribution of total pressure losses over the volute cross section. The total pressure over the volute cross section is lower than of the incoming fluid and gradually decreases toward the volute outlet.

Note that the single vortex and twin vortices have moved axially further from the wall in the lowest mass flow rate (Figure 6.33). It can be observed that the strength of these vortices decreased downstream and the center of the rotational flow is carried away from the hub wall to the shroud wall. The low-pressure region in volute has expanded more than the 3497 RPM case, which can contribute to this process as well. However, it is not possible to exactly predict the location of these vortices.

6.3.3 TONGUE EFFECT

Figures 6.34-36 show the static pressure contours on the shroud side of the vaneless diffuser for different speeds and mass flow rates. The tongue region is shown with a radial dashed line to observe its effect on the pressure distribution. In all cases, constant pressure contours are broken up between the tongue and volute beginning, which creates a distortion in the circumferential static pressure distribution. In addition,

this region creates a sharp circumferential static pressure gradient between volute outlet and inlet. Existing of such gradient forces the flow at the volute outlet to "leak" back into the volute. As the flow rate increases, the distortion shrinks due to pressure build up at the tongue because of the blockage effect. On the other hand, overall the intensity of the radial pressure gradient inside the vaneless diffuser increases as the mass flow rate decreases, which leads to the separated flow in this component.
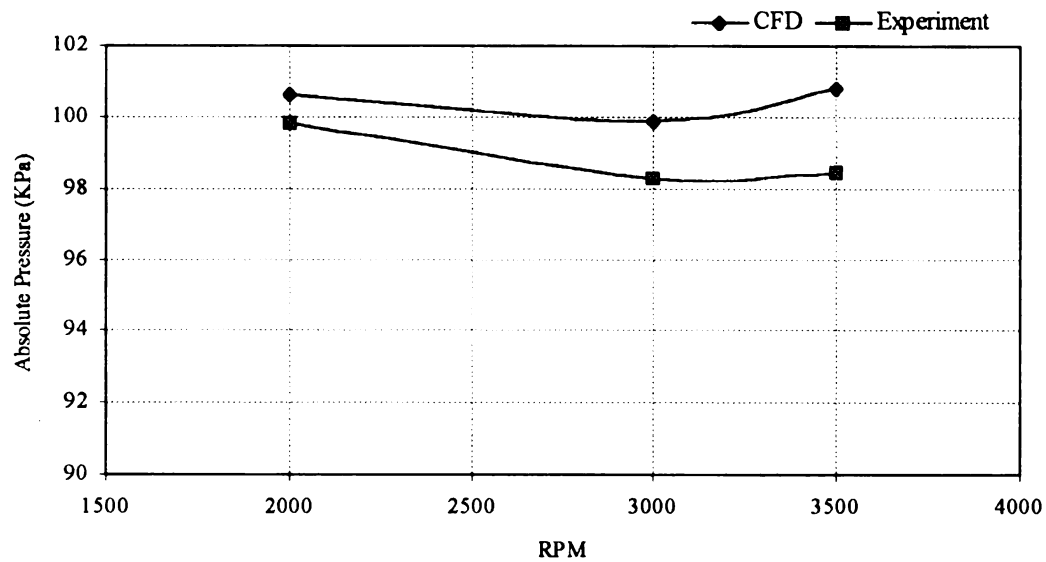
FIGURES

Figure 6.1: Diffuser Inlet Static Pressure at Choke
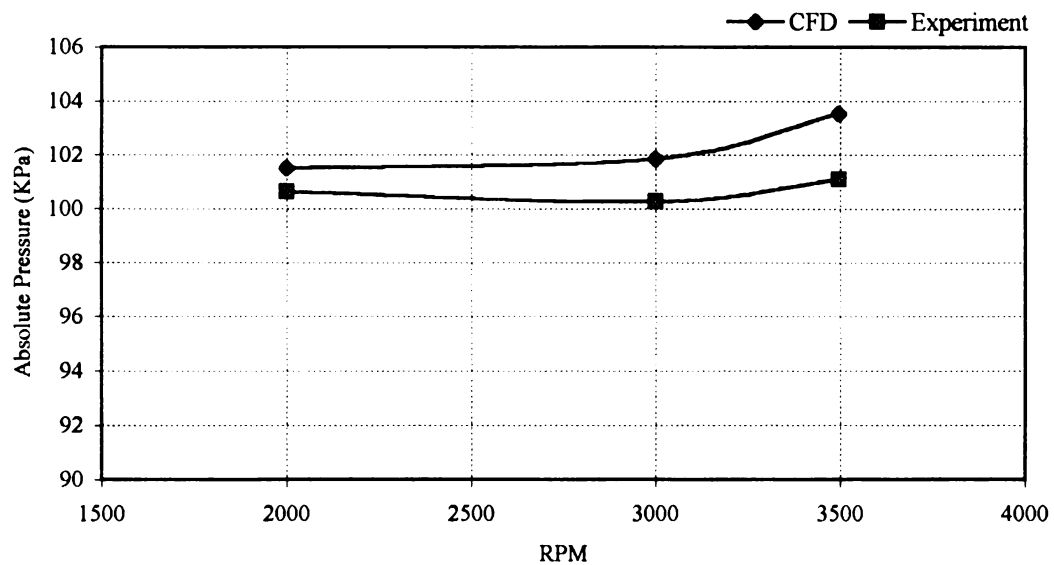
Figure 6.2: Diffuser Outlet Static Pressure at Choke Condition
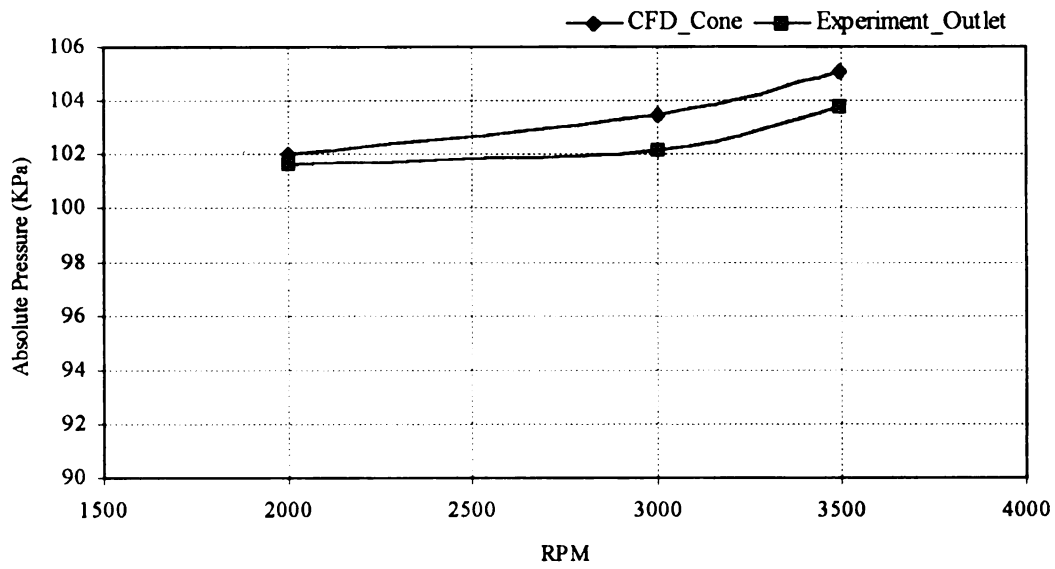
Figure 6.3: Cone outlet Total Pressure at Choke Condition
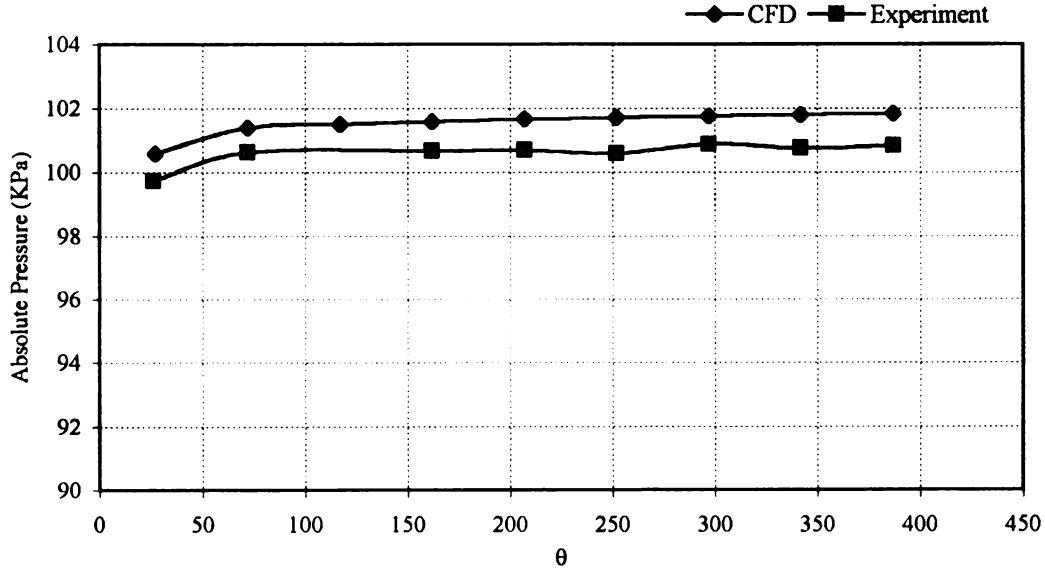
Figure 6.4: Volute Static Pressure Distribution at 2000 RPM and Maximum Flow Rate
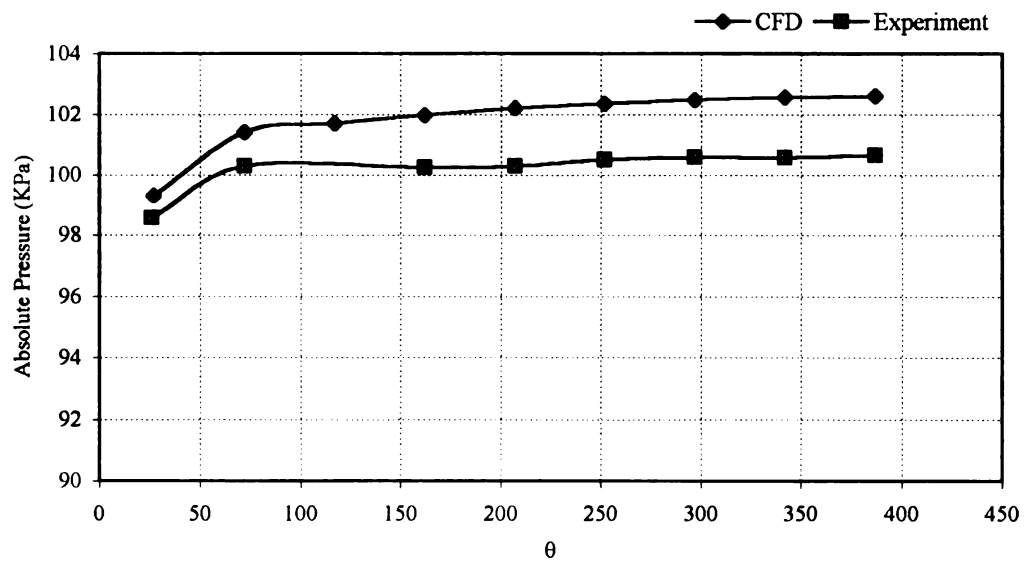
Figure 6.5: Volute Static Pressure Distribution at 3000 RPM and Maximum Flow Rate
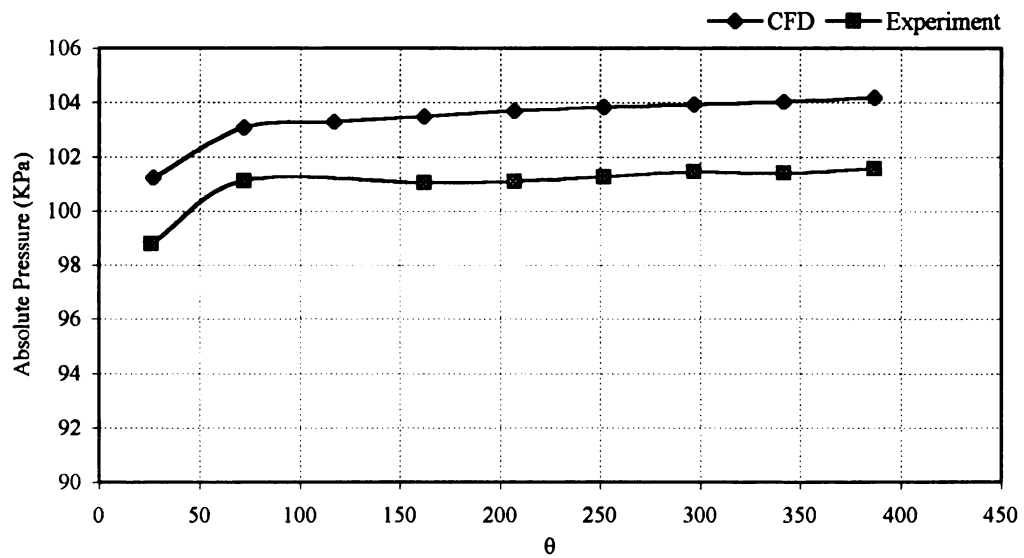
Figure 6.6: Volute Static Pressure at 3497 RPM and Maximum Flow Rate

159
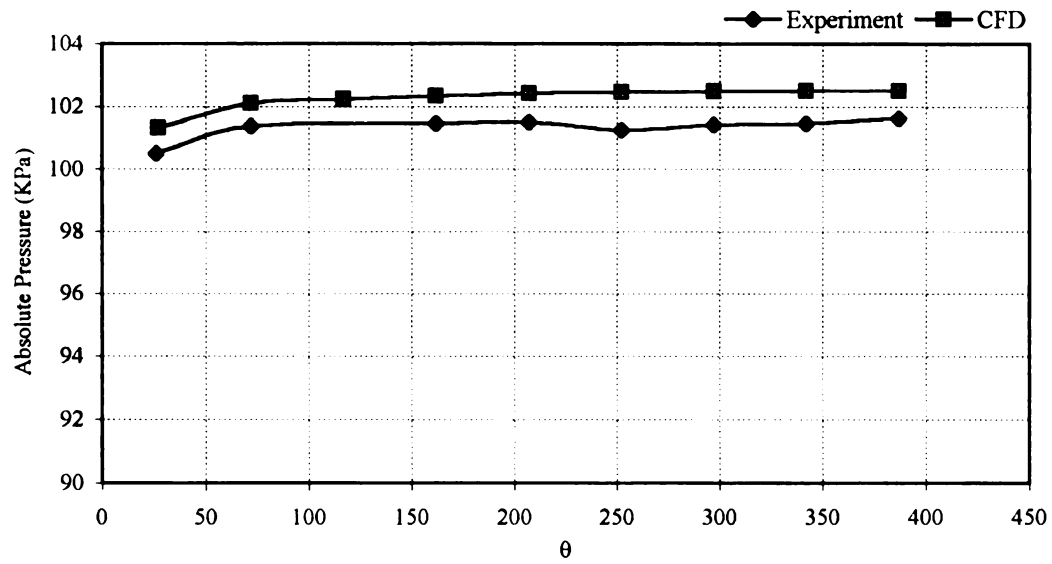
Figure 6.7: Volute Static Pressure Distribution at 2000 RPM and Mid Mass Flow Rate
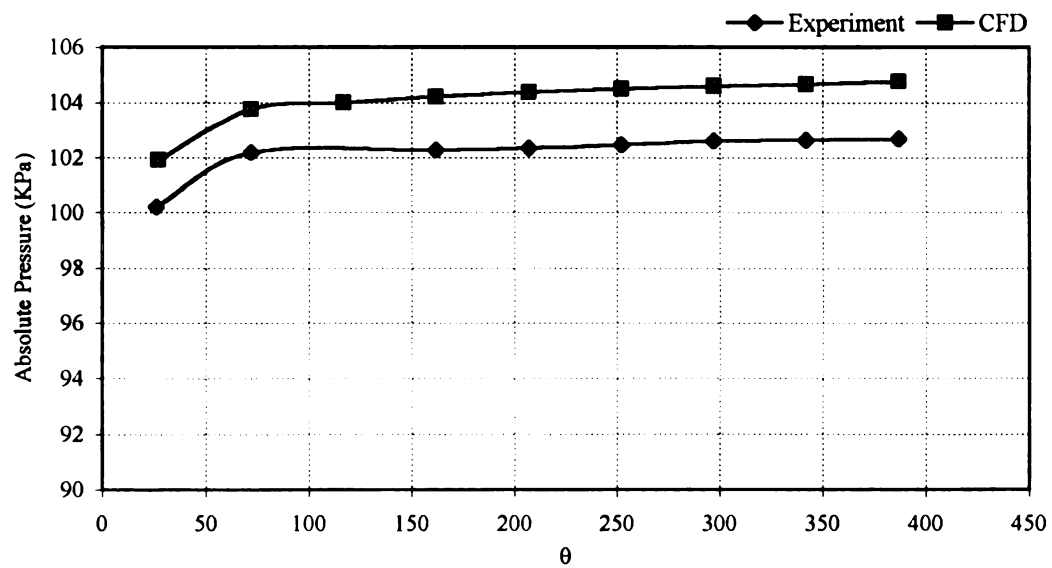
Figure 6.8: Volute Static Pressure Distribution at 3000 RPM and Mid Mass Flow Rate
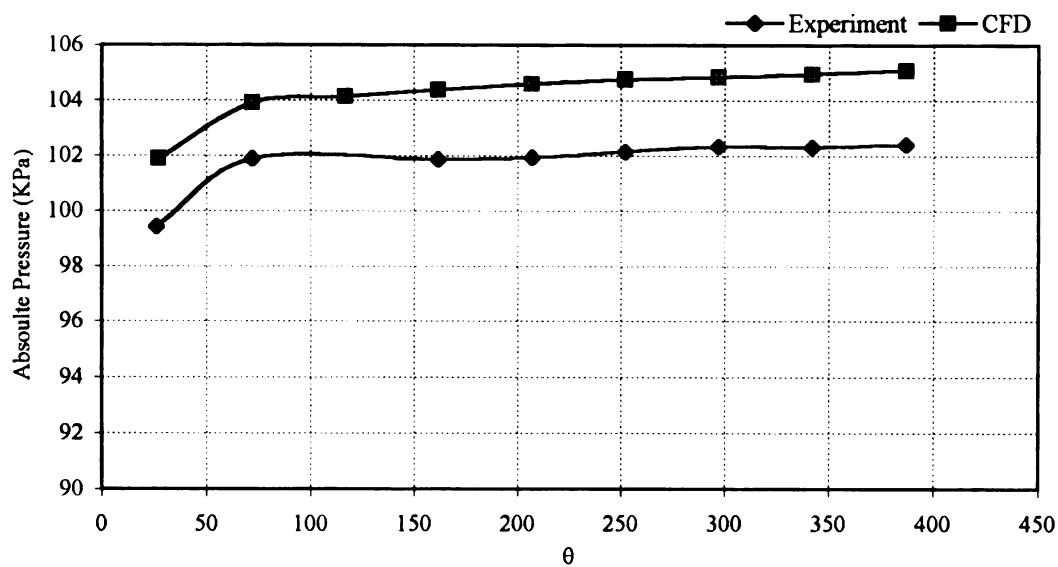
Figure 6.9: Volute Static Pressure Distribution at 3497 RPM and Mid Mass Flow Rate
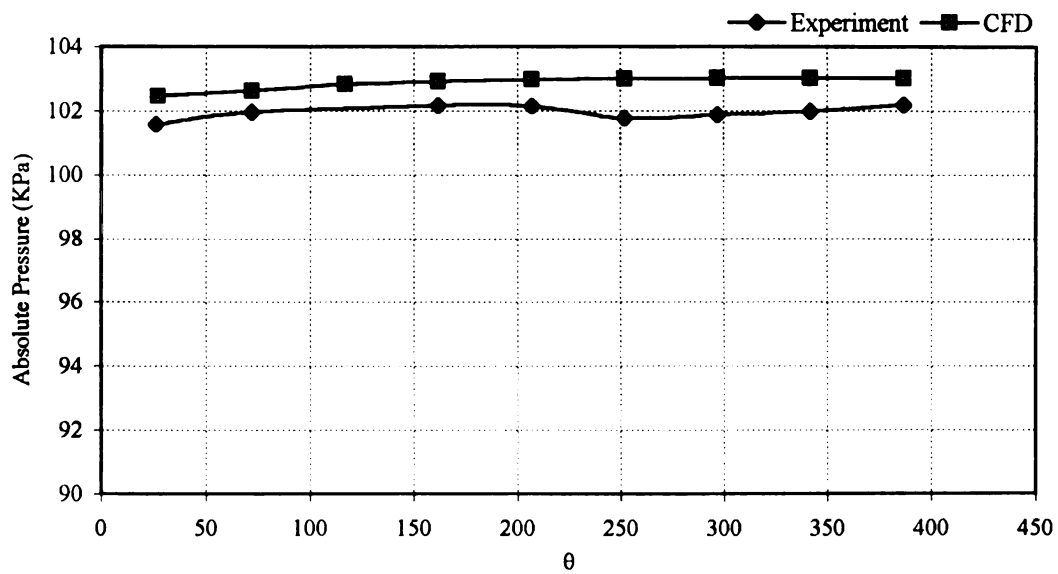
Figure 6.10: Volute Static Pressure Distribution at 2000 RPM and Min Mass Flow Rate
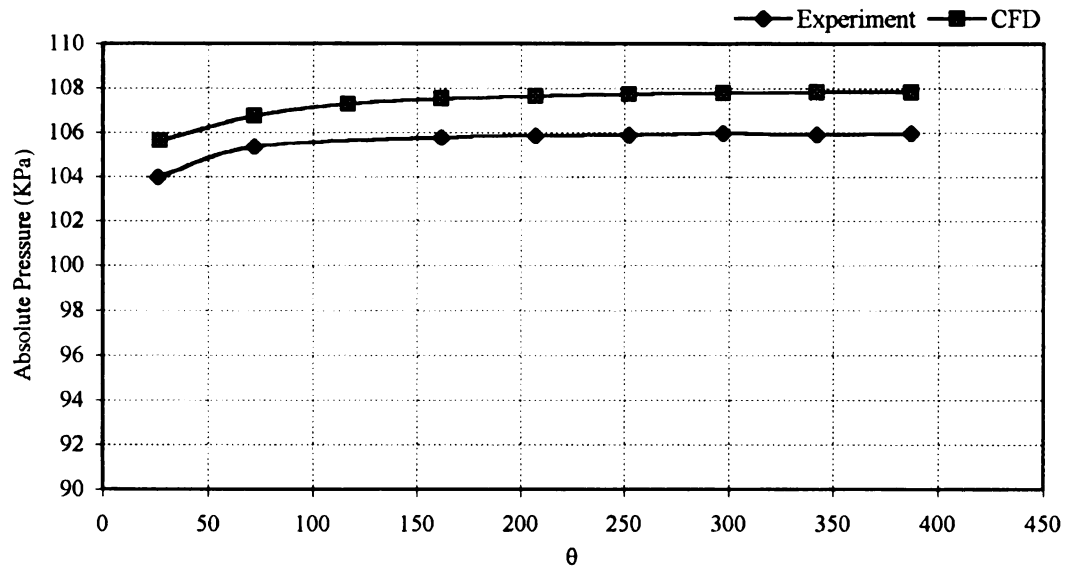
Figure 6.11: Volute Static Pressure Distribution at 3000 RPM and Min Mass Flow Rate
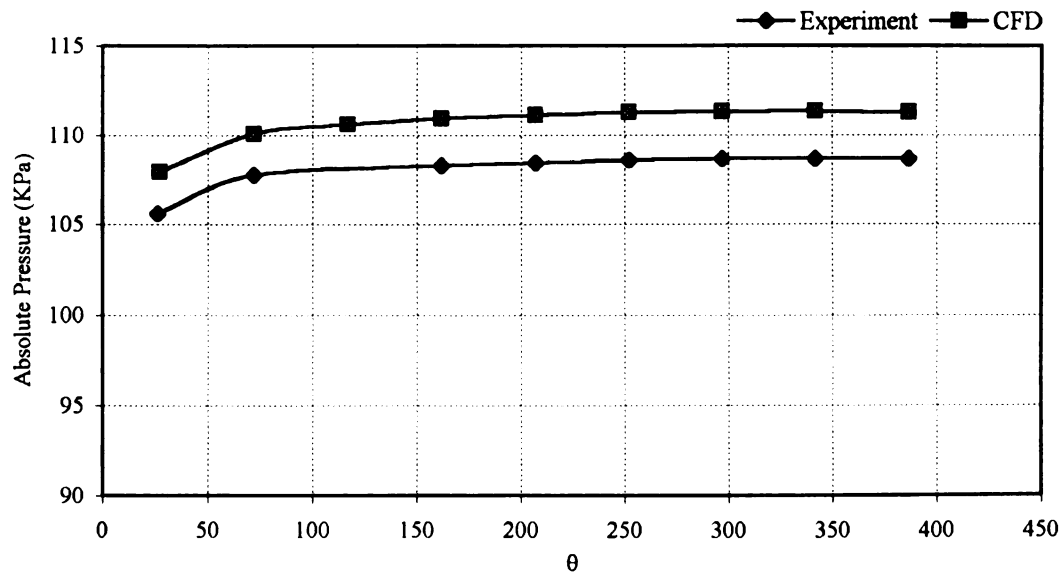
Figure 6.12: Volute Static Pressure Distribution at 3497 RPM and Min Mass Flow Rate
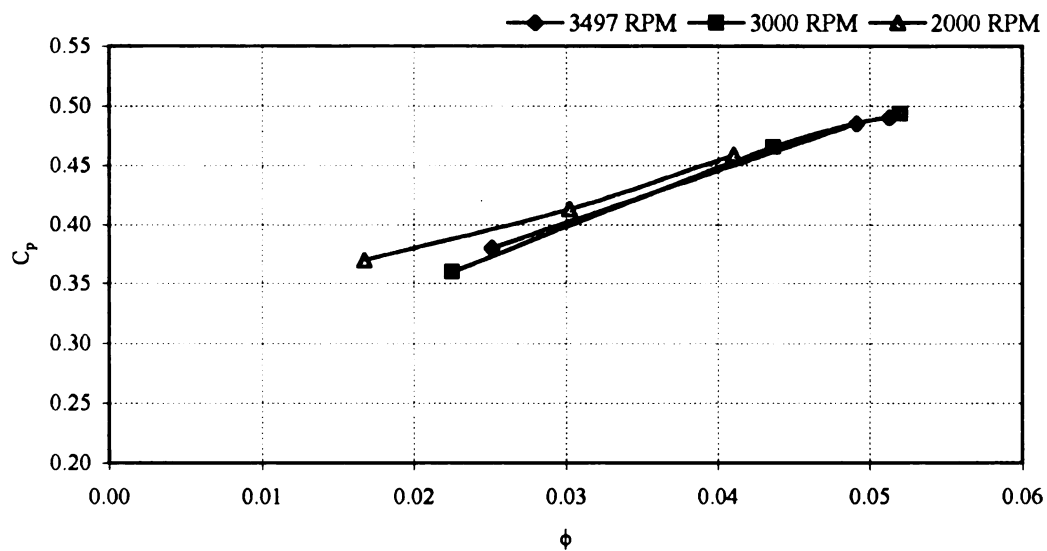
Figure 6.13: Diffuser Pressure Recovery Coefficient
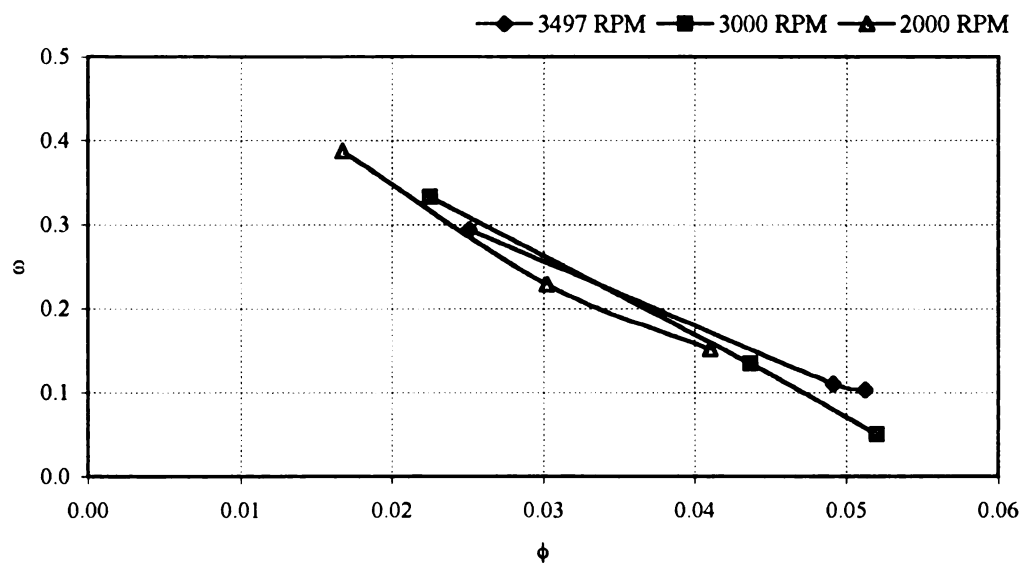
Figure 6.14: Diffuser Loss Coefficient

163
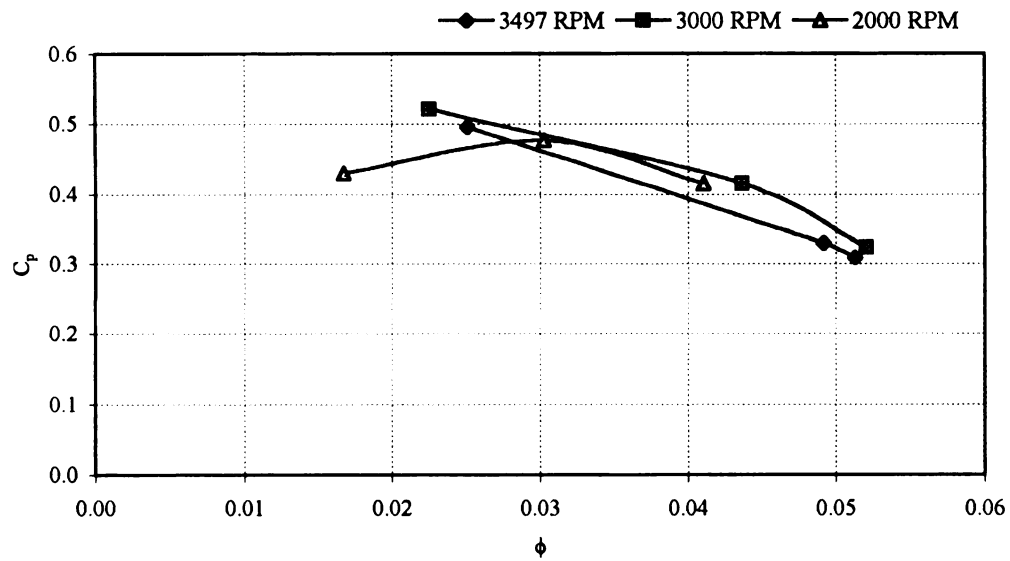
Figure 6.15: Volute Pressure Recovery Coefficient
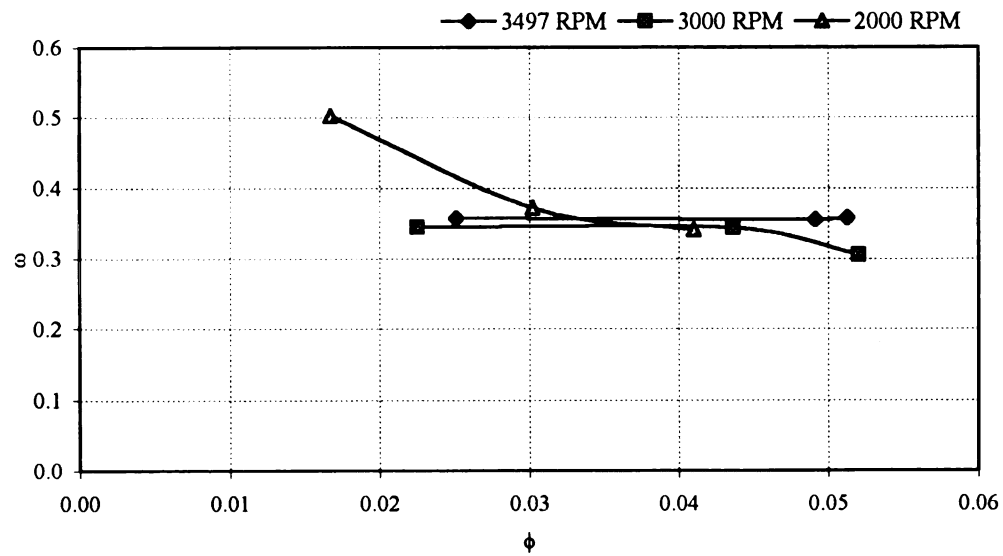
Figure 6.16: Volute Loss Coefficient
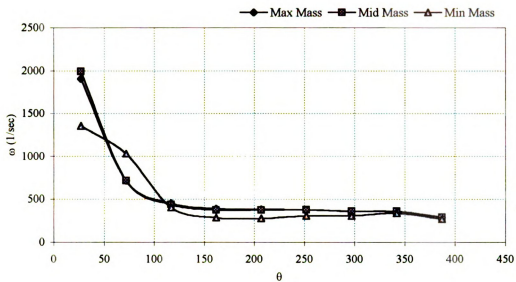
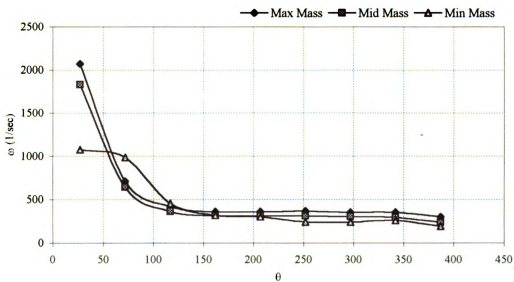Figure 6.17: Vorticity Magnitude at Different Volute Cross-Sections and 3497 RPM

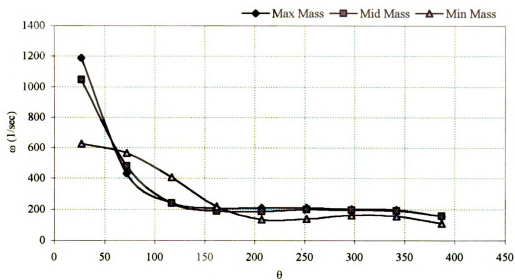Figure 6.18: Vorticity Magnitude at Different Volute Cross-Sections and 3000 RPM

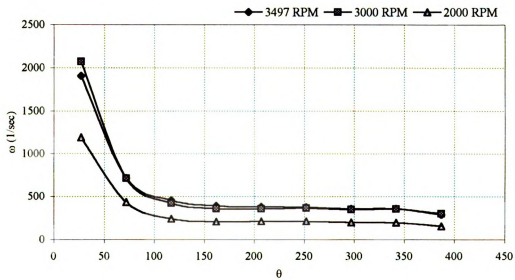Figure 6.19: Vorticity Magnitude at Different Volute Cross-Sections and 2000 RPM

Figure 6.20: Vorticity Comparison for Maximum Flow Rate and Different Speeds
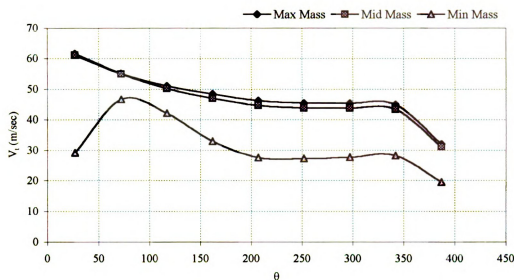
166

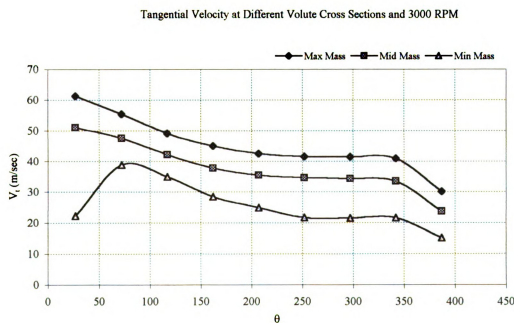Figure 6.21: Tangential Velocity at Different Volute Cross-Sections and 3497 RPM

Figure 6.22: Tangential Velocity at Different Volute Cross-Sections and 3000 RPM
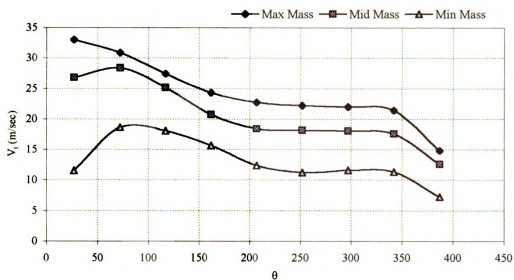
Figure 6.23: Tangential Velocity at Different Volute Cross-Sections and 2000 RPM
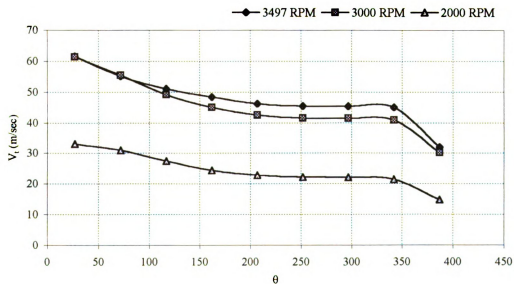

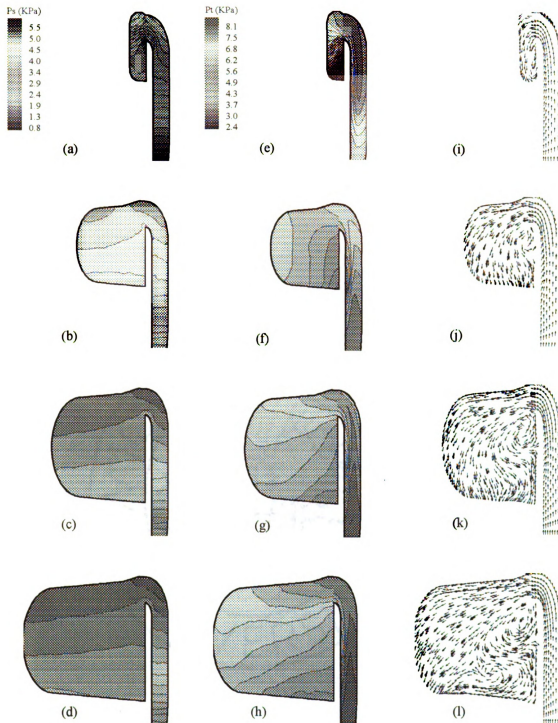Figure 6.24: Tangential Velocity Comparison for Maximum Flow Rate and Different Speeds

Figure 6.25: Static and Total Pressure Contours and Meridional Velocity Vectors for 3497 RPM, Maximum Flow Rate and Cross Section Angles (a) 27, (b)117,(c)207, (d)297

Figure 6.26: Static and Total Pressure Contours and Meridional Velocity Vectors for 3497 RPM, Mid Mass Flow Rate and Cross Section Angles (a) 27, (b)117,(c)207, (d)297

Figure 6.27: Static and Total Pressure Contours and Meridional Velocity Vectors for 3497 RPM, Min Mass Flow Rate and Cross Section Angles (a)27, (b)117, (c)207, (d)297

Figure 6.28: Static and Total Pressure Contours and Meridional Velocity Vectors for 3000 RPM, Max Mass Flow Rate and Cross Section Angles (a) 27, (b)117,(c)207, (d)297
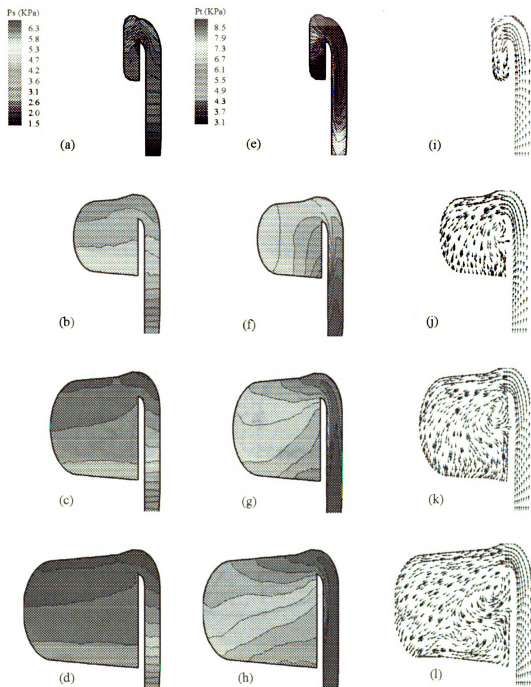
Figure 6.29: Static and Total Pressure Contours and Meridional Velocity Vectors for 3000 RPM, Mid Mass Flow Rate and Cross Section Angles (a) 27, (b)117,(c)207, (d)297
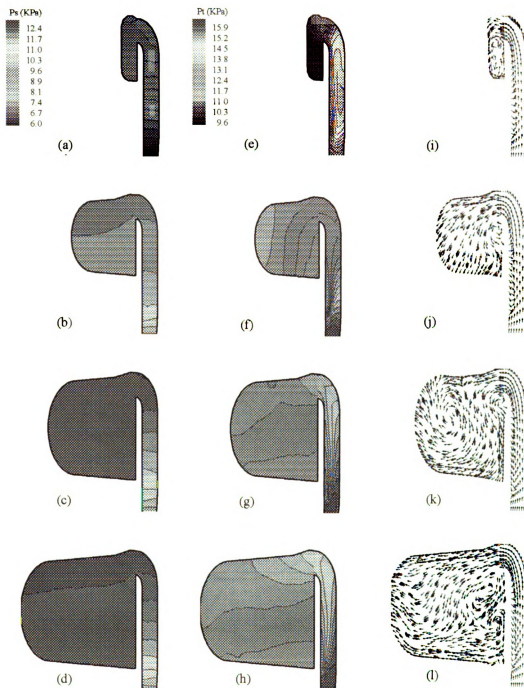
Figure 6.30: Static and Total Pressure Contours and Meridional Velocity Vectors for 3000 RPM, Min Mass Flow Rate and Cross Section Angles (a) 27, (b)117,(c)207, (d)297
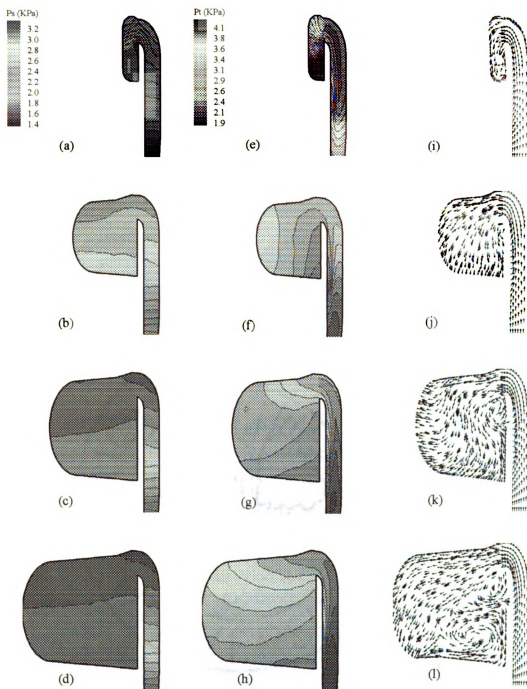
Figure 6.31: Static and Total Pressure Contours and Meridional Velocity Vectors for 2000 RPM, Max Mass Flow Rate and Cross Section Angles (a) 27, (b)117,(c)207, (d)297
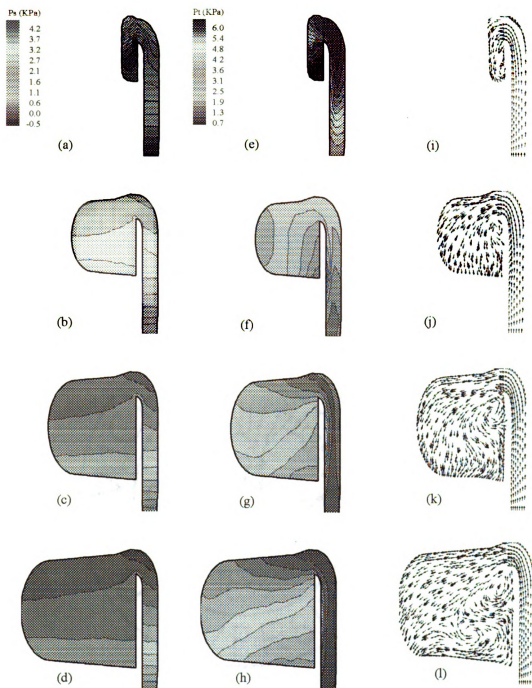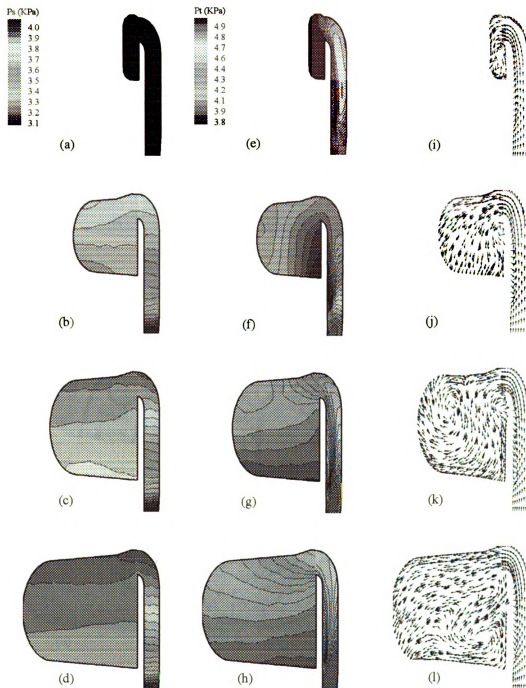
Figure 6.32: Static and Total Pressure Contours and Meridional Velocity Vectors for 2000 RPM, Mid Mass Flow Rate and Cross Section Angles (a) 27, (b)117,(c)207, (d)297
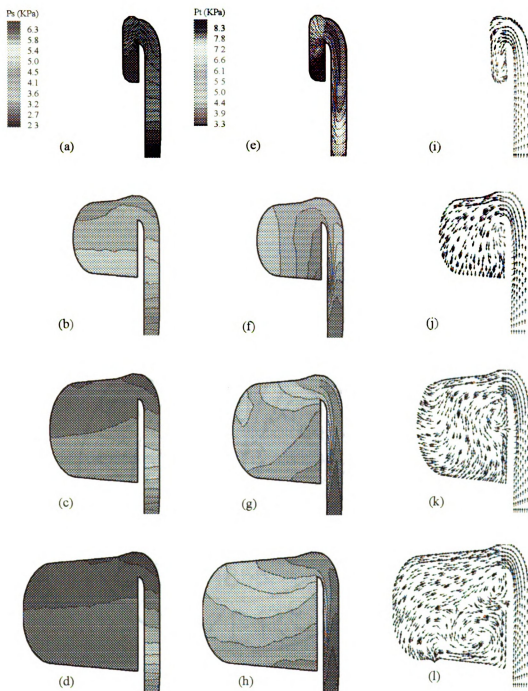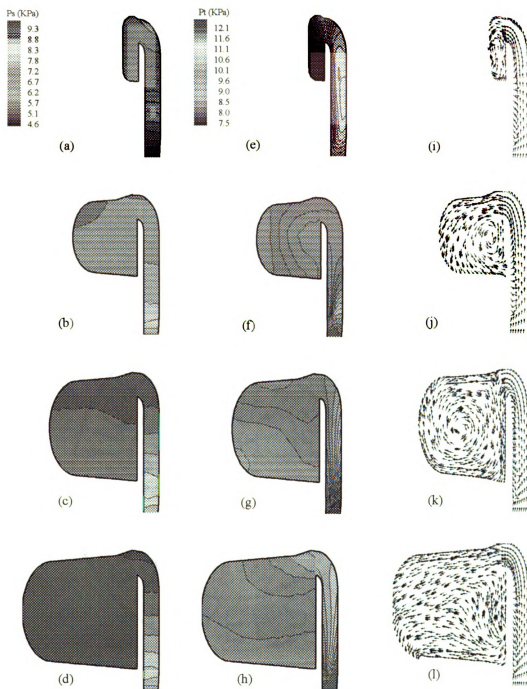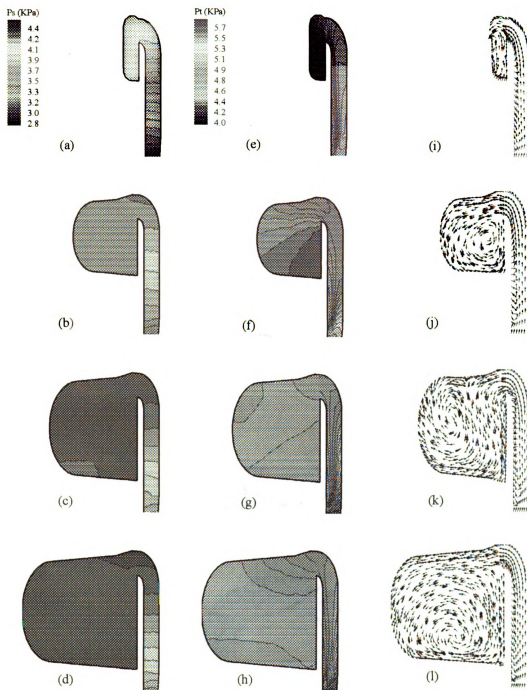
Figure 6.33: Static and Total Pressure Contours and Meridional Velocity Vectors for 2000 RPM, Min Mass Flow Rate and Cross Section Angles (a) 27, (b)117,(c)207, (d)297
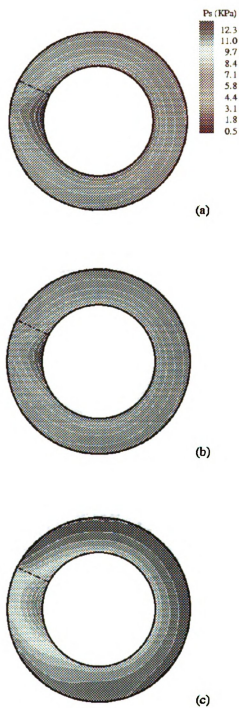
Figure 6.34: Diffuser Static Pressure Contours for 3497 RPM and (a) Max (b) Mid (c) Min mass flow rates
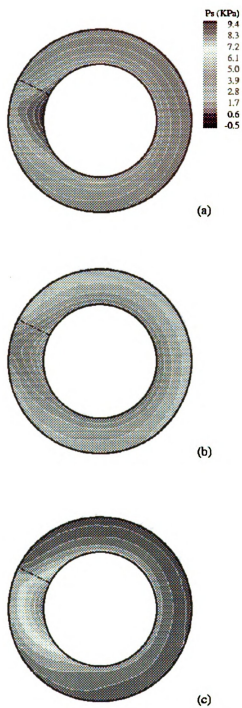
Figure 6.35: Diffuser Static Pressure Contours for 3000 RPM and (a) Max, (b) Mid, (c) Min Mass Flow Rates
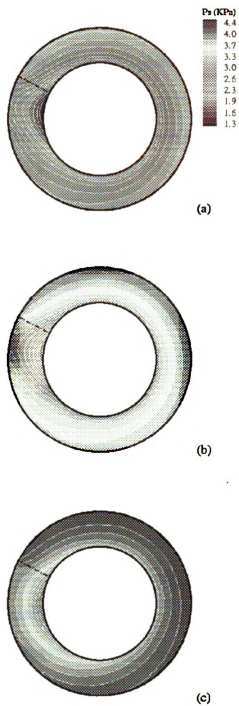
Figure 6.36: Diffuser Static Pressure Contours for 2000 RPM and (a) Max, (b) Mid, (c) Min Mass Flow Rates

CONCLUSIONS

In this investigation there were two primary objectives were considered:

1) To establish an advanced experimental facility, which enables understanding of the detail flow characteristics inside a volute geometry.

2) At the same time develop a numerical scheme that can predict and analyze the flow inside the volute.

With these two procedures, theory and experiments are complementing and supplementing each other in design and analysis of the volute flow. Hence, a designer or flow analyst is able to understand the losses and flow mechanism inside the volute, which results in design of an efficient volute.

An advanced testing facility with the capability of analyzing the flow in a centrifugal compressor was established. A CVHF 1280 Trane two stage compressor was modified to a single stage. This unit operates with refrigerant gas in commercial settings and after modifications air replaced the refrigerant. This facility is designed and modified for investigation of the performance, flow structure and loss mechanism in the stage and components. The vaneless diffuser and volute are utilized with static pressure taps to map the static pressure field in these two components. This compressor is utilized for measuring velocity vectors inside the diffuser and volute with five-hole and cobra probes in future. This unit can operate with the academic laboratory standards and its reassembly will enable the future researchers to modify the parts and convert it to a two-stage unit and perform investigation in any component of this compressor.

In this dissertation, the performance of the compressor at three speeds of 2000, 3000, 3497 RPM was evaluated. Upon calculating the mass flow rates in these speeds and comparing to the design conditions, it was found that the compressor is operating at off design condition. In the experimental results, the nonuniform circumferential static pressure distribution was observed in all cases. This was due to the effect of the tongue region on the compressor performance. There is a large circumferential pressure gradient between the volute outlet and inlet, which forces the flow to reenter the volute.

A meanline analysis of the impeller was performed with the experimental data in order to evaluate the performance of the impeller and provide diffuser boundary conditions at the diffuser inlet. It was predicted that the diffuser performance at lower speeds and mass flow rates results in stall because of the large flow angles entering the vaneless diffuser.

For the first time, to the best knowledge of the author, FLUENT has been utilized to perform flow simulation inside volute geometry. Currently in the Turbomachinery industry CFX-TASCFLOW is utilized for design and analysis of the flow in centrifugal compressors. This solver is a structured based in which creating the grid requires time consuming techniques. In contrast, the unstructured FLUENT solver was able to import CAD files directly and with the efficient grid generation schemes of GAMBIT, an unstructured mesh was generated for the vaneless diffuser and volute. Although the grid was unstructured, the results were in good agreement with experimental ones. Vortices were diagnosed inside the volute that contributes to higher losses. There is a large vorticity magnitude at the beginning of the scroll that decreases further downstream of the tongue. The decrease in this magnitude is due to the

formation of the counter vortex to dissipate the original vortex. This will result in dissipation of the kinetic energy inside the volute. In addition, the friction losses increase because of the large radial component of velocities produced by these swirling structures.

Flow at the inlet of the diffuser is uniform axially but the axial distribution deforms in the diffuser outlet because of the bend section. In lower mass flow rates, the momentum of the flow cannot overcome the large radial pressure gradients inside the vaneless diffuser and the flow separates. The separation of the flow becomes more pronounced with decrease in the mass flow rate. At 2000 RPM and minimum mass flow rate, the flow completely separates on the hub wall and extends back to the impeller region. It was observed that in this case, flow reenters from volute back into the vaneless diffuser. Overall pressure distribution contours showed that the volute is too large for these mass flow rates, which result in diffusion pattern circumferentially inside the volute.

One of the primary interests of industry in volute investigation is development of a methodology to perform optimization study for volute geometries. This dissertation presented an efficient technique to analyze the flow inside the volute with an optimum approach. All in-house codes can perform meanline analysis for the stages of a compressor in order to provide the inlet boundary conditions. With outlet boundary conditions obtained from a performance test, simulation can be performed for all cases. However, grid generation is always the difficult part of the simulation. If the original CAD file was drawn with shorter surfaces, GAMBIT could have handled the volume

grid generation easier and faster. In this approach generation of structured grid for profiles and interpolation of the surfaces, which is very time consuming, is not required.

.

REFERENCES

185

[1] Al-Zubaidy, S.N.J.
"A direct design procedure for centrifugal impellers", ASME 1992

[2] Al-Zubaidy, S.N.J.
" Towards optimizing the design of centrifugal impellers"

[3] Ayder, E.
"Experimental and numerical analysis of the flow in centrifugal compressor and pump volute"
Ph.D. thesis, Von Karman Institute For Fluid Dynamics, Sint-Genesius-Rode, Belgium, 1993

[4] Ayder, E., Van den Braembussche, R. A.
"Experimental study of the swirling flow in the internal volute of a centrifugal compressor"
International Gas Turbine & Aeroengine Congress, Orlando, Florida, 1991

[5] Ayder, E., Van den Braembussche, R. A., Brasz, J. J.
"Experimental and theoretical analysis of the flow in a centrifugal compressor volute"
International Gas Turbine & Aeroengine Congress, Cologne, Germany, 1992

[6] Ayder, E., Van den Braembussche, R. A.
"Numerical analysis of the three dimensional swirling flow in centrifugal compressor volutes"
International Gas Turbine & Aeroengine Congress, Cincinnati, Ohio, 1993

[7] Aungier, R. H.,
"Centrifugal compressor stage preliminary aerodynamic design and component sizing"
International Gas Turbine & Aeroengine Congress, Houston, Texas, 1995

[8] Bhinder, F.S., Mashimo, T., Jawad, S. N.
"On the use of numerical optimization in designing the radial impellers for centrifugal compressors"
International Gas Turbine & Aeroengine Congress, Tokyo, Japan, 1987

[9] Bruno eck, I.
"Fans"
Pergamon press, Oxford, 1973

[10] Carter, D.
"A Finite Element analysis of ideal flow in a centrifugal pump volute"
M.S. Thesis, University of Virginia, May 1981

[11] Chapple, P. M, Flynn P. F., Mulloy, J. M.
"Aerodynamic Design of Fixed and Variable Geometry Nozzleless Turbine Casings"
ASME Journal of Engineering for Power, Vol. 102, January 1980

[12] Chen, S., Lee, S., Huang, Y.
"A Mathematical Model for the Analysis of Fluid Flow in a Scroll"
ASME Journal of Fluids Engineering, Vol. 108, March 1986

[13] Chen, H.
"Design Methods of Volute Casings for Turbocharger Turbine Applications"
Journal of Power and Energy, Vol. 210, 1996

[14] Cohen, H., Rogers, G.; Saravanamuttoo, H.
"Gas Turbine Theory" (Third Edition)
Longman Group UK, Ltd., 1987

[15] Dillin, P., Sakai, T., Wilson, M., Whitfield, A.
"A computational and experimental evaluation of the performance of a centrifugal fan volute"
Proc Instn Mech Engrs Vol 212 Part A, 1998

[16] Dixon, S.L.
"Fluid mechanics and thermodynamics of turbomachinery", Fourth edition, 1998

[17] Eck, B.
"Fans – Design and Operation of Centrifugal, Axial-Flow and Cross-Flow Fans"
Pergamon Press, Oxford

[18] Eckert, B., Schnell, E.
"Axial- und Radialkompressoren"
Springer Verlag, Berlin 1961

[19] Elholm, T., Ayder, E., Van den Braembussche, R.
"Experimental study of the swirling flow in the volute of a centrifugal pump"
ASME Journal of Turbomachinery, Vol. 114, April 1992

[20] Engeda, A.
"Numerical flow prediction of the diffusion process in a radial vaneless diffuser"
Numerical Simulations in Turbomachinery, ASME 1995

[21] Engeda, A., Hagelstein, D., Hillewaert, K., Van den Braembussche, R. A., Keiper, K., Rautenberg, M., "Experimental and numerical investigation of the flow in a centrifugal compressor volute"
International Gas Turbine & Aeroengine Congress, Indianapolis, Indiana, 1999

[22] Gu, F
"Design and flow analysis of volutes for centrifugal compressors"
Ph.D. Dissertation, Michigan State University, 2000

[23] Hagelstein, D., Haessmann, H., Keiper, R, Rautenberig, M.
"Comparison of flow field and performance of internal and external volutes for centrifugal compressors"
Institute of turbomachinery, University of Hanover, Germany (1990)

[24] Hillewaert, K., Van den Braembussche, R. A.
"Numerical simulation of impeller-volute interaction in centrifugal compressors"
International Gas Turbine & Aeroengine Congress, Stockholm, Sweden, 1998

[25] Iversen, H., Rolling, R.; Carlson J.
"Volute Pressure Distribution, Radial Force on the Impeller, and Volute Mixing Losses of a Radial Flow Centrifugal Pump"
ASME Journal of Engineering for Power, April 1960, pp 136-144

[26] Japikse, D.
"Centrifugal Compressor Design and Performance"
Concepts ETI, Inc. 1996

[27] Li, X., Shen, H. H.
"Evaluation of a Shipboard Refrigeration System via Computer Simulation"
Dep. Of Civil and Environmental Engineering, Clarkson University, Potsdam, NY

[28] Lorett, J. A., Gopalakrishnan, S.
"Interaction between Impeller and Volute of Pumps at Off-Design Conditions"
ASME Journal of Fluids Engineering, Vol. 108, March 1986

[29] Ludwig, M.
"Development of a Volute Design Program using Visual Basic"
M.S. thesis, Michigan State University, East Lansing, MI, 1999

[30] Martinez-Botas, R. F., Pullen, K. R., Shi, F.
"Numerical calculations of a turbine volute using a 3-D Navier-Stokes solver"
International Gas Turbine and Aeroengine Congress & Exhibition, Birmingham, June 1996 (ASME Paper 96-GT-66)

[31] Miner, S., Flack, R., Allaire, P.
"Two-dimensional flow analysis of a laboratory centrifugal pump"
ASME Journal of Turbomachinery, Vol. 114, April 1992

[32] Palmer, D. L., Waterman, W. F.
"Design and development of an advanced two-stage centrifugal compressor"
Journal of Turbomachinery, Vol. 117, 205-211, April 1995

[33] Rodgers, C.
"Specific speed and efficiency of centrifugal impellers"

[34] Ronduner, C., Koppel, P., Kupferschmied, P., Gyarmathy, G.
"Comparison of measurement data at the impeller exit of a centrifugal compressor measured with pneumatic and fast response probes"
International Gas Turbine & Aeroengine Congress, Stockholm, Sweden, 1998

[35] Tabakoff, W., Sheoran, Y.; Kroll, K.
"Flow Measurements in a Turbine Scroll"
ASME Journal of Fluids Engineering, Vol. 102, September 1980

[36] Van den Braembussche, R.A., Ayder, E.
"Improved model for the design and analysis of centrifugal compressor volutes"
Von Karman Institute For Fluid Dynamics, Sint-Genesius-Rode, Belgium, 1997

[37] Van den Braembussche, R. A., Ayder, E., Hagelstein, D., Rautenberig, M., Keiper, K. "Improved model for design and analysis of centrifugal compressor volutes"
International Gas Turbine & Aeroengine Congress, Stockholm, Sweden, 1998

[38] Van den Braembussche, R. A.
"Centrifugal compressors, one dimensional design"
Course note 134, Von Karman Institute For Fluid Dynamics, Sint-Genesius-Rode, Belgium, 1987

[39] Van den Braembussche, R. A.
"Design and optimization of centrifugal compressors"
Course note 141/TU, Von Karman Institute For Fluid Dynamics, Sint-Genesius-Rode, Belgium, 1990

[40] Van den Braembussche, R., Hande, B.
"Experimental and theoretical study of the swirling flow in centrifugal compressor volutes", ASME Journal of Turbomachinery, Vol. 112, No.1, pp 38-43

[41] Van den Braembussche, R.
Flow in volutes of centrifugal compressors
Elliot Turbomachinery Company, Inc., Jeannette, PA, USA, April 1998

[42] Varghese, G., Mohana Kumar, T.; Rao, Y.
"Influence of Volute Surface Roughness on the Performance of a Centrifugal Pump"
ASME Journal of Fluids Engineering, Dec. 1978, Vol. 100, Pages 473-476

[43] Weber, C., Koronowski, M.
"Meanline Performance Prediction of Volutes in Centrifugal Compressors"
International Gas Turbine Conference and Exhibit, Duesseldorf, June 1986
(ASME Paper 86-GT-216, June 1986)

[44] White, F. M.
"Fluid Mechanics", Third Edition 1994

[45] Whitfield, A., Roberts, D. V.
"Alternative Vaneless Diffusers and Collecting Volutes for Turbocharger Compressors"
School of Engineering, University of Bath, ASME Paper 83-GT-32

[46] Whitefield, A.
"Preliminary design and performance prediction techniques for centrifugal compressors"
Developments in industrial compressors conference, London, UK, 1990

[47] Whitefield, A.
"Non-dimensional aerodynamic design of a centrifugal compressor impeller"
Proc Instn Mech Engr Vol 205, 1991

[48] Wilson, D.G.
"The design of high-efficiency turbomachinery and gas turbines", Second edition.